SCUOLA DI DOTTORATO
UNIVERSITÀ DEGLI STUDI DI MILANO-BICOCCA

Department of Materials Science

PhD program in Materials Science and Nanotechnology

XXXV Cycle

Assessment of Xenes for their integration into a plasmonic device platform

Bonaventura Eleonora

Registration number 862620

Tutor: Prof. Emiliano Bonera

Supervisor: Dr. Alessandro Molle

Coordinator: Prof. Marco Bernasconi

ACADEMIC YEAR 2021/2022

[…]

Collabora. Il confronto con gli altri ti arricchisce, sempre.

O alla peggio ti mostra cosa non vuoi fare e diventare.

@iniziolunedi

Table of contents

Introduction

Graphene has attracted enormous interest in various fields of science and technology, paving the way for the synthesis and exploration of new two-dimensional (2D) materials. Similar and sometimes complementary properties to those of the carbon honeycomb lattice have broadened the range of applications, shifting the focus from nanoelectronics to other areas such as photonics and optoelectronics.

Of all the possible families, there is a small cluster of 2D materials that has attracted particular interest since its debut: Xenes of group 14. Xenes constitute a single-element class of graphene-like 2D materials. Their electronic structure ranges from trivial insulators to tunable gap semiconductors and semi-metals but, due to a mixed sp^2-sp^3 orbital hybridization, they have an extremely reactive buckled structure and do not form van der Waals crystals. In fact, because of their intrinsic artificial nature, Xenes are mainly grown by epitaxy on specific lattice-matched substrates. While the strong interactions can be controlled to change the response of materials as required, the same interactions severely limit the access to Xenes optical response and then their integration into devices. Silicene grown on Ag(111) is emblematic of this. On the one hand, the Ag(111) substrate is crucial in forcing silicene to preserve the 2D honeycomb structure; on the other hand, it irreversibly affects the silicene electronic features.

The aim of this work is to identify strategies to access the optical and thermo-optical response of Xenes in order to develop an integrable Xene-based platform. Specifically, two strategies are proposed to overcome the problem of Xenes interaction with the native substrate. The first is to replace the silver substrate with an insulating one, such as sapphire. The second is to engineer the metal substrate by introducing a buffer layer that decouples the overlying Xene. Some technology transfer experiments to develop a plasmonic device based on the Xene-on-Al_2O_3(0001) platform are also reported.

By combining Fourier transform infrared spectroscopy (FTIR) and Vis-UV spectrophotometry, it is possible to extract the optical properties of a material in a wide frequency range. The encouraging results, obtained by growing silicon nanosheets on Al_2O_3(0001), have set

the scene for the use of the same substrate to grow stanene and thus enable the determination of its optical response from THz to UV.

Finding new suitable substrates is not the only viable route to preserve the properties of epitaxial Xenes. Introducing a buffer layer between an already known substrate and the Xenes may prove to be another valuable strategy to decouple them and gain access to fundamental properties. Here again, silicene is the forerunner for Xenes. The sequential growth of stanene and silicene on Ag(111) surface gives rise to what has recently been termed a "full Xene heterostructure". Clearly, the same concept can be extended to other systems and fits into the general framework of 2D heterostructures. Piling up Xene of different nature may be extremely advantageous. In some cases, it allows a large part of the know-how developed on the early system to be transferred to the new configuration. Access to the optical and structural properties of the heterostructures is possible through well-proven experimental techniques, such as Raman and optical spectroscopy. A careful study of the Raman response, as a function of variables like the spatial position or power of the incident radiation, can also provide additional data on induced strain, doping and even thermal behavior of the system under investigation.

Finally, the Dirac-like behavior observed in the infrared optical conductivity of 2D silicon nanosheets revealed the chance to get a Dirac plasmonic response from Xenes. Large carrier mobility and tunability make Dirac materials highly demanded for nanotechnology applications where the manipulation of light is required. The plasmonic resonance in Dirac systems is dependent on the doping level that, due to their semi-metallic nature, can be easily controlled through chemical doping or electrical gating. The high levels of charge injection obtained at low voltages make the ionic liquid gating an ideal method for controlling charge carrier density in 2D materials. However, this is only one of the two ingredients required to experimentally observe Dirac plasmon response. In far field, plasmons cannot be excited directly by the electromagnetic radiation. It requires an extra momentum, which can be added by periodically patterning the surface of the material. The fabrication of patterned Xene-based structures, with good control over shape and quality, is particularly challenging. The removal or etching of materials with high selectivity towards underlying layers, at extremely low thickness, requires atomic precision that can only be achieved with specific chemistry and dedicated etching tools.

Chapter 1

Two-dimensional materials

Since 2004, when the first graphene flake was isolated [128], fundamental and applied research on two-dimensional 2D materials has never stopped. In their structures the atomic arrangements and bond strengths along two dimensions are similar and much stronger than the bonds along the third dimension. 2D material properties are consequences of the elemental constituents, the symmetry of the crystalline structures, and especially the strong confinement in the direction perpendicular to the 2D plane. The ideal spatial distribution of several 2D materials is pictorially illustrated in the sketch in Figure 1.1.

1.1 A short trip through the "flatland"

The following is a quick overview of the best known 2D materials and their main properties. Its purpose is to introduce the overall context in which this work has developed.

- **Graphene**: In graphene the carbon atoms are arranged in a honeycomb lattice. The sp^2 hybridization between one s orbital and two p orbitals leads to a planar structure. The uninvolved p orbital, which is perpendicular to the planar structure, can covalently bond with neighbouring carbon atoms. Since each p orbital has an extra electron, the π band that is formed is half-filled. The energy band dispersion satisfies the Dirac equation, making graphene a Dirac semi-metal. Due to the unique electrical and optical properties, including ultra-high carrier mobility, ballistic transport effect, wide spectral response range and ultra-fast optical response time, graphene shows considerable potential for optoelectronics and photonics applications. Conversely, the main obstacle to the use of graphene in electronics is the well-known absence of an energy gap between its conduction and valence bands, at typical devices working temperature [52].

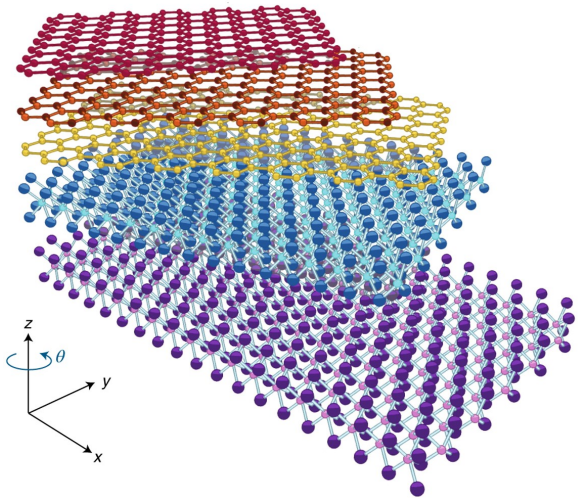

Fig. 1.1 Pictorial sketch of different staked 2D materials. From top to bottom, the sketches represent graphene, hBN and TMDs structures. Adapted from Ref. [155].

- **Hexagonal Boron Nitride (hBN)**: Layers of hBN consist of hexagonal rings of alternating B and N atoms, with strong covalent sp^2 bonds and a lattice constant nearly identical to that of graphite [129]. The wide band gap in the UV spectral range ($\sim$ $6eV$), mechanical strength and excellent chemical stability make hBN a suitable material for gate dielectrics, encapsulation or stabilisation of other 2D materials and heterostructures [189]. Moreover, hBN has also gained attention in because of a recent demonstration of strongly confined phonon-polariton modes, with frequencies typically in the mid-infrared (IR) spectral range, resulting from the coupling of light photons with optical phonons in polar dielectrics [24].

- **Insulating Oxides**: Many oxides have layered structures and can therefore be seen as a source for new 2D materials. These include lead oxide and lead salts, phosphorous oxides, and phosphates, molybdenum and vanadium oxides. In these materials, the layers are often connected by weak covalent bonds, oxygen bridges, or intercalating elements, and are normally non-stoichiometric. Moreover, layered oxides are normally polycrystalline, limiting the possibility of obtaining them by mechanical exfoliation. These structures are interesting as battery cathode materials, superconductors or passivating layers [193].

- **Transition Metal dichalcogenides (TMDs)**: The general formula that describes TMDs composition is MX_2, where M is the transition metal element from group 4 (Ti, Zr, Hf and so on), group 5 (V, Nb or Ta) or group 6 (for instance Mo or W) of the periodic table, and X is a chalcogen (S, Se, or Te). In their structure the chalcogen atoms are

in two hexagonal planes, which are separated by a plane of metal atoms. Adjacent layers are weakly held together to form the bulk crystal in a variety of polytypes, which vary in stacking orders and metal atom coordination. They offer a broad range of electronic properties, from insulating or semiconducting to metallic or semimetallic. This variety can be traced back to the progressive filling of the non-bonding d bands by the transition metal electrons [129]. In several semiconducting compounds (generally MoX_2 and WX_2) a transition from an indirect band-gap in the bulk to a direct band-gap in the monolayer occurs [170]. This behaviour has important implications for applications of TMDs in photonics, optoelectronics and sensing. Moreover, in recent years, research on TMDs has been extended to metallic compounds formed by group 10 metals [190]. Some of these, such as $PtSe_2$ and $PtTe_2$, have been identified as topological materials, paving the way for the experimental realisation of new states of matter [71].

- **MXenes**: MXenes are a large family of 2D carbides, carbonitrides and nitrides of transition metals with the general formula $M_{n+1}X_nT_x$, where M represents an early transition metal, X is carbon and/or nitrogen, and T_x stands for surface terminations such as OH, O and F. Due to a large variety of transition metals and surface functionalities, their properties can be tuned by selecting combinations of transition metals, X elements, and controlling their surface chemistry. In MXenes the metallic conductivity due to free electrons of transition metal carbide or nitride backbone is combined with the hydrophilicity resulting from their surface terminations. This, together with their mechanical properties, make MXenes attractive for an extremely large number of applications [66].

- **Xenes**: Xenes are buckled honeycomb lattices of a single element whose physical properties are determined by the elemental constituent. Historically, their diffusion as emerging materials is divided into two phases. Initially, the Xenes family only included materials composed of group 14 elements, which thus share the electronic structure with carbon. Subsequently, the definition was extended to include the elements from groups 13, 15 and 16 group, i.e. elements that are not directly related to carbon. Their electronic structure ranges from trivial insulators to semiconductors with tunable gaps, to semimetallic. Their topological properties induced by the spin-orbit effect in heavier elements are still being studied [62].

Although this is not an exhaustive description, it should illustrate the diversity that characterises 2D materials and the range of possible applications.

Among the materials listed, there is a small subset that has attracted much interest over the years because of the strong similarity between its members and graphene. These are the Xenes of group 14. To this similarity, which is mainly due to the electronic configuration of single elements, must be added the semiconductor industry's interest. Despite its outstanding electronic properties, graphene cannot be integrated in conventional transistor technology for logic operations. The switching mechanism necessarily implicates the presence of an energy gap that is missing in graphene at room temperature, but is expected in the band structure of Xenes. Moreover, the elements of group 14, and Si in particular, show an intrinsic affinity with semiconductor technologies currently in use.

1.2 Xenes of group 14

In their most stable form, Xenes based on Si, Ge, Sn and Pb atoms have a buckled honeycomb structure, which differs from the flat structure of graphene mainly due to the different degree of hybridisation of the chemical bonds. The hybridization is purely sp^2 in graphene, while is mixed sp^2-sp^3 in silicene and germanene, and almost fully sp^3 in stanene and plumbene. The different degree of hybridisation of the atomic orbitals and the resulting buckling of the crystal structure have several implications for Xenes.

Firstly, they do not form van der Waals crystals and therefore, they cannot be produced through methods commonly used for the synthesis of graphene or other van der Waals materials (e. g. mechanical or liquid exfoliation). Although silicene, germanene, stanene and plumbene were predicted to be stable in their freestanding fashion, they need peculiar conditions to be realised. Epitaxy is the most common method of synthesising Xenes and the substrate plays a fundamental role. Indeed, only a limited number of substrates is commensurate with the free-standing Xene structure [62].

Stability is a second key aspect when dealing with Xenes. The preference for an sp^3 hybridisation, again, makes them extremely reactive. In fact, when exposed to air, 14-group Xenes are subject to degradation. A solution to this issue was given by encapsulating silicene first [119], and then phosphorene (the 2D allotropic form of phosphorous) [116]. An amorphous and non reactive Al_2O_3 capping layer can be deposited on supported Xenes, resulting in the preservation of their chemical environment. The protective layer is obtained by sequentially growing elemental Al in the first stage, and Al in an O_2-rich environment in the second stage [116]. A number of benefits can be attributed to the introduction of the capping layer. It allows materials to be removed from the ultra-high vacuum conditions typical of epitaxial growth, enabling *ex situ* characterisation. Xenes are not affected by collateral contamination and the capping can also works as an insulating layer for applications where a

gate is required. It is important to note that degradation is significantly reduced even when multilayer configurations are taken into account [60].

The reactivity of Xenes is also reflected in their interaction with the native substrate. A given substrate can actually influence the lattice geometry and electronic properties of the supported material even if there is a correspondence between the lattice constants of the two materials [117]. This fundamental facet has driven all the progress that has been made, from 2D honeycomb structure theory for silicon and germanium to the latest developments in device integration. Some of the aspects that will be discussed can be generalised to all the Xenes in the 14-group. In this respect, silicene and stanene will be taken as a case in point for the investigation.

1.2.1 Silicene

From a theoretical point of view, the hexagonal lattice of silicon (Si) has been appeared even earlier than graphene: in 1994 Takeda and Shiraishi [159] proposed the aromatic stages of silicon and germanium, presenting them as hypothetical materials. In this work they introduced the idea of a stable corrugated structure with a D_{3d} group symmetry, which is now recognized as a key feature of group-14 Xenes [117]. However, it took several years before these structures received the attention they deserved. The isolation of a single layer of graphene [128] was certainly a decisive event in this respect.

The term silicene was first used in a theoretical paper in 2007 [165], describing a two-dimensional sheet with a honeycomb lattice composed of Si atoms. In the following years, many theoretical groups have worked to clarify the structural and electronic properties of silicene, providing useful information for its experimental realisation.

Based on DFT calculations, a low-buckled honeycomb structure was found to be more stable than planar or high-buckled structures for silicene in its freestanding form [18]. The low-buckled silicene configuration was predicted to have a lattice constant of $b = 3.83$ Å and a bond length of $d = 2.25$ Å, while the vertical distortion translates as a buckling distance $\Delta = 0.44$ Å and a bond angle $\theta = 101^{\circ}$. This implies the interplay of sp^2 and sp^3 hybridized states in the bond. Furthermore, the system exhibited a semi-metallic electronic nature, with π and π^* bands crossing the Fermi level at the K and K' points. Similar results where obtained in different theoretical works, reporting values for the Si-Si bond length smaller than the distance in the bulk Si [70, 99].

Experimentally, the growth of silicene has been reported mainly on metallic templates. As already mentioned, the choice of substrates requires very restrictive constraints. The substrate must be commensurate with the predicted stable configuration of the freestanding Xene and the chemical reactivity with the X- adatoms must be negligible. Most of the studies

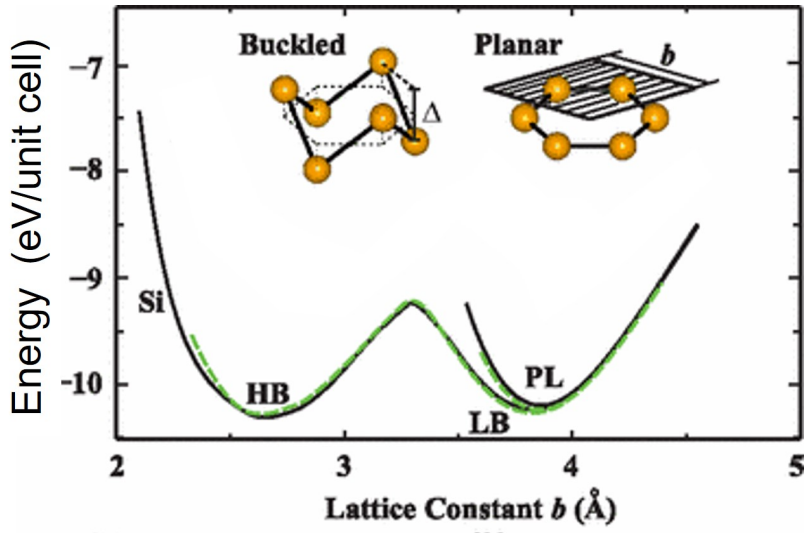

Fig. 1.2 Energy versus hexagonal lattice constant of 2D Si, calculated for various honeycomb structures. In the inset are shown the planar and buckled geometries together with buckling distance Δ and lattice constant of the hexagonal primitive unit cell b. Adapted from Ref. [18].

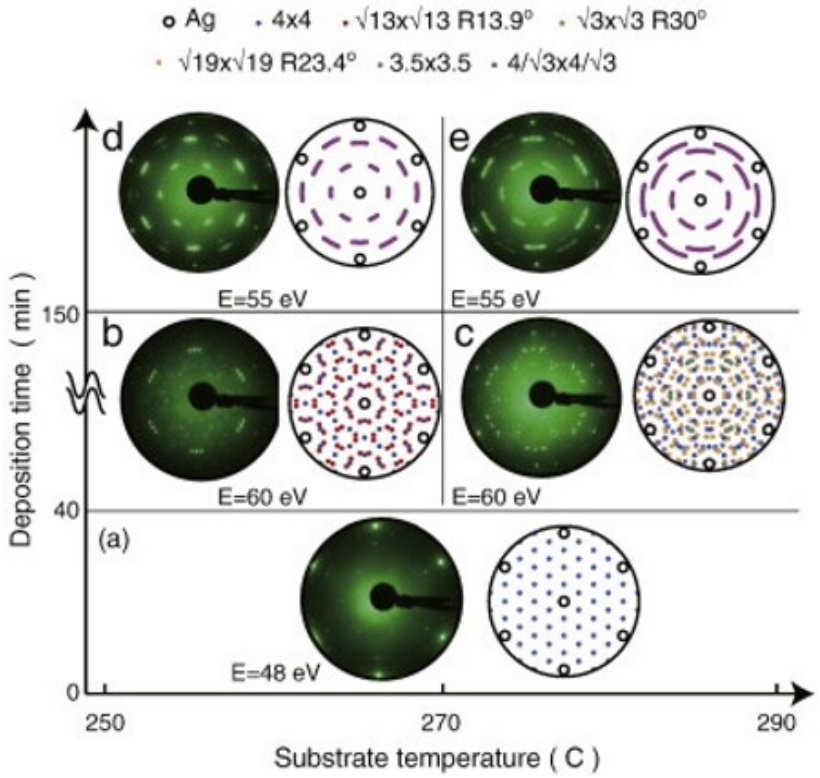

Fig. 1.3 LEED pattern of the phase evolution of silicene on Ag(111) depending on substrate temperature and deposition time. a) Pure 4×4 and b) a mixture of 4×4 and $\sqrt{13} \times \sqrt{13}$phases. c) Mixture of the 4×4 and minority phases. d) and e) $4/\sqrt{3} \times 4/\sqrt{3}$. Adapted from Ref. [5].

on silicene reported in the literature have been performed by choosing Ag(111) as substrate due to the symmetric character of its surface unit cell [59].

Silicene on Ag(111) shows several phases that depend on both the commensurability relation with the substrate surface and the allowed buckling distributions. The epitaxial phases of Xenes are generally described in terms of the substrate primitive lattice vectors or with respect to the freestanding Xene unit vectors. Temperature and surface coverage affect the phase reconstruction of silicene on Ag(111) due to the metastable nature of the 2D structure [5, 120]. The LEED patters of the phase evolution of silicene on Ag(111) reported by Arafune and co-workers [5] are shown in Figure 1.3. For a low coverage, LEED patterns show the 4×4 phase. Increasing the amount of evaporated Si, in the temperature range 523-543 K, the $\sqrt{13} \times \sqrt{13}$ phase appears. Additional evaporation of Si changes the silicene structure and the LEED pattern shows a $4/\sqrt{3} \times 4/\sqrt{3}$ phase.

Silicene has also been grown on other metal substrates. ZrB_2 [54] and Ir [112, 172] were used as template for silicene deposition, giving rise to buckled structures with electronic properties dramatically affected by the hybridization with the substrates.

Huge efforts have been made to synthesise quasi free-standing silicene on various substrates, and the debate on the real possibility of obtaining a large area extended non-interacting silicene layer on such substrates is still ongoing. However, the predicted gap opening in a band structure very similar to graphene continues to drive silicene research.

1.2.2 Stanene

Theoretical studies of the 2D honeycomb structure of tin (Sn) atoms have often been a natural extension of those carried out on silicene [100]. According to the generalized gradient approximation, stanene structure consist of a buckled hexagonal lattice, containing two atoms in each primitive cell with an optimized lattice constant of ~ 4.5 Å. The size of the Sn atoms, which is larger than that of C, induces inner-core repulsion forces. Consequently, stanene also has a structure in which adjacent atoms prefer an out-of-plane orientation with a mixture of sp^2 and sp^3 orbital hybridisation states [19]. In another work, the structure of freestanding stanene has been classified in high-buckled (HB) and low-buckled (LB) [143]. The HB phase is structurally comparable with stable β-Sn, while the LB phase with α-Sn. α- (or gray) and β- (or white) are the two allotropic crystalline forms of tin. Gray tin shows a cubic, diamond like structure. It is a metastable phase that can transform into the tetragonal β phase above the phase transition temperature of 13.2 ° C. By introducing an *ad hoc* phase-stabilising substrate, this temperature can be increased [154]. The transition from HB to LB phase involves an increase in lattice constant. A stable structure of hexagonal stanene in the geometric dumbbell configuration reported in Figure1.4a-b, due to the high

cohesive energy of the Sn atoms, has also been reported. The stability of this structure is supported by the positive phonon frequencies over the entire Brillouin zone, that is shown in Figure 1.4c [161].

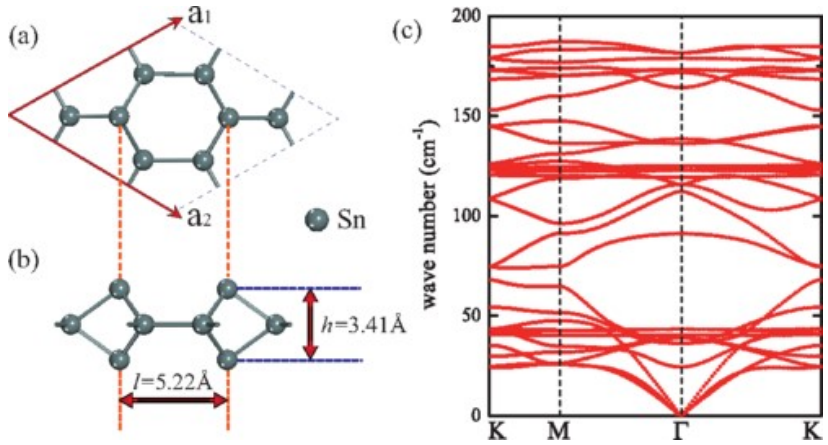

Fig. 1.4 a) Top view and b) side view of the dumbbell stanene structure. The lattice unit vectors (a1 and a2), the distance between two dumbbells in a unit cell (l) and the height of the structure (h) are also reported. c) The phonon dispersion of the dumbbell stanene structure. Adapted from Ref. [161].

The epitaxial growth of stanene has been explored on various substrates. Experimental results show an high sensitivity of stanene properties to strain and chemical passivation [145]. This is why the correct control of the interfacial interaction is of crucial importance. In 2015, the growth of 2D stanene nanosheets on $Bi_2Te_3(111)$ substrate has been reported, along with an atomic and electronic band structure analysis, paving the way for further experimental studies [50]. Scanning tunnelling microscopy (STM) images together with the proposed atomic structure model is reported in Figure 1.5.

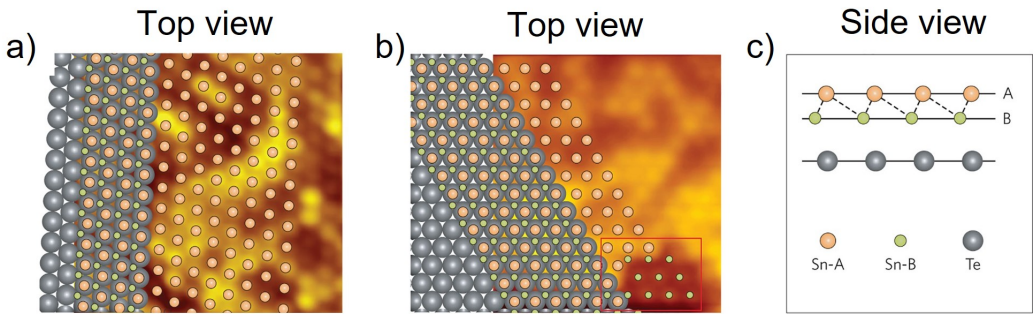

Fig. 1.5 a-b) atomic structure model superimposed on STM images of the epitaxial stanene layer. c) Side view. Adapted from Ref. [50].

From the outset, stanene was considered a very promising material because of an aspect that distinguishes it from other Xenes in the same group: spin-orbit (SO) coupling. This effect is also present in other elements. However, the atomic weight of tin, compared to that of carbon and silicon, amplifies its influence on the properties of the system. The next chapter discusses this topic in more detail. For now, here are some notable experimental results.

A stable superconducting quantum state was observed in a few-layer stanene, grown layer by layer using MBE technique, on buffer PbTe(111)/Bi_2Te_3 heterostructures [94]. Similarly, high-quality single layer stanene (in the α phase of Sn) has been grown on InSb(111). In this case the compressive strain on the "α-stanene" resulted in a gap opening larger than that expected for free-standing stanene [179]. Epitaxial growth of low-buckled planar stanene has been developed on an Ag(111), after the formation of an Ag_2Sn surface alloy [187]. Deformation-induced effects in the band structure of epitaxially grown stanene were observed on a semi-metallic Sb(111) surface [58].

1.2.3 Access to the electronic properties of Xenes

In the experiments reported so far, the epitaxial growth of Xenes has been mainly realised on metal substrates. Regardless of the specific material, the band structures of silicene and stanene always share a common feature: hybridisation effects with the substrate. The effect of the substrate is therefore not only to determine registry in the vertically distorted honeycomb structure through the commensurability relationship, but also to alter the electronic structure of the Xenes through hybridisation [59]. The case of Ag-supported silicene can again be taken as a paradigmatic example of this strong interaction.

Angle-resolved photoemission spectroscopic (ARPES) measurements (see Figure 1.6a) showed the presence of linear bands near the Fermi level of silicene, which were interpreted as being due to the hybrid Si-Ag bands rather than the mass-less silicene fermions [168]. The previous result was also confirmed by optical spectroscopic measurements.

For instance, Cinquanta and co-workers [31] reported a combined experimental and theoretical study of the optical response of silicene on Ag, where electronic transitions involving Ag states were found to contribute significantly to absorption. Figure 1.6b shows the calculated absorption spectra of supported and unsupported silicene compared to that of an amorphous silicon layer. The strong Si-Ag hybridization has been proven to deeply affect the electronic properties and therefore the optical response of the supported silicene. The resulted absorbance spectrum is a superimposition of different contributions with mixed Si-Ag and Ag-Ag transitions. In particular, the absence of a peak at 1.6 eV combined with the sharpening and redshift of the main absorption peak to around 3.3 eV in supported silicene, was attributed to Si-Ag hybridisation. It is worth reporting on recent studies of Au(111)-

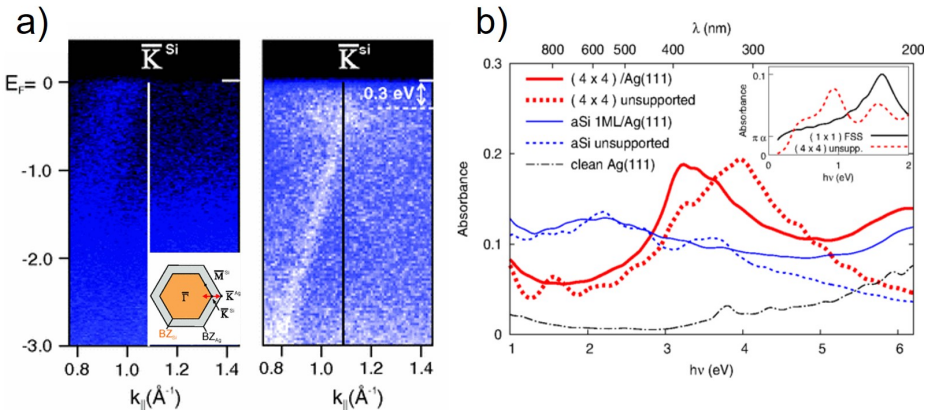

Fig. 1.6 a) ARPES intensity maps for clean Ag surface (left) and after formation of silicene (right). The inset shows the scheme of the 2D Si layer with respect to the Ag(111) surface. The red arrow indicates the measurement direction. Adapted from Ref. [168]. b) Calculated absorbance of Ag-supported and unsupported 4×4 superstructure compared to the supported and unsupported amorphous silicon. The calculated absorbance of the bare Ag is also reported. In the inset the absorbance of 1×1 free-standing and unsupported silicene are compared. Adapted from Ref. [31].

supported silicene and passivated by hBN. Optical measurements showed the preservation of the low-energy band structure around the Fermi level and thus the preservation of the Dirac electrodynamics expected for silicene [56].

Silicon nanosheets on Al_2O_3(0001)

One way to preserve the properties of Xenes seems to be to grow them on commensurate insulating substrates, so that their electronic states occur in the substrate gap [101]. Using Al_2O_3(0001) has recently been suggested as a possible strategy in this respect. Al_2O_3(0001) is a dielectric material with a reported experimental band gap of ~ 9 eV [55]. As a large-gap semiconductor, with a sufficient work function, the substrate ensures that the electronic states of the Xenes are in the gap and do not interact with its own. Moreover, silicene and stanene are predicted to grow with limited interaction with on its Al-terminated surface [26, 169]. Basically, it can stabilize a monolayer honeycomb structure of silicene and stanene without destroying the Xenes electronic states. The experimental realisation of 2D silicon on $Al_2O_3(0001)$ was reported a short time after these theoretical predictions.

Grazianetti *et al* [61] investigated the optical properties of Si nanosheets at 2D limit, epitaxially grown on Al_2O_3(0001), as function of films thickness. The optical conductivity of thin samples, reported in Figure 1.7a, show an overall behavior similar to that expected from the ideal silicene. As it will be discussed later, the optical conductivity is strongly related

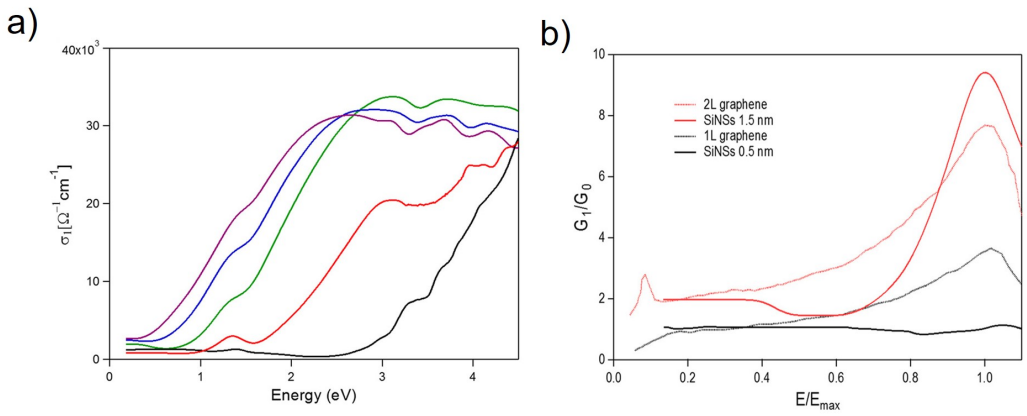

Fig. 1.7 a) Real part of the optical conductivity $\sigma_1(\omega)$ for 0.5 (black), 1.5 (red), 3 (green), 5 (blue), and 7 nm (purple) of epitaxial silicon. b) Real part of the optical conductance $G_1(\omega)$ normalized to the universal optical conductance G_0 for the 0.5 (black line) and 1.5 nm (red line) thickness silicon nanosheets. The frequency axis is normalized to the bonding–antibonding π transition appearing around 1.4 eV in Si nanosheets and around 4.6 eV in graphene. Adapted from Ref. [61].

to the join density of states (JDOS), thus it provides reliable band structure information. The absorption feature at $\sim$ 1.4 eV and the increasing absorption around 4 eV for small thicknesses, as described in the following chapter, are consistent to those resulting from interband transitions in the free-standing silicene band structure. In addition, a Dirac-like behaviour is observed in the IR part of the optical conductance, suggesting the presence of Dirac fermions hosted by the silicene-like band structure. Normalizing the actual frequency with respect to the bonding-antibonding π transitions for silicene and graphene, they obtained the universal frequency axis reported in Figure 1.7b. The quantized conductance suggests that silicon nanosheets show silicene-like properties as already proved for graphene [108]. This experimental scenario has been supported by *ab initio* calculations.

An interesting aspect to consider is that the encapsulation procedure, introduced at the top of this section, has been applied also in this case. The amorphous capping layer did not affect the optical properties of the Si nanosheets on $Al_2O_3(0001)$ due to its low thickness and intrinsic transparency, allowing the optical characterisation [61].

Importantly, the identification of Dirac-like optical conductivity in silicon-like nanosheets grown on optically transparent substrates paves the way for their exploitation in plasmonics applications. Plasmons offer the possibility of storing the information encoded in a beam of light at subwavelength spatial scales, a property of great interest for optoelectronic applications and already exploited in nano-sensors [97, 139]. The subwavelength confinement implies that the electromagnetic energy associated with the light field is highly concentrated

in specific points. Here the interaction of light and matter is strongly enhanced thus allowing for ultrafast processing of optical signals down to the femtosecond timescale. Dirac plasmons hold great promise for novel tunable optical devices operating in multiple frequency ranges (from terahertz to the visible) with extremely high speed, low driving voltage, low power consumption and compact size [64, 34, 104].

1.3 Motivation and outline of the thesis

Silicene and stanene have different properties. However, they present similar problems in terms of synthesis and characterisation. Their experimental forms, when realised on substrates of a metallic nature, differ drastically from their free-standing counterparts due to the critical role played by the substrate. It acts on two levels: while the commensurability relationship determines the geometric features of the hexagonal lattice, the strong hybridisation with the atoms alters the band structure. From the examples given in the previous section, two important facts emerge. The first is that the interaction between silicene and Ag is not negligible. The second fact is the clear link between the electronic properties and the optical response of silicene. Both of these aspects can also be extended to the stanene [58, 187, 35]. More generally, the strong radiation-matter interaction that 2D materials experience due to their spatial confinement is the basis for photonics and opto-electronics applications. Access to 2D materials optical properties is therefore a fundamental prerequisite for the development of reliable devices.

This thesis deals with the optical characterisation of different Xene-based configurations. The main objective is to identify one or more strategies to access the optical properties while excluding or controlling the influence of the native substrate. The work also aims to assess the integration of Xenes into a device. In particular, the possibility of using the a-Al_2O_3-Xene-Al_2O_3(0001) configuration as a platform to study the plasmonic response of these materials will be evaluated. The structure of the thesis is the following:

- In the first part of Chapter 2 the band structure of 14-group Xenes is presented, together with the implications for the optical response of free-standing silicene and stanene. In the second part, collective electronic excitations, i. e. plasmons, are introduced and their main features in 2D Dirac systems are discussed in detail. These concepts are presented to support the results reported in Chapters 4, 5 and 6.

- The experimental techniques used in this work are discussed in Chapter 3. The first part is focused on the growth technique mainly used to produce Xenes: the molecular beam epitaxy (MBE). The two systems used to grow two different sample configurations (i.

e. Xenes on $Al_2O_3(0001)$ and Xenes on Ag(111)) are introduced. The basic concepts of the X-Ray photoelectron spectroscopy (XPS) and the low energy electron diffraction (LEED) techniques are then described, whereas optical and Raman spectroscopy are discussed in more detail. This chapter also describes the photolithography and etching processes used to fabricate plasmonic gratings. The final section is dedicated to the ionic liquid gating.

- The experimental realization and investigation of the optical response of stanene-like thin films grown on $Al_2O_3(0001)$ is the focus of Chapter 4. In addition to direct growth, the possibility of introducing a graphene buffer layer to control the interaction with the substrate was being evaluated.

- Chapter 5 explores the possibility of decoupling silicene grown on Ag(111) by introducing an interlayer of stanene between the two materials. The optical response of silicene as a heterostructure component is compared with silicene grown directly on Ag(111). The effect of the tin layer on the overall properties of the system is finally investigated by means of opto-thermal Raman spectroscopy.

- Chapter 6 illustrates the steps taken to realize plasmonic devices based on silicene-like films grown on $Al_2O_3(0001)$ and stanene-like films grown on graphene/$Al_2O_3(0001)$. Finally, some preliminary results of the optical characterisation of the realised devices are reported in the same chapter.

Chapter 2

Optical properties of IV-group Xenes

As partially shown in the previous chapter, Xenes represent an important platform for the development of new technological applications. Specifically, the atomically thin nature and the optical excitations supported by these materials make them particularly attractive in the fields of optoelectronics and photonics.

This chapter introduces the optical properties of Xenes and their relationship to the electronic band structure, with the aim of providing a theoretical background to support the arguments discussed in this work. Some of the physical effects that most influence the optical response are also presented. The second part of the chapter introduces the basics of plasmonics. The principles of surface plasmon propagation and confinement are explained, as well as the grating coupling technique. The last part is devoted to the theory describing the plasmonic response in 2D systems, with a focus on Dirac materials.

2.1 The electronic band structure

The properties of graphene depend on the sp^2 hybridization between one s-orbital and two p-orbitals, and the consequent formation of a σ-bond between carbon atoms. The unaffected p-orbital which is perpendicular to the planar structure of graphene can bond covalently with neighboring atoms, leading to the formation of a π-band. Since each p-orbital has one extra electron, the π-band is half filled and this makes graphene a semi-metal with a zero band-gap [123]. Starting from a tight-binding approach, in which the electrons can hop to nearest neighbors atoms, and expanding the full band structure close to the K point in the momentum space the well-known linear dispersion for the energy is obtained (see Figure 2.1a):

$$E_{\pm}(\vec{k}) \approx \pm v_F|\vec{k}| + O((k/K)^2) \tag{2.1}$$

where $\vec{k}$ is the momentum and v_F is the Fermi velocity. The low energy dynamics of graphene charge carriers mimic relativistic particles with zero mass: their transport is governed by the Dirac's equation.

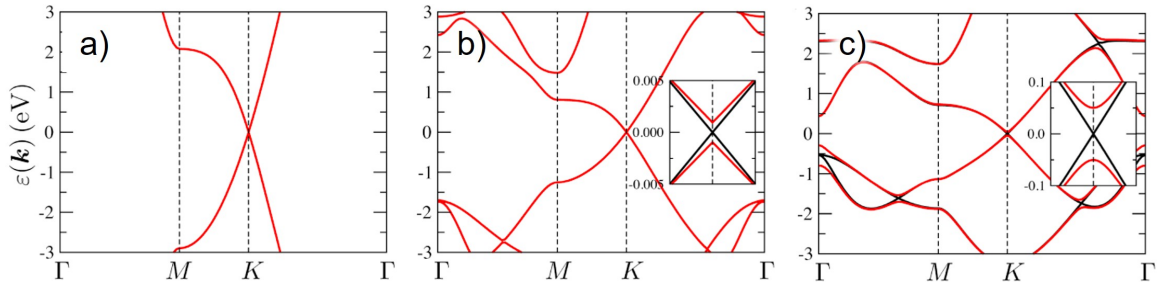

Fig. 2.1 Band structures of (a) graphene, (b) silicene, and (c) stanene along high-symmetry lines of the 2D hexagonal Brillouin zone. For silicene and stanene, the inset shows a magnification of the electronic bandgap around the Dirac point together with the band structure obtained without SO coupling (solid black lines). Figure adapted from Ref. [110].

Differently from graphene, Xenes are buckled and show a mixed sp^2-sp^3 hybridization. Despite a resulting buckling amplitude, the π and σ bands are still decoupled, and Dirac cones are formed by the π and π^* bands with a zero gap at the corners K and K^* of the Brillouin zone [18] (see Figure 2.1 b-c).

2.1.1 The Spin-Orbit coupling

According to the symmetry of the system, a low energy effective Hamiltonian can be defined in case of Spin-Orbit (SO) coupling. Considering Xenes in a planar configuration, near the K point of the Brillouin zone, this will be [100, 99]:

$$H_{eff}^{[K]} \approx \begin{bmatrix} -\xi\sigma_x & v_F(k_x + ik_y) \\ v_F(k_x - ik_y) & \xi\sigma_z \end{bmatrix} \tag{2.2}$$

where v_F is the Fermi velocity of π electrons near the Dirac points with a linear energy dispersion, and σ_z is the Pauli matrix. The effective Hamiltonian near point K^* is related to the one near K by the time-reversal operation.

At this point, it is convenient to shift the focus to silicene. The results will then have a general application to the other Xenes in the group of 14. The effective SO coupling for planar silicene is obtained from a tight-binding model [184] and is expressed as:

$$\xi \approx 2\xi_0^2|\Delta_\varepsilon|/(9V_{sp\sigma}^2) \tag{2.3}$$

where Δ_ε is the energy difference between the $3s$ and $3p$ orbitals and ξ_0 is half the intrinsic spin-orbit coupling strength. The parameter $V_{sp\sigma}$ corresponds to the σ bond formed by the $3s$ and $3p$ orbitals. Equation 2.2 leads to the following energy dispersion:

$$E(\vec{k}) = \pm\sqrt{(v_F k)^2 + \xi^2} \tag{2.4}$$

Taking the values of the corresponding parameters, the energy gap at the Dirac points can be estimated as $E_g = 2\xi$. For silicene, this value corresponds to 0.1 meV [99]. This result is obtained by considering a planar lattice configuration where the angle θ between the Si-Si bond and the direction normal to the plane has the minimum value ($\theta = 90°$, sp^2 hybridization). In this case the π and σ orbitals are coupled only through the intrinsic SO interaction. It has already been seen, however, that for Xenes the most favourable configuration is the low-buckled one [18]. With a deviation from the planar geometry the π and σ orbitals can directly hybridize and the effective SO coupling increases, depending on the angle θ. In the low-buckled structure ($\theta = 101.73°$, mixed sp^2-sp^3 hybridization) the calculated energy gap for silicene is 1.55 meV. The opening of a gap, greater than that expected for graphene considering the SO coupling [80], is a relevant result for Xenes.

This band gap opening at the Dirac point, which is shown the inset of Figure 2.1b and Figure 2.1c, is responsible for the quantum spin Hall (QSH) effect, a state with non trivial topological properties. This time-reversal invariant electronic state is gapped in the bulk and conducts charge and spin in gapless edge states without dissipation [81, 99]. The QSH is robust against scattering. It may be applied in dissipation-less conducting wires, thus limiting the power consumption of devices [59]. In graphene the QSH effect is weak and can only be accessed at very low temperatures [80, 72]. Conversely, silicene, germanene, but even more stanene show a stronger SO coupling than graphene, which leads to energy gaps of 1.55 meV, ~ 23.9 meV and ~ 100 meV respectively [99, 100]. Such values would enable operations on the device even at room temperature.

The mixed sp^2-sp^3 hybridisation makes Xenes chemically reactive. Therefore, substrate engineering or functionalization can have a huge impact on the electronic band structure of Xenes. Chemical functionalisation of 2D materials is already known to be an effective way of tuning the chemical, physical and topological properties and increasing the environmental stability of these materials. Significant examples are hydrogenated [42] and fluorinated [144] graphene. For group-14 Xenes, the most encouraging results come from stanene. Considering SO coupling, first-principle calculations based on density functional theory, identified a gap in fluorinated stanene band structure (Figure 2.2a-b), with the valence and conduction bands degenerate at the Γ point [181]. The chemical functionalization induce a parity exchange

between occupied and unoccupied bands that is non trivial to the topology. The parity change mechanism is clarified in Figure 2.2c. Chemical functionalizatation creates a QSH insulator

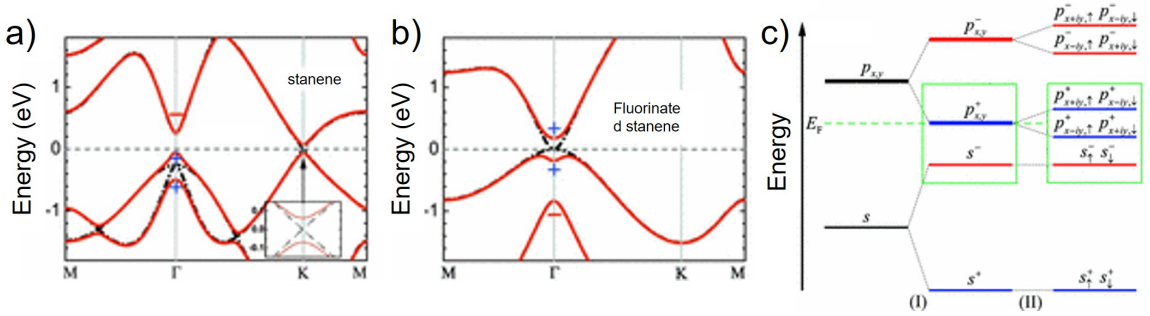

Fig. 2.2 Band structure for a) stanene and b) fluorinated stanene. Schematic diagram of the evolution from the atomic s and $p_{x,y}$ orbitals of Sn into the conduction and valence bands at the Γ point for fluorinated stanene. The p_z orbital is saturated by F, thus states around Fermi energy (green dashed line) are mainly contributed by the atomic s and $p_{x,y}$ orbitals. In stage I, the chemical bonding between Sn-Sn atoms forms bonding and antibonding states for both s and $p_{x,y}$ orbitals. The symbols "+" and "−" denote the parity of the resulting states. Before turning on SO coupling, the p_x and p_y orbitals are degenerate due to the C_3 rotation symmetry and the system is a zero-gap semiconductor. As the SO coupling is "turned on" in stage II, the degeneracy of the bonding state $\left|p^+_{x,y}\right\rangle$ is lifted, opening a full energy gap. This introduces a non-trivial insulating phase with and inverted order of $|s^-\rangle$ and $\left|p^+_{x,y}\right\rangle$. Figure adapted from Ref. [181].

with sizeble non trivial bulk gap of 0.3 eV.

Similar effects may be induced by interaction with the substrate. Tang and co-workers [161] confirmed the band inversion induced by SO coupling at the Γ point and evaluated the impact on the topological properties of stanene due to different substrates. Based on their simulations, the band inversion observed in stanene proved to be substrate-dependent and strain-sensitive, providing an opportunity to manipulate the stanene electronic properties. Electronic structure engineering and bandgap opening in Xenes are highly desirable because they would overcome the limitations of graphene, making them suitable for digital and optoelectronic applications. Clearly this approach can be generalised to other 2D materials. It finds its fullest expression in the realisation of 2D heterostructures.

2.2 The optical response

The band structure, described in the previous section, is strongly reflected in the optical response of Xenes. That is the reason why spectroscopic studies in a wide photon energy

range (generally from the THz to the UV) may help to gain information on the electronic properties, their modification by the environment and the lattice geometry. This investigation method also enables to clarify fundamental aspects of radiation-matter interaction, which are certainly useful in the perspective of developing new photonic and optoelectronic device [118]. On first approximation the linear band dispersion of Xenes and graphene, shown in Figure 2.1, can be described by an unified scheme in terms of optical transitions around the Dirac point.

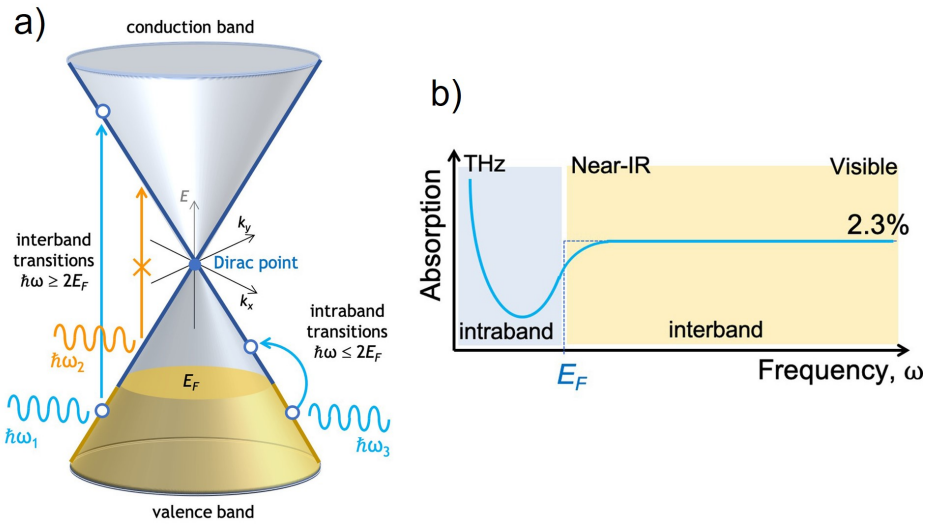

Fig. 2.3 a) Sketch of a Dirac cone that is typical of 2D Dirac system like graphene. Allowed and prohibited optical transitions are the blue and orange arrows, respectively. The Dirac point and Fermi level are reported. b) Sketch of the universal absorption in a Dirac system from the THz to the visible domain spectrum as a function of the frequency. Figure from Ref. [104].

When excited by external radiation, charges may experience interband or intraband transitions, depending on the energies involved (see Fig. 2.3). Interband transitions consist of charge carrier excitations from the valence to the conduction band. They occur at energies $\hbar\omega \geq 2E_F$, where E_F is the Fermi energy, and generally lie between mid-infrared and visible spectral regions. For graphene, the optical absorption in the mid-IR tends to assume the constant value $\pi\alpha$ due to the interband transitions, where $\alpha = 1/137$ [121, 107] is the fine-structure constant. The deviations from the constant absorbance in the low frequency limit ($\hbar\omega \leq 2E_F$) is attributable to the intraband transitions that can be reduced to a Drude behaviour of free carriers [107].

Independent quasi-particle approach

Theoretically, neglecting self-energy and excitonic effects due to the electron-electron interaction in the crystal, the quasi-constant optical absorption in the infrared spectral region appears to be a common feature of 14-group Xenes [109].

The optical absorption is determined by the imaginary part of the dielectric function $\varepsilon(\omega)$, which is related to the optical transition matrix. The general expression for 2D absorbance is:

$$A(\omega) = \frac{\omega}{c} L \, Im\{\varepsilon(\omega)\} \tag{2.5}$$

where L is the distance between the simulated layers, assuming a graphite-like superlattice arrangement, and c is the speed of light. In the independent-quasiparticle approximation, in the limit $\omega \to 0$, the absorbance approaches to $A(0) = \pi\alpha$ (with $\alpha = e^2/\hbar c$). That result is independent of the group-14 element and of the sheet buckling. The constant absorption can be explained through the conservation of the point-group symmetry of the 2D honeycomb lattice, which is maintained regardless of the buckling amount. It is worth stressing that the same result can be analytically derived using the tight-binding method [109].

In contrast to the behavior in the infrared spectral region, in the visible and ultraviolet spectral regions the absorbance shows different frequency variations for the elements of the group-14. This is due to the specific band structure of each material. The lineshape of the absorbance is determined by the van Hove singularities in the join density of states (JDOS). The calculated JDOS for graphene and silicene is shown in Figure 2.4.

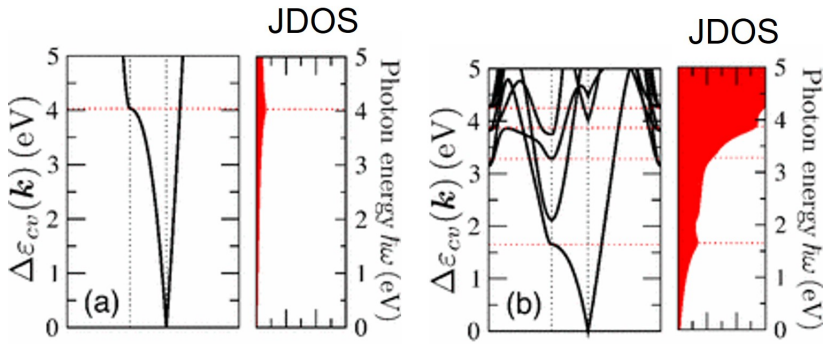

Fig. 2.4 Interband transition energies along high-symmetry lines in the Brillouin zone for a) graphene and b) silicene. The red horizontal lines indicate energies of van Hove singularities which give peak structures in the absorbance. The resulting joint densities of states are also shown in units of eV. Figure adapted from Ref. [109].

In particular, peaks and shoulders in $A(\omega)$ can be related to critical points in the 2D band structure and JDOS [40]. For example, the saddle point at the M-point in the 2D Brillouin

zone is responsible for a pronounced peak at 4.0 eV for graphene and the peak around 2 eV for Xenes.

Opening the energy band gap

As shown above, the SO coupling, as well as functionalization or interaction with different substrates, can lead to variations in the electronic band structure of Xenes. Limiting the discussion to the SO effect, it induces a fundamental gap E_g at the K point of the Brillouin zone. This produces two effects on the optical properties of Xenes in the low-frequency range: the absorbance is zero for photon energies below the gap and the first optical transitions at K point involve parabolic bands. The behavior for the absorbance near the gap can be described as follows [110]:

$$A(\omega) = \pi\alpha\left[1 + (\frac{E_g}{\hbar\omega})^2\right]\Theta(\hbar\omega - E_g) \tag{2.6}$$

In order to calculate the optical response of an isolated sheet it may be useful to introduce the 2D optical conductivity σ_{2D} [111]. In the limit of vanishing reflectivity, the 2D optical conductivity can be directly related to the absorbance through:

$$A(\omega) = \frac{1}{\varepsilon_0 c} Re\{\sigma_{2D}(\omega)\} \tag{2.7}$$

with ε_0 the vacuum dielectric constant and c the speed of light. Results of theoretical calculations based on DFT for silicene and stanene are reported in Figure 2.5. The first

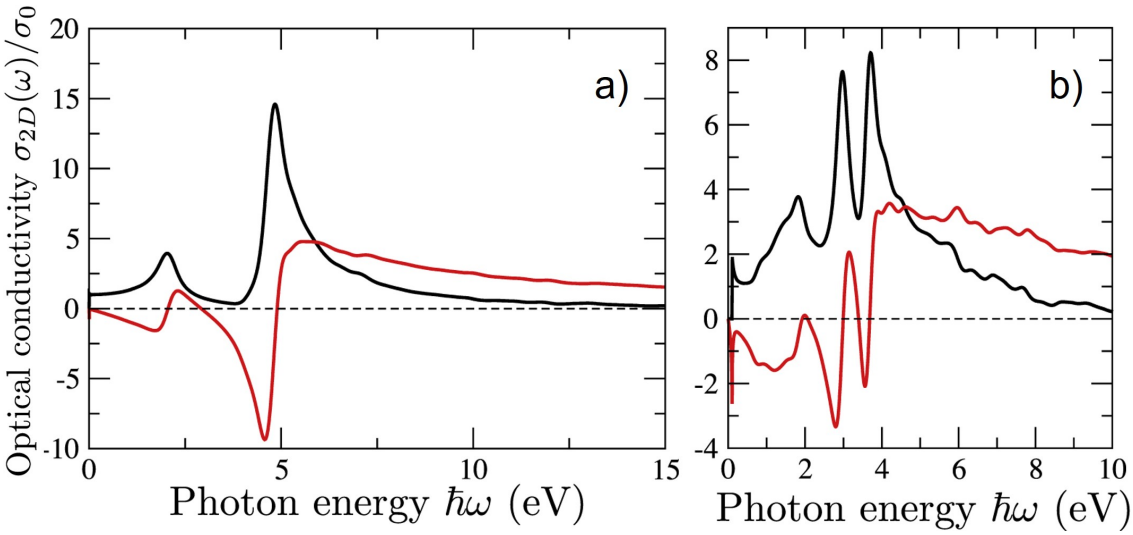

Fig. 2.5 Normalized optical conductivity of a) silicene, and b) stanene. Real part: black line, imaginary part: red line. Figure adapted from Ref. [111].

peaks near 2 eV in silicene and stanene is a consequence of the 2D saddle points in the π-π^*

interband structure located at the six M points at the Brillouin zone boundary. The higher peaks near 5 eV for silicene and 3.1/4.0 eV for stanene are related to $\sigma \rightarrow \sigma^*$ transitions mainly at the Γ point of the 2D Brillouin zone. As mentioned above, these peaks can also be related to van Hove singularities in the interband structure [111].

It is important to stress that, in general, the absorbance together with transmittance and reflectance, is a macroscopic optical property that can be determined experimentally using spectroscopic techniques. Further information on the relations between different optical properties and the models used to describe the experimental optical data can be found in Appendix A.

2.3 Principles of Plasmonics

As mentioned at the end of Section 1.2, the appearance of Dirac electrons in 2D silicon, epitaxially grown on sapphire, opens the way to the possible identification of a plasmonic response of the system.

The interaction between photons and electric dipoles can produce, in many materials, hybrid quasi-particles called polaritons. The best known physical realization of polaritons are the so-called surface plasmon polaritons (SPPs). SPPs consist of electromagnetic excitations propagating at the interface between a dielectric and a metal, evanescently confined in the direction perpendicular to the interface [106]. Plasmons enable the manipulation of light-matter interactions at sub-wavelength scale. Their small spatial extension relative to the wavelength and the huge optical enhancement (near-field intensities $> 10^5$ times larger than the incident light intensity) can be exploited in various fields. Sensing [3], imaging [103], optical modulation [156, 65] and non-linear optics [82], to name a few, are all applications that benefit from the coupling of electromagnetic waves to the collective modes of electrons in plasmonic materials. Noble metals are known to be the best plasmonic materials available [173] but have many limitations: they are difficult to tune and have large ohmic losses that restrict their applicability to devices. These restrictions have strongly driven the exploration of the plasmonic response in systems with different electronic properties. Dirac materials can be considered a clear example of this [104]. Included in the definition are the well-known graphene, topological insulators such as Bi_2Se_3, Bi_2Te_3, Sb_2Te_3 [188], Weyl semimetals like the recent $PtTe_2$ [183] and, of course, Xenes [99, 61, 56].

A general description of the properties of surface plasmon polaritons can be obtained from the macroscopic Maxwell's equations:

$$\nabla \cdot \mathbf{D} = \rho \tag{2.8a}$$

$$\nabla \cdot \mathbf{B} = 0 \tag{2.8b}$$

$$\nabla \times \mathbf{E} = -\frac{\partial \mathbf{B}}{\partial t} \tag{2.8c}$$

$$\nabla \times \mathbf{H} = \mathbf{J} + \frac{\partial \mathbf{D}}{\partial t} \tag{2.8d}$$

These equations link the dielectric displacement **D**, the electric field **E**, the magnetic field **H** and the magnetic induction **B** with the external charge and current densities ρ and **J**. These macroscopic fields are further linked via the polarization **P** and the magnetization **M** according to the equations:

$$\mathbf{D} = \varepsilon_0 \mathbf{E} + \mathbf{P} \tag{2.9a}$$

$$\mathbf{H} = \frac{1}{\mu_0}\mathbf{B} - \mathbf{M} \tag{2.9b}$$

where ε_0 and μ_0 are the electric permittivity and magnetic permeability of vacuum, respectively. Restricted to a linear, isotropic and non-magnetic media, the following relations can be defined:

$$\mathbf{D} = \varepsilon_0 \varepsilon \mathbf{E} \tag{2.10a}$$

$$\mathbf{B} = \mu_0 \mu \mathbf{H} \tag{2.10b}$$

$$\mathbf{J} = \sigma \mathbf{E} \tag{2.11}$$

with ε the dielectric constant or relative permittivity and $\mu = 1$ the relative permeability of a nonmagnetic medium, and σ the conductivity. These linear relations can be generalized taking into account the non-locality in time and space in a medium. Assuming that the length scales are significantly larger than the lattice spacing of the material (i.e. homogeneity of the medium), the response functions to an external field **E** depend on the differences of spatial and temporal coordinates:

$$\mathbf{D}(\mathbf{r},t) = \varepsilon_0 \int dt' d\mathbf{r}' \varepsilon(\mathbf{r}-\mathbf{r'},t-t')\mathbf{E}(\mathbf{r'},t') \tag{2.12a}$$

$$\mathbf{J}(\mathbf{r},t) = \int dt' d\mathbf{r}' \sigma(\mathbf{r}-\mathbf{r'},t-t')\mathbf{E}(\mathbf{r'},t') \tag{2.12b}$$

The Equations 2.12 simplify by taking the Fourier transform with respect to $\int dtd\mathbf{r}e^{i(\mathbf{K}\cdot\mathbf{r}-\omega t)}$:

$$\mathbf{D}(\mathbf{K},\omega) = \varepsilon_0\varepsilon(\mathbf{K},\omega)\mathbf{E}(\mathbf{K},\omega) \tag{2.13a}$$

$$\mathbf{J}(\mathbf{K},\omega) = \sigma(\mathbf{K},\omega)\mathbf{E}(\mathbf{K},\omega) \tag{2.13b}$$

The response of a media under an electric field is thus described by $\varepsilon(\mathbf{K},\omega)$ and $\sigma(\mathbf{K},\omega)$, both with a wavevector and a frequency dependence. The two response functions are related by:

$$\varepsilon(\mathbf{K},\omega) = 1 + \frac{i\sigma(\mathbf{K},\omega)}{\varepsilon_0\omega} \tag{2.14}$$

that follows from Maxwell's equations (Eq. 2.8).

For metals, a further simplification can be introduced due to their spatially local response. Here $\mathbf{K} \simeq 0$ and thus $\varepsilon((\mathbf{K}=0,\omega) = \varepsilon(\omega)$. This is valid as long as the wavelength λ in the material is significantly longer than all characteristic dimensions, such as the size of the unit cell or the mean free path of the electrons. This condition is in general still fulfilled at ultraviolet frequencies.

In the absence of external stimuli ($\rho = 0$, $\mathbf{J} = 0$), the characteristic wave equation can be obtained by combining the curl Equations 2.8c and 2.8d:

$$\nabla \times \nabla\mathbf{E} = -\mu_0\frac{\partial^2\mathbf{D}}{\partial t^2} \tag{2.15}$$

that can be rewritten in the Fourier reciprocal space by means of the identities $\frac{\partial}{\partial t} \rightarrow -i\omega$ and $\nabla = \mathbf{K}$ as:

$$\mathbf{K}(\mathbf{K}\cdot\mathbf{E}) - K^2\mathbf{K} = -\varepsilon(\mathbf{K},\omega)\frac{\omega^2}{c^2}\mathbf{E} \tag{2.16}$$

where $c = \frac{1}{\sqrt{\mu_0\varepsilon_0}}$ is the speed of light in vacuum. Depending on the polarization of the electric field vector two cases can be distinguished:

- Transverse waves, $(\mathbf{K}\cdot\mathbf{E} = 0) \rightarrow \mathbf{K}^2 = \varepsilon(\mathbf{K},\omega)\frac{\omega^2}{c^2}$
- Longitudinal waves $\rightarrow \varepsilon(\mathbf{K},\omega) = 0$

At this point it is useful to introduce the Drude model. The Drude approach allows to describe the response of a gas of free electrons moving against a fixed background of positive ion cores when an electromagnetic field is applied. A simple equation for the motion of an electron of mass m and charge $-e$ in a plasma sea, subjected to an external electric field $\mathbf{E}$ is:

$$m\ddot{x} + m\gamma\dot{x} = -e\mathbf{E} \tag{2.17}$$

The motion is damped via collision occurring with a characteristic collision frequency $\gamma = 1/\tau$, where τ is the relaxation time. By assuming an harmonic time dependence of the electric field $\mathbf{E}(t) = \mathbf{E}_0 e^{-i\omega t}$ and according to the definition of the electrical polarization $P = -ne\mathbf{r}(t)$ it can be wrote:

$$\mathbf{P} = -\frac{ne^2}{m(\omega^2 + i\gamma\omega)}\mathbf{E}(t) \tag{2.18}$$

By replacing this expression in the Equation 2.9a the dielectric function becomes:

$$\varepsilon(\omega) = 1 - \frac{{\omega_p}^2}{\omega^2 + i\gamma\omega} \tag{2.19}$$

The quantity ${\omega_p}^2 = \frac{ne^2}{\varepsilon_0 m}$, introduced in Equation 2.19 is the plasma frequency of the free electron gas with n the number density of the free electron gas. Similarly, a new expression can be introduced for the conductivity:

$$\sigma(\omega) = \frac{\sigma_0}{1 - i\omega\tau} \tag{2.20}$$

defining the dc-conductivity as $\sigma_0 = \frac{ne^2\tau}{m} = {\omega_p}^2\tau\varepsilon_0$.

The effect of the electromagnetic field impinging on a metal is to displace free electrons from their position. This leads to a lack of negative charge, resulting in a coulombic attraction that forces them to return to their original position. The resulting oscillating charge-density gives rise to volume plasmons. The plasma frequency $\omega_p = \sqrt{ne^2/\varepsilon_0 m}$ can thus be recognized as the natural frequency of a free oscillation of the electron sea.

It is worth noting that, in general, the Drude model can be used to describes the optical response of metals for photon energies below the threshold of inter-band transitions. Further details on the description of the optical properties of solids through classical models can be found in Appendix A.

2.3.1 Surface plasmon polaritons

At the interface between a dielectric and a conductor, the coupling of the electromagnetic field to charge-density oscillations determines surface plasmon polaritons (SPPs). In a classical picture SPPs are particular solutions of Maxwell's equations (Eq. 2.8) that appear for specific boundary conditions [130]. In order to define the propagation geometry a simple interface between two media can be considered, as reported in Figure 2.6. For $z < 0$ there is a metal, which is described via a dielectric function $\varepsilon_1(\omega)$, while for $z > 0$ there is a non-absorbing

half space characterized by a positive dielectric constant ε_2. It is worth noting that the requirement of metallic character implies $Re[\varepsilon_1] < 0$ and for noble metals this condition is fulfilled at frequencies below the plasma frequency ω_p defined in the previous paragraph. The plane $z = 0$ coincides with the interface sustaining the propagating waves.

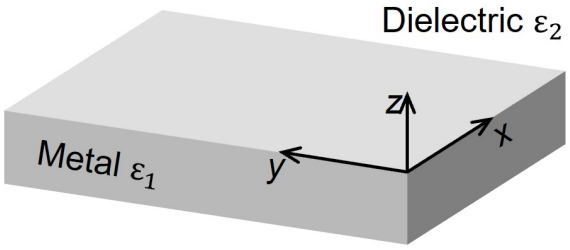

Fig. 2.6 Sketch of the interface between two materials. The waves propagate along the x-direction in a cartesian coordinate system.

If for simplicity the waves are assumed to propagate along the x direction, the electric field is $\mathbf{E}(x,y,z) = \mathbf{E}(z)e^{i\beta z}$, with $\beta = k_x$. The last parameters is called the propagation constant of the traveling waves and corresponds to the component of the wave vector in the direction of propagation. In the absence of external charge and current densities, the Equations 2.8c and 2.8d can be combined, resulting in the Equation 2.15. Using the identities $\nabla \times \nabla \times \mathbf{E} = \nabla(\nabla \cdot \mathbf{E}) - \nabla^2\mathbf{E}$ as well as $\nabla \cdot (\varepsilon\mathbf{E}) = \mathbf{E} \cdot \nabla\varepsilon + \varepsilon\nabla \cdot \mathbf{E}$, in the absence of external stimuli the wave equation describing the surface wave becomes:

$$\frac{\partial^2\mathbf{E}(z)}{\partial z^2} + (k_0^2\varepsilon - \beta^2)\mathbf{E} = 0 \tag{2.21}$$

where $k_0 = \omega/c$ is the wavevector of the propagating wave in vacuum. The Equation 2.21 must be satisfied for both media and a similar one can be found also for the magnetic field [106]. At this point, returning to Maxwell's equations 2.8c and 2.8d, and assuming harmonic time dependence ($\frac{\partial}{\partial t} = -i\omega$), the explicit expressions for the different components of electric and magnetic fields become:

$$\frac{\partial E_y}{\partial z} = -i\omega\mu_0 H_x \tag{2.22a}$$

$$\frac{\partial E_x}{\partial z} - i\beta E_z = i\omega\mu_0 H_y \tag{2.22b}$$

$$i\beta E_y = i\omega\mu_0 H_z \tag{2.22c}$$

$$\frac{\partial H_y}{\partial z} = i\omega\varepsilon_0\varepsilon E_x \tag{2.22d}$$

$$\frac{\partial H_x}{\partial z} - i\beta H_z = -i\omega\varepsilon_0\varepsilon E_y \tag{2.22e}$$

$$i\beta H_y = -i\omega\varepsilon_0\varepsilon E_z \tag{2.22f}$$

where the propagation along the x-direction ($\frac{\partial}{\partial x} = i\beta$) and the homogeneity in the y-direction ($\frac{\partial}{\partial y} = 0$) have been considered. This system of equations allows two set of self-consistent solutions with different polarization properties of the propagating waves: the transverse magnetic modes (TM or p) where only the components E_x, E_z and H_y are non-zero and the transverse electric modes (TE or s) with non-zero H_x,H_z and E_y.

For the simple geometry reported in Figure 2.6 the TM solutions are:

$$\text{for z>0} \begin{cases} H_y(z) = A_2 e^{i\beta x} e^{-k_2 z} \\ E_x(z) = iA_2 \frac{1}{\omega\varepsilon_0\varepsilon_2} k_2 e^{i\beta x} e^{-k_2 z} \\ E_z(z) = -A_1 \frac{\beta}{\omega\varepsilon_0\varepsilon_2} e^{i\beta x} e^{-k_2 z} \end{cases}$$

$$\text{for z<0} \begin{cases} H_y(z) = A_1 e^{i\beta x} e^{k_1 z} \\ E_x(z) = -iA_1 \frac{1}{\omega\varepsilon_0\varepsilon_1} k_1 e^{i\beta x} e^{k_1 z} \\ E_z(z) = -A_1 \frac{\beta}{\omega\varepsilon_0\varepsilon_2} e^{i\beta x} e^{k_1 z} \end{cases}$$

The reciprocal value of $k_{1,2}$, which is the component of the wavevector perpendicular to the interface in the two media, defines the evanescent decay length of the fields perpendicular to the interface and quantifies the confinement of the wave. The continuity conditions imposed on H_y and εE_z at the interface require that $A_1 = A_2$ and

$$\frac{k_2}{k_1} = -\frac{\varepsilon_2}{\varepsilon_1} \tag{2.23}$$

Following the last conditions is evident that the surface waves exist only at interfaces between materials with opposite signs of the real part of their dielectric permittivities (i. e. between a conductor and an insulator). In addition, the continuity condition for H_y across the interface leads to:

$$k_1^2 = \beta^2 - k_0^2\varepsilon_1 \tag{2.24a}$$

$$k_2^2 = \beta^2 - k_0^2\varepsilon_2 \tag{2.24b}$$

The dispersion relation of SPPs propagating at the interface between a metal and an insulator is obtained by combining the last three equations:

$$\beta = k_0 \sqrt{\frac{\varepsilon_1\varepsilon_2}{\varepsilon_1 + \varepsilon_2}} \tag{2.25}$$

This expression also applies in the presence of damping inside the metal and thus for a complex dielectric function. Obviously, complex values will also be obtained for β.

Following the same procedure for the TE modes, the continuity conditions at the interface for the field components are only fulfilled if $A_1 = A_2 = 0$. This means that all the fields are equal to zero, so surface plasmon polaritons can only exist for TM polarization. To figure out the properties of SPPs, starting from the dispersion relation, it could be useful to introduce real values for the dielectric functions of different materials. In Figure 2.7 is shown the real

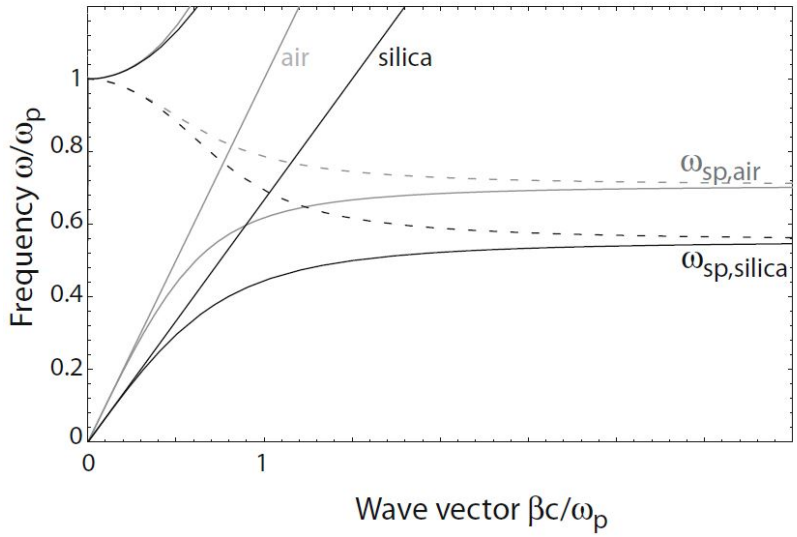

Fig. 2.7 Dispersion relation of SPPs at the interface between a Drude metal with negligible collision frequency and air (gray curves) and silica (black curves)[106].

and imaginary part of the wavevector β, at the interface between a metal described by the real Drude dielectric function and air ($\varepsilon_2 = 1$) or fused silica ($\varepsilon_2 = 2.25$). In the following an ideal conductor, without damping effect is assumed. The constrained nature of SPPs means that they appear to the right of the respective air and silica light lines. That is why phase-matching techniques such as grating coupling are required for their excitation via three-dimensional beams. Radiation into the metal occurs in the transparency regime, for $\omega > \omega_p$. Between the regime of the bound and radiative modes, a frequency gap region with purely imaginary β that forbids the propagation. For small wavevectors, corresponding to mid-infrared or lower frequencies, the SPP propagation constant is close to k_0 at the light line, and the waves extend over many wavelength in the dielectric space. In the opposite regime of large wavevectors, the frequency of the SPPs approaches the characteristic surface plasmon frequency:

$$\omega_{sp} = \frac{\omega_p}{\sqrt{1+\varepsilon_2}} \tag{2.26}$$

This expression can be obtained putting the free-electron dielectric function into the Equation 2.25. In the limit of negligible damping of conduction electron oscillations, the wavevector β goes to infinity as the frequency approaches ω_{sp} and the group velocity approaches 0. In this way the modes acquires electrostatic character and are known as surface plasmons. It is important to stress that in real metals, the conduction electrons suffer both from free-electron and interband damping. In this case the dielectric function $\varepsilon_1(\omega)$ is complex and with it also the propagation constant. The traveling SPPs are damped with an energy attenuation length given by:

$$L = \frac{1}{2Im[\beta]} \tag{2.27}$$

Thus, by replacing a real metal dielectric function in the Equation 2.25, a different dispersion curve is obtained. The result for the case of silver/air and silver/silica interface is reported in Figure 2.8. In contrast to completely undamped SPPs, the bound SPPs approach a finite

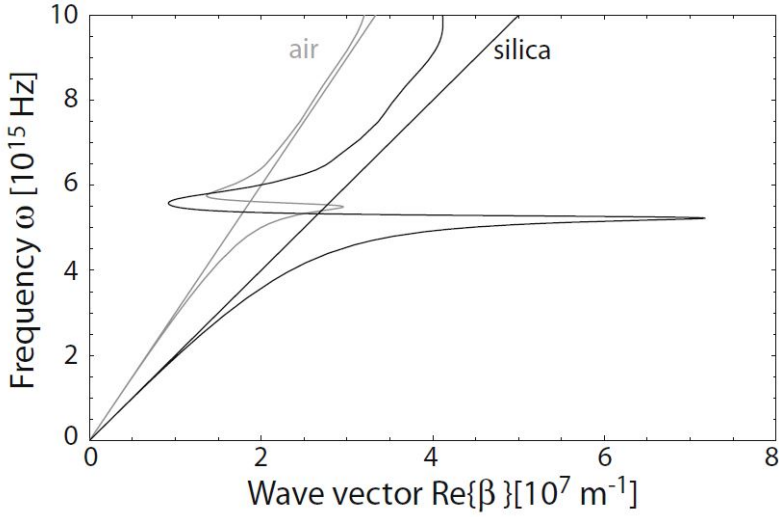

Fig. 2.8 Dispersion relation of SPPs for silver/air (gray curves) and silver/silica (black curves) interfaces. The limit for the surface plasmon frequency is achieved due to damping effects [106].

wavevector at the surface plasmon frequency ω_{sp} of the system. This results in a lower limit both on the surface plasmon wavelength $\lambda_{sp} = 2\pi/Re[\beta]$ and on the confinement perpendicular to the interface, since the SPP fields in the dielectric fall off as $e^{-|k_z||z|}$ with $k_z = \sqrt{\beta^2 - \varepsilon_2(\frac{\omega}{c})^2}$. A characteristic trade-off between localization and loss is typical for SSPs: the better the confinement, the lower propagation length. To conclude this section, it is important to stress that in multilayered system consisting of alternating conducting and dielectric thin films, each single interface can show bound SPPs. If the separation between

adjacent interfaces is comparable to or smaller than the decay length of the interface mode, interaction between SPPs give rise to coupled modes.

2.3.2 Surface plasmon polaritons excitation

As mentioned in the previous paragraph the SPPs are highly confined modes at the interface between a conductor and a dielectric. The propagation constant β indeed is greater than the wavevector in the dielectric and this results in an evanescent dacay on both sides of the considered interface. An additional source of lateral momentum is needed to break the optical momentum mismatch and allow a direct light-plasmon coupling. Prism coupling, grating coupling or excitation upon charged particle impact are just some of the techniques that can be applied in order to provide the extra-momentum needed to observe SPPs.

In this work the grating coupling approach was followed in order to excite the SPPs with light. In this method the increase of the wavevector necessary to match the surface plasmon momentum is achieved by adding reciprocal lattice vector of a periodic grating G to the free-space wavevector [142]. In general, the conductor surface has to be structured with a certain periodicity P over an extended spatial region. For a one-dimensional grating the new in plane wavevector is $k' = k + G$, with $G = n2\pi/P$ a reciprocal lattice-vector of the grating. Thus, from a conceptual perspective, an array of parallel stripes (Figure 2.9) represents the simplest geometry to realise, allowing extra-wavevectors to be related directly to the period of the stripes. In fact, several factors can affect the quality of the stripes. It is important

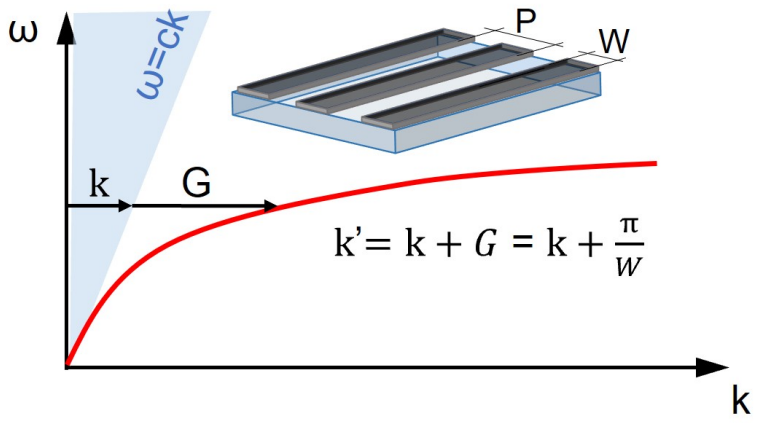

Fig. 2.9 Array of parallel stripes with period and width equal to 2W and W, respectively, provides an extra wavevector $G = 2\pi/2W$. The red curve describes the plasmon dispersion. In the absorption process G is added to the light momentum k in order to match the light dispersion with the plasmon one.

to stress that all possible SPP frequencies can not be excited through the grating coupling. When the period of the structure is half that of the effective wave-length of the SPP mode, scattering may lead to the formation of SP standing waves and the opening of an SPP stop band.

Finally, it should be noted that localised surface plasmons have been excluded from this discussion. They are confined modes on to the boundary of metal structures of sub-wavelength dimensions, such as nanoparticles. The frequency and width of these modes are determined by the particle's shape, material, size and environment and they underlie spectroscopic techniques such as surface-enhanced Raman scattering (SERS) [75, 124].

2.3.3 Plasmons in 2D- electron gases

Even though plasmonic modes can exist in every dimension, 2D plasmons have a set of features that strongly distinguish them from their 3D counterparts. In a 2D material, electrons are confined by the attractive potential of the lattice ions that blocks their motion perpendicular to the plane. At the same time, the electric field produced by the electrons still propagates in 3D space. The main consequence of this is the lack of screening of the electric field, which leads to a strongly interacting systems. In order to describe the plasmonic response in low dimension systems a general theory for long-wavelength plasma oscillations in a solid must be introduced. The main result of the discussion in Das Sarma and Hwang's work [146] is summarised by the formula defining the plasma frequency of a 2D electron system with parabolic energy-momentum dispersion:

$$\omega_p \sim \sqrt{\frac{2\pi e^2 n}{2\kappa m}} q^{1/2} \tag{2.28}$$

where e is the electron charge, n is the carrier density per unit of volume, m is the carrier mass and κ is a background dielectric constant. At this point, it is possible to specify the behaviour of a system where charged carriers obey the Dirac equation. In this case the energy-momentum dispersion is linear and it is given by $\xi = \hbar v_F$ where v_F is the Fermi velocity. The expression of the Dirac 2D plasma become:

$$\omega_p \sim \sqrt{\frac{e^2}{(\kappa \hbar v_F)}} (g\pi n)^{1/4} v_F q^{1/2} \tag{2.29}$$

where $g = g_s g_v$ is the degeneracy factor, with g_s and g_v the spin and valley degeneracy, respectively. Both the reported equations show the same dependence from the momentum ($\sqrt{q}$). Conversely, the carrier density dependence of the Dirac system is different from the

classical 2D electron gas. It is $\omega_p \propto n^{1/4}$ for Dirac plasmons and $\propto n^{1/2}$ for the conventional system.

Observation of Dirac plasmons in graphene

The first observation of Dirac plasmons on graphene has been reported by Ju and co-workers [79] in 2011. They studied tunable plasmon excitations using Fourier transform terahertz (THz) spectroscopy. Graphene was grown via chemical vapour deposition on copper and then transferred onto a Si/SiO_2 wafer. Its surface was patterned forming micro-ribbon arrays of different widths W and period 2W, in order to provide the extra momentum $G = \pi/W$ required for the photon absorption process.

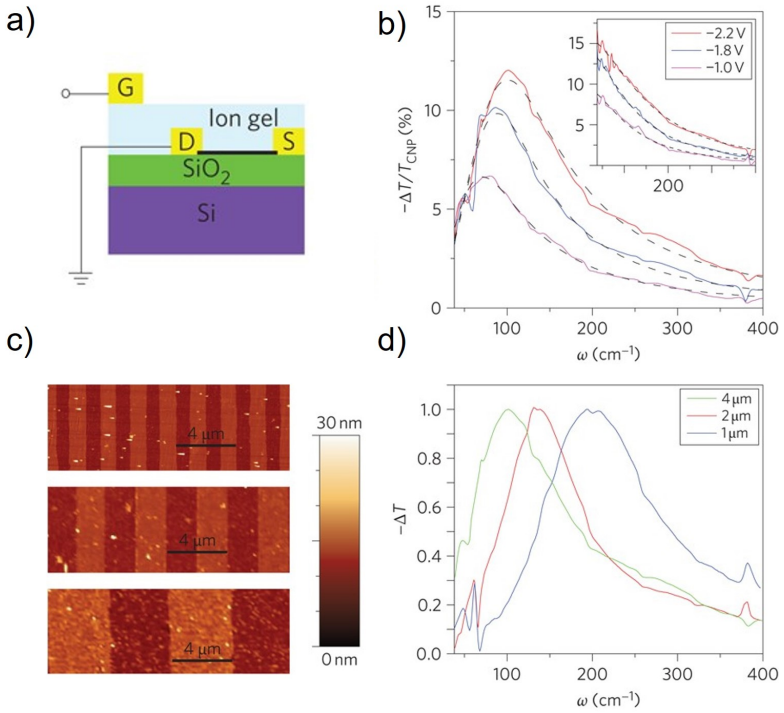

Fig. 2.10 a) Side view of the device based on graphene micro-ribbon array on a Si/SiO_2 substrate. The carrier concentration in graphene is controlled using the ion-gel top gate. b) Control of the plasma resonance through electrical gating. THz radiation was polarized perpendicular to the graphene ribbons. The plasmon resonance shifts to higher energy and gains intensity with increased carrier concentration. The inset show the spectra for THz radiation polarized parallel to the ribbons. c) AFM image of graphene micro-ribbon array sample. d) Change of transmission spectra with different graphene micro-ribbon widths for the same doping concentration. Adapted from Ref. [79].

Different values of W allowed to map the dispersion curve of the surface plasmons with momentum. Moreover, plasmon excitations in patterned graphene were controlled by

tuning the carrier concentration using an ion-gel top gate. The device structure and the AFM image of a graphene micro-ribbon array are shown in Figure 2.10a and Figure 2.10c, respectively. The light absorption was evaluated by reporting the change of transmission spectra at different gate voltage and different ribbon widths. For incident light polarized along the ribbons, the optical response was well described by the Drude model. On the other hand, for incident light polarized perpendicular to the ribbon, they observed an absorption peak originating from plasmon oscillations. The spectra as function of frequency are reported in Figure 2.10b and Figure 2.10d. For a given carrier concentration the plasmon resonance frequencies are described by the scaling behaviour of $\omega_p \propto W^{1/2}$, which is characteristic of 2D electron gases. The dependence on the carrier density is instead $\propto n^{1/4}$ that is a clear signature of Dirac electrons.

A similar experiment was carried out to study the response of graphene plasmons at higher frequencies, in the mid-infrared spectral range. In that occasion, Yan and colleagues [182] realized nanometric structures (~ 50) nm on graphene surface transferred onto two different substrates: SiO_2/Si and diamonds-like-carbon (DLC) on Si. The extinction spectra of a ribbon array on SiO_2 for parallel and perpendicular polarization of light is reported in Figure 2.11a. The resonance peaks in the extinction spectrum with perpendicular polarization are the result of excitation of localized graphene plasmons.

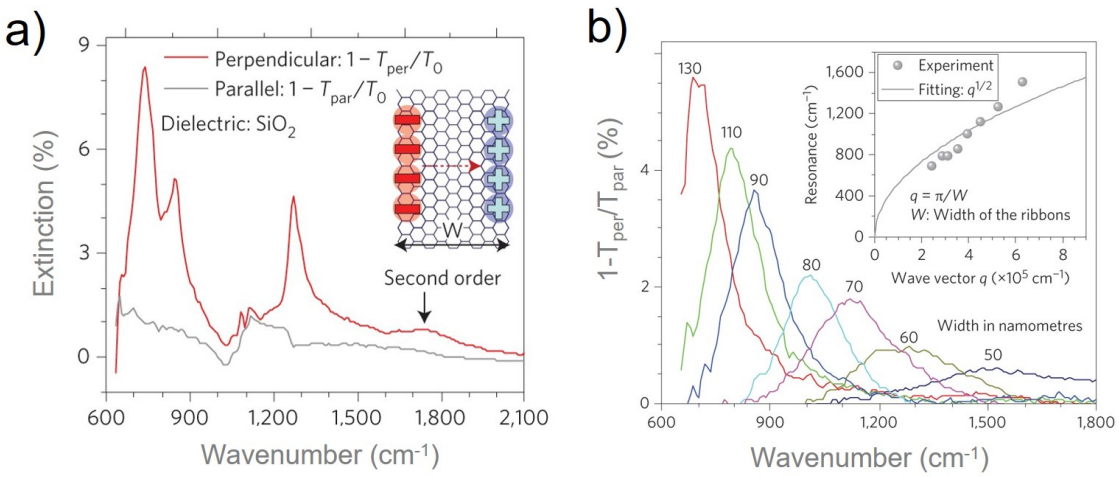

Fig. 2.11 a) Extinction spectra of a ribbon array on SiO_2 for the two polarizations of light (perpendicular-red, parallel-gray). The inset shows a sketch of the dipole oscillation in a graphene ribbon. b) Extinction spectra of graphene ribbons on DLC for different ribbon widths. The inset shows the plasmons resonance frequency as a function of the wavevector $q = \pi/W$ where W is the width of the nanoribbon. The gray curve is a fit according to $\omega_p = \sqrt{q}$. Adapted from Ref. [182].

In panel b of Figure 2.11 is shown the extinction spectra of graphene ribbons on DCL with different ribbon widths. They explained the discrepancy between the experimental data and the expected scaling ($\sqrt{\pi/W}$) as en effect of ribbon edges. By comparing the optical response of nano-ribbons in the two configurations, they found that plasmons lifetimes and propagation distances were strongly affected by interactions with substrate phonons and intrinsic graphene optical phonons, unlike in the THz spectral range. Plasmons can decay via optical phonon emission.

Overall, graphene has emerged as an alternative 2D plasmonic material due to its remarkable optical and plasmonic properties. The linear dispersion of the Dirac fermions hosted in graphene band structure enables broad band applications, in which electric gating can be used to induce changes in its optical and plasmonic properties.

In light of the data and considerations outlined so far, we therefore wonder whether Xenes, properly supported or possibly decoupled from the native substrate, can also meet the demand for new functionalities to be exploited in the development of new photonic and optoelectronic devices.

Chapter 3

Synthesis, characterization and processing

This chapter introduces the main experimental techniques used to obtain the results presented in this thesis. The first part is devoted to the description of molecular beam epitaxy (MBE) growth technique, employed to fabricate all the Xene-based configurations discussed in the following sections. The working principles of the X-ray photoelectron spectroscopy (XPS) and the low energy electron diffraction (LEED) are then described. These techniques were used to gain information on the chemical status and the crystalline structure of the samples before removing them from ultra-high vacuum conditions. Outside the growth chamber, the main characterisation methods involved spectroscopic techniques. Near Infrared-Ultraviolet (NIR-UV) Dispersive Spectrometry, Fourier Transform Infrared Spectroscopy (FTIR) and Raman spectroscopy are non-destructive optical techniques extremely useful for the evaluation of the optical and the structural properties of 2D materials. Opto-thermal Raman spectroscopy is also described. This approach provides information about the thermal behaviour of materials under investigation. As far as the plasmonic device fabrication is concerned, the optical lithography and the ionic liquid gating method, used respectively to fabricate periodic patterns and to control their electronic response, are described in the last part of this chapter.

3.1 Synthesis of Xenes

Although freestanding silicene and stanene can exist, there are no crystals made up of layers that can be peeled off, as is the case with van der Waals materials. Physical Vapour Deposition (PVD) methods were the first response to the need for experimental realisation of Xenes.

In a PVD process, the starting material is brought into the vapour phase, usually by means of thermal evaporation, and is then condensed onto a target substrate. The entire process takes place under high vacuum or ultra-high (UHV) conditions, allowing the vapour phase particles to travel to the target substrate without colliding with the background gas.

The interaction between the substrate and the deposited material is of fundamental importance for the final result of the growth. If this interaction is strong enough, the growth proceeds by forming an ordered crystalline layer on a substrate with the same normal orientation, according to precise symmetry and commensurability with respect to the substrate. This process is known as epitaxial growth or epitaxy.

There are three main approaches to epitaxial growth of Xenes: i) epitaxy by deposition, ii) epitaxy by segregation, and iii) epitaxy by intercalation [62, 46]. In epitaxy by deposition, atoms evaporated from a source under UHV conditions condense and self-organize on a substrate. This is a non-equilibrium or kinetically driven process where the choice of substrate and the fine tuning of growth parameters (mainly substrate temperature and deposition flux) are key factors in the successful formation of a 2D epitaxial lattice. Silicene on Ag is a typical example [48, 5]. Epitaxy by segregation requires the interdiffusion of precursor atoms through a substrate deposited on an underlying precursor reservoir. The diffused atomic species then self-organise into a 2D epitaxial lattice according to the commensurability relationship with the substrate. An example of this approach is silicene grown on ZrB_2 [54]. Finally, in the epitaxy by intercalation the atoms of the precursor material are evaporated from a source onto a matrix crystal, which may be either permeable to the precursor atomic species or prone to react with them, self-organising into a 2D epitaxial lattice according to the symmetry imposed by the substrate. An example of this situation is silicene intercalated between graphene and a Ru(0001) substrate [91].

The Xene-based configurations analysed in this thesis were all grown via epitaxy by deposition, which is commonly carried out by Molecular Beam Epitaxy (MBE). The MBE process involves the reaction of one or more thermal molecular beams with crystalline surface, under UHV conditions. MBE leads to a process characterised by extremely low evaporation and deposition rates, enabling kinetically controlled growth with atomic precision.

3.1.1 Molecular Beam Epitaxy Systems

Based on the substrate used for growth, the samples analysed in this work can be divided into two categories. The first includes samples grown on Al_2O_3(0001), while the second includes samples grown on Ag(111). Each group was grown in a dedicated MBE system. The two reactors are briefly described below.

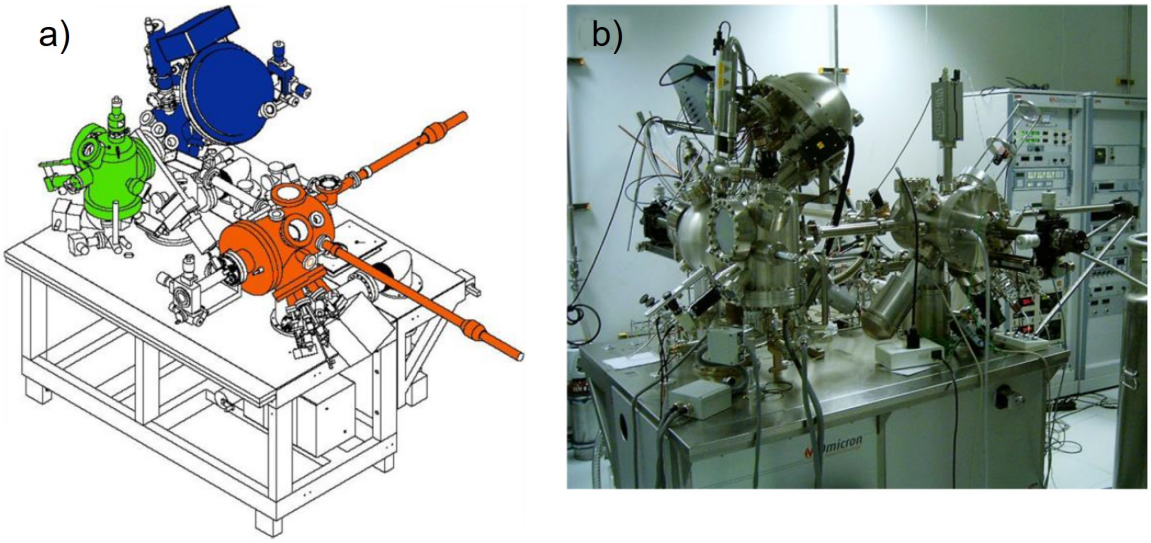

Fig. 3.1 a) Scheme of the Omicron NanoTechnology GmbH MBE system used for growing Xenes on $Al_2O_3(0001)$ substrates. Preparation, XPS analysis and SPM chambers are highlighted in orange, blue and green, respectively. b) Picture of the system.

The experimental system Omicron NanoTechnology GmbH used to grow and characterize in situ Al_2O_3-supported samples is shown in Figure 3.1. It consist of three interconnected chambers kept at a base pressure of $\sim 10^{-10}$ mbar: a preparation chamber (orange), ad analysis chamber for X-Ray Photoelectron Spectroscopy (XPS) (blue) and a Scanning Probe Microscopy (SPM) chamber (green). The XPS chamber is used to determine the atomic species in the as-prepared samples and to analyse their chemical state, while the SPM chamber is used for *in-situ* morphological characterisation of the sample surface. It is important to stress that the latter technique was not used to characterize Xenes grown on Al_2O_3 substrates. Samples can be loaded into (or unloaded from) the system via a fast-entry lock, and transferred between chambers using dedicated sample holders moved by magnetic manipulators. Precision-manipulators are used to move and position samples in both the preparation and XPS/SPM chambers.

The ScientaOmicron LAB10 MBE system was used for Ag-supported sample production. The setup is shown in Figure 3.2. Again, it is possible to identify three interconnected environments kept under ultra-high vacuum conditions: i) a loading chamber, ii) a preparation chamber and iii) a growth chamber. The growth chamber is equipped with Low Energy Electron Diffraction (LEED) and Auger Electron Spectroscopy (AES) tools. These techniques share the same electron source and are used for the *in situ* characterization of the epitaxial films. LEED allows surface crystallography to be analysed, while AES is used to determine the surface chemical composition and depth profile of samples. The sample transfer is done

Fig. 3.2 Picture of the ScientaOmicron LAB10 MBE system used for the growth of Xenes on Ag(111) substrate.

manually using precision-manipulators. The more compact structure of the LAB10 MBE system together with the MISTRAL control system, facilitate the user management.

The procedure for the growth of the samples is the same for both systems, with minor variations in the preparation of the two types of substrate. Substrate preparation is required to ensure optimum crystalline quality of epitaxial films. This step is typically performed by repeated sputtering and annealing, using an ion sputter gun and resistive heaters. Ion sputtering removes all organic contaminants from the substrate surface using a directional beam of high-energy inert gas ions (Ar^+). The sputtered surface is then thermally annealed to restore its crystalline periodicity. After substrate surface preparation, thin films can be grown using various effusive sources for the UHV evaporation. The UHV status during the evaporation of the atomic or molecular species is cross-checked with a residual gas analyzer (RGA) attached to the preparation chamber.

The epitaxial deposition of tin on $Al_2O_3(0001)$ was carried out using a Knudsen cell (k-cell). The synthesis of epitaxial silicon on $Al_2O_3(0001)$ was performed by resistive evaporation from an intrinsic silicon wafer, brought to sublimation temperature by an external generator. The synthesis of stanene on Ag(111) was performed though a k-cell while silicene on Ag(111) was deposited employing a silicon sublimation source. In both MBE systems, the Al films used to synthesise the protective capping layer described in Section 1.2 were evaporated using a k-cell. The voltage and current supplied to the sources is controlled externally to achieve the appropriate evaporation temperature. A thickness monitor based on

a quartz crystal microbalance is provided in both MBE chambers to allow correct growth rate calibration.

3.2 In-situ characterization

The XPS and LEED characterisation methods, used for the *in situ* characterization of Xene-based samples, are briefly described below.

3.2.1 X-Ray Photoelectron Spectroscopy

Composition of thin films and chemical bonding at the interface between thin films and substrate were investigated by X-Ray Photoelectron Spectroscopy (XPS). The physical principle of the XPS is the photoelectric effect [73]. XPS analysis is thus based on the electronic photoemission from a core level induced by a X-ray irradiation. The physical process is schematically represented in Figure 3.3b. A photon, with energy in the soft X-ray range (<2 KeV), impinges on a sample and photo-ionizes the core-energy level of the atoms in the material. The excited electrons travel through the sample to the surface, escape into the vacuum and are collected by an analyzer that determines their kinetic energy (E_{kin}). The XPS sampling depth is limited by the inelastic mean free path of photoelectrons inside the thin film, i. e., the average length that a photoelectron may cover before losing energy in inelastic scattering. This limitation makes XPS analysis effective only nearby the surface region of the samples. Within this restriction, the sampling depth can be varied by tuning the angle formed by the photoelectrons and the impinging X-ray beam (take-off angle). Deeper and more superficial regions can be probed in a close-to-normal photoemission configuration ($\theta \sim 90°$) and for smaller take-off angles, respectively.

Assuming that the interaction between the escaping electron and the system is instantaneous, it is possible to calculate the kinetic energy of the escaping photoelectron E_{kin} in terms of its core-level binding energy (E_B), as illustrated in the diagram of Figure 3.3b:

$$E_{kin} = h\nu - E_B - \phi_{spec}$$

where $h\nu$ is the energy of the incoming X-Ray photon, ϕ_{spec} is the work-function of the spectrometer and E_B is the core-level binding energy of the electron. By convention it is expressed as a positive quantity with respect to the Fermi level of the system. By fixing the work-function of the analyzer and the energy of the incoming photons, the kinetic energy of the electrons determines their binding energy and vice versa. The intensity as a function of the binding energy of the emitted core electrons is therefore always given by an XPS

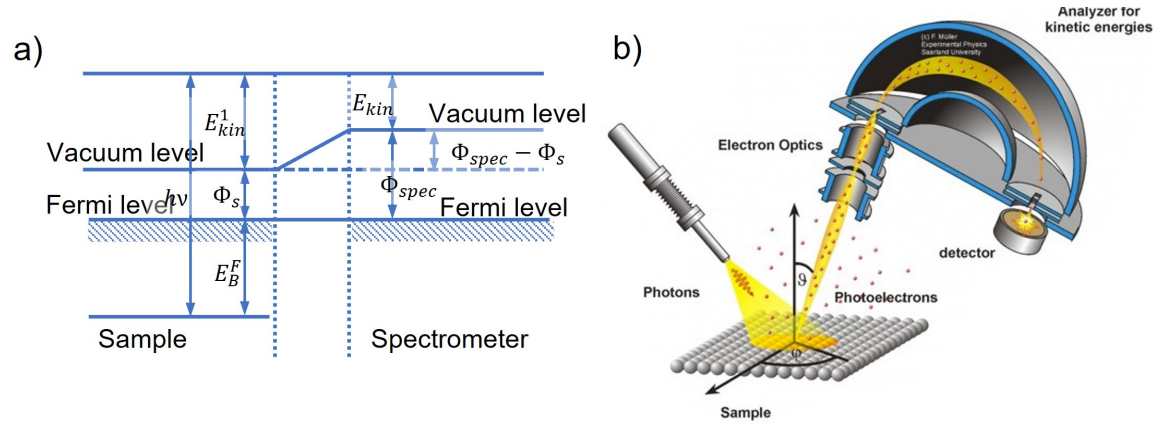

Fig. 3.3 a) Energy levels diagram for the determination of the binding energy of the photoemitted electron. The kinetic energy measured by the spectrometer E_{kin} is different from the kinetic energy referred to the sample vacuum level E^1_{kin}. This is due to the difference between the work function of the spectrometer Φ_{spec} and of the sample Φ_s. b) Sketch of an XPS experiment.

spectrum. The latter quantity varies between the chemical elements and, for a given element, it is also influenced by the nature of the chemical bond. Therefore, by studying the peak positions in the XPS spectra it is possible to quantify the atomic species and how these species are chemically bonded to each other.

In the present work the XPS measurements on Sn nanosheets deposited on $Al_2O_3(0001)$ and on graphene-$Al_2O_3(0001)$ substrates were carried out by means of a non-monochromatic X-Ray source. It was equipped with a standard magnesium anode at an emission energy of 1253.6 eV (Mg K_α X-Ray line). A hemispherical energy analyser with a pass energy of 20 eV was used to collect the kinetic energy of emitted photoelectrons. The take-off angle was set at $\theta = 53°$so that the emitted photoelectrons probed only the atomic species at the surface of the as-deposited epitaxial 2D materials.

3.2.2 Low Energy Electron Diffraction

A Low Energy Electron Diffraction (LEED) experiment can provide different information. In this work diffraction patterns were used to check the quality of the substrate surface after the preparation and to obtain the surface symmetry and reconstruction of Xenes grown on Ag(111). The principle behind a LEED experiment is the elastic back-scattering of low energy electrons incident normally on a crystal surface. There is a direct correspondence between the observed diffraction pattern and the reciprocal lattice of the surface. The following relationships express the key requirements for obtaining a LEED pattern. In particular, the

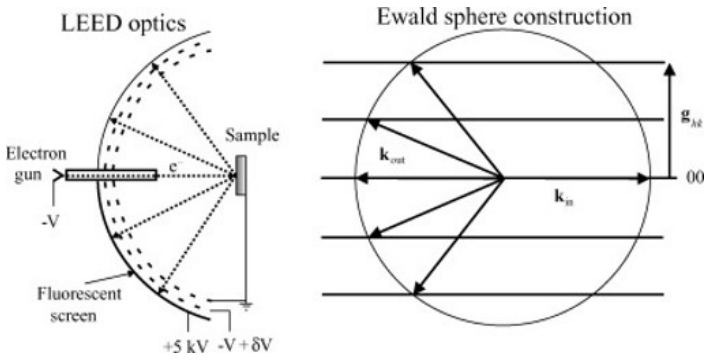

Fig. 3.4 Scheme (left) of the basic setup used in a LEED experiment. The geometry of the experiment is compared to the Ewald sphere construction. It is a consequence of the conservation of energy and electron momentum parallel to the surface for a 2D periodic surface. The horizontal lines shown in the construction are the 'reciprocal lattice rods'. Image adapted from Ref. [175].

components of the incident and scattered electron wavevector parallel to the surface obeys to:

$$\mathbf{k}_{out} = \mathbf{k}_{in} + \mathbf{g}_{hk}$$

where the reciprocal lattice vector is

$$\mathbf{g}_{hk} = h\mathbf{a}^* + k\mathbf{b}^*$$

and the primitive translation vectors of the reciprocal net $\mathbf{a}^*$ and $\mathbf{b}^*$ are defined as:

$$\mathbf{a}^* = 2\pi\frac{\mathbf{b}\times\mathbf{n}}{A}$$

$$\mathbf{b}^* = 2\pi\frac{\mathbf{n}\times\mathbf{a}}{A}$$

where $A = \mathbf{a}\times\mathbf{b}\cdot\mathbf{n}$, $\mathbf{n}$ is the unit vector normal to the surface and $\mathbf{a}$ and $\mathbf{b}$ are the primitive translation vectors defining the periodicity of the sample parallel to the surface [175]. A simplified version of the Ewald sphere construction, reported in Figure 3.4 can be a convenient representation together with a typical geometry for a LEED experiment.

A conventional LEED setup, reported in Figure 3.4, consists of an electron gun with electron optics, an energy-selector acting ad a high pass filter, a fluorescent screen and a Charge Coupled Device (CCD) camera. The kinetic energy of the electrons emitted by the electron gun is between 20 and 500 eV. Electrons from a low-energy electron gun are diffracted back to the fluorescent screen. The innermost grid is maintained at the same (ground) potential as the sample in order to allow the electrons to travel in a field-free space.

A second grid is set at a retarding potential just sufficient to reject inelastically scattered and secondary electrons but allow the elastically scattered (diffracted) electrons to pass through, where they are then accelerated onto the fluorescent screen. If the periodicity and the orientation of the surface lattice is the same as the underlying bulk lattice, the surface is designed (1×1). A common case is that the vectors of the surface net differ from those of the underlying lattice, so that $a_s = Ma$ and $b_s = Nb$. Vectors a_s and b_s define the surface unit mesh and a and b are the translation vectors of the ideal, unreconstructed surface. The nomenclature for this structure (Wood's notation) is $(M \times N)$. If in addition, the surface lattice is rotated with respect to the underlying lattice by an angle ϕ, the notations become $(M \times N)R\phi$. This notation has been used to identify size and orientation of the silicene and stanene supercells with respect to the Ag(111) surface unit cell.

3.3 Optical characterization techniques

Spectroscopy is a common approach to measure the energy dependent properties of solids [40]. The general scheme for a spectroscopy experiment consists of sending a probe on a sample and observing its modification after the interaction with the sample. The range of energies of interest and the type of interactions to be investigated define the spectroscopic technique. In particular, in infrared and optical spectroscopy the probe consists in light, thus enabling to investigate the response of excitations at momentum $\hbar q \sim 0$, in the energy range from 10^{-3} to 5 eV, thus giving information about the low energy electrodynamics of materials.

3.3.1 NIR-Vis-UV Dispersive Spectrometry

The NIR-Vis-UV (NIR-UV) spectroscopy made it possible to investigate the optical response of Xenes in the spectral region where interband electronic transitions are expected to occur and where the effects of hybridisation with the substrate are most evident (see Chapter 2). Dispersive spectrometers use light sources that generate a broadband of electromagnetic radiation across the UV-NIR spectrum (typically 190 to 3200 nm) to illuminate a sample. A dispersion device, such as a monochromator, separates the broadband radiation into wavelengths. One or more detectors then measure the intensity of the transmitted or reflected radiation by the sample at each wavelength. The transmittance and reflectance measurements discussed in the following chapters were acquired through two different but almost superimposable instruments: an Agilent Cary 5000 and a Jasco V-770 spectrophotometers. They are symmetrical double beam spectrophotometers which can work both in transmission and reflection mode. The light sources are a deuterium arc in the UV (190 to 350 nm) and a

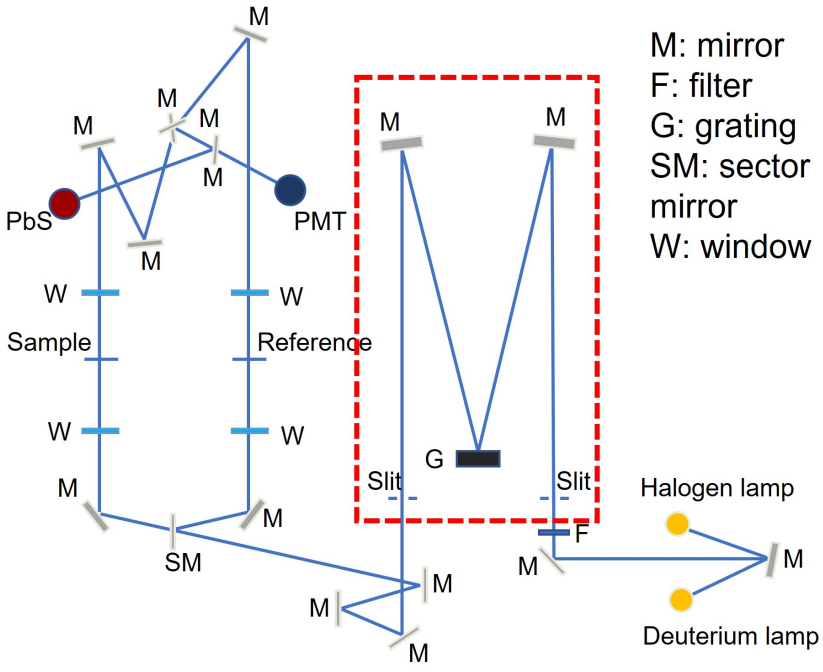

Fig. 3.5 Optical path of Jasco V-770: starting with the light source, the radiation is focused on the entrance slit of the monochromator. Here it is dispersed by the grating and focused on the exit slit. The monochromatic light is split into two beams by a sector mirror: one going to the sample channel and the other to the reference channel. The beams transmitted by the sample and the reference are alternately incident upon the detector. If the reference sample-holder is left empty in the transmittance mode (or it is occupied by an aluminum mirror in reflectance mode), the double beam configuration allows to obtain absolute spectral measurements. The dotted red line highlights the monochromator Czerny-Turner configuration.

tungsten halogen lamp in the VIS-NIR (330 to 3200 nm) spectral regions. The main differences between the two tools concern the monochromator configuration and the detection system. In the Jasco V-770, the monochromator is based on Czerny-Turner configuration and the signal detection takes place via the combination of a photomultiplier tube (PMT) and a PbS photoconductive cell, which cover the VIS-UV and and the NIR region respectively. In the Cary 5000 for the monochromator an out-of-plane double Littrow geometry is used while detection is carried out using a single detector for the whole measurable spectral range. Figure 3.5 shows the optical path of the Jasco V-770 spectrophotometer.

3.3.2 Fourier Transform Infrared Spectroscopy

Fourier transform Infrared (FT-IR) spectroscopy has been used in this work to characterize Xenes in the infrared spectral region, between 0.01 and 1 eV. In this technique the Fourier

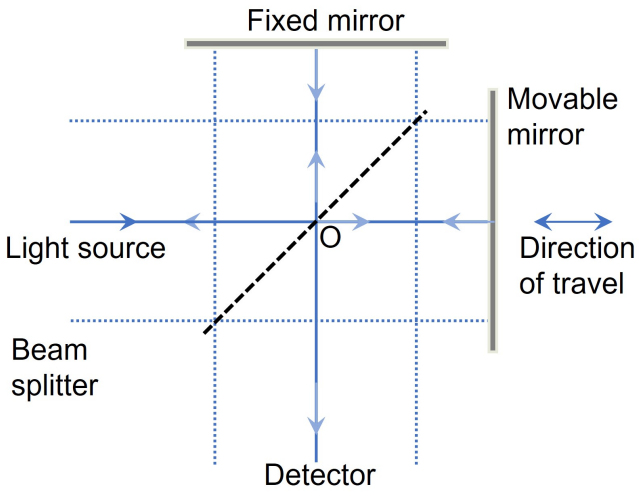

Fig. 3.6 Scheme of Michelson interferometer for collimated beams. Image adapted from Ref.[63].

Transform analysis is applied to convert a spatial dependent interferogram $I(\delta)$, coming from the sample-radiation interaction, into a frequency dependent power spectrum $B(\omega)$. The Michelson configuration is the most common interferometric configuration. It is schematized in Figure 3.6 and consists of a light source, a beamsplitter, two mutually perpendicular plane mirrors and a detector.

The light beam goes from the source to the beamsplitter which splits the beam into two equal beam. One beam is transmitted to a movable mirror at distance $L+\delta/2$ whereas the other beam is reflected to a fixed mirror at distance L. The movable mirror can either be moved back and forth at a constant velocity or be held at equally spaced points for fixed short periods and stepped rapidly between these points. The two methods define the continuous scan interferometer or the step-scan interferometer, respectively. The beams are reflected from the mirrors and then recombined by the beamsplitter. As the path difference is δ, when the beams are combined an interference pattern is created. The interference is constructive if δ is a multiple integer of the wavelengths ($\delta = n\lambda$) and destructive if $\delta = (n+1/2)\lambda$. This interference pattern defines the interferogram and its Fourier transform determines the power spectrum of the source. The detector reads information about every wavelength simultaneously, unlike in dispersive spectrometry (the so-called multiplex or Fellgett's advantage).

The intensity of a collimated beam at the detector, measured as a function of the optical path difference, in an ideal beamsplitter case, is given by:

$$I'(\delta) = 0.5I(\tilde{\nu}_0)[1+cos(2\pi\delta\tilde{\nu}_0)] \tag{3.1}$$

where $I(\tilde{\nu}_0)$ is the intensity of a monochromatic source and $\tilde{\nu}_0$ is the radiation wavenumber which corresponds to $1/\lambda_0$. $I'(\delta)$ consist of a constant component and a modulated component. The modulated component is generally referred to as the interferogram. When the fixed and movable mirrors have the same distance from the beamsplitter (zero-path-difference condition), the beams are in phase and interfere constructively. In this situation, the intensity of the beam passing to the detector is the sum of the intensities of the beams arriving from the fixed and moving mirrors. The amplitude of the interferogram as observed after detection is proportional not only to the intensity of the source but also to the beamsplitter efficiency, the detector response, and the amplifier characteristics. Of these factors, only I_0 varies from one measurement to the next for a given system configuration, while all the other factors remain constant. The Equation 3.1 may be modified introducing a single wavenumber-dependent correction factor $H(\tilde{\nu}_0)$. The modulated component of the signal from the amplifier is:

$$S(\delta) = 0.5H(\tilde{\nu}_0)G(\tilde{\nu}_0)I(\tilde{\nu}_0)cos(2\pi\delta\tilde{\nu}_0) \tag{3.2}$$

where $G(\tilde{\nu}_0)$ is the responsivity of the detector and amplifier for radiation of wavenumber $\tilde{\nu}_0$. At this point it is possible to define the single beam spectral intensity as:

$$B(\tilde{\nu}_0) = 0.5H(\tilde{\nu}_0)G(\tilde{\nu}_0)I(\tilde{\nu}_0) \tag{3.3}$$

So the equation representing the interferogram is therefore:

$$S(\delta) = B(\tilde{\nu}_0)cos(2\pi\delta\tilde{\nu}_0) \tag{3.4}$$

The parameter $B(\tilde{\nu}_0)$ gives the intensity of the source at the wavenumber $\tilde{\nu}_0$, modified by the instrumental characteristics. The spectrum is obtained from the interferogram by computing the cosine Fourier transform of $S(\delta)$. If the source is not monochromatic, the measured interferogram is the resultant of the interferograms corresponding to each wavelength. Examples of spectra and related interferograms are shown in Figure 3.7. For a continous source the interferogram can be represented by the integral:

$$S(\delta) = \int_{-\infty}^{\infty} B(\tilde{\nu})cos(2\pi\tilde{\nu}\delta)\,d\tilde{\nu} \tag{3.5}$$

The inverse Fourier transformation, for $S(\delta)$ even function, will be:

$$B(\nu) = 2\int_{0}^{\infty} S(\delta)cos(2\pi\tilde{\nu}\delta)\,d\delta \tag{3.6}$$

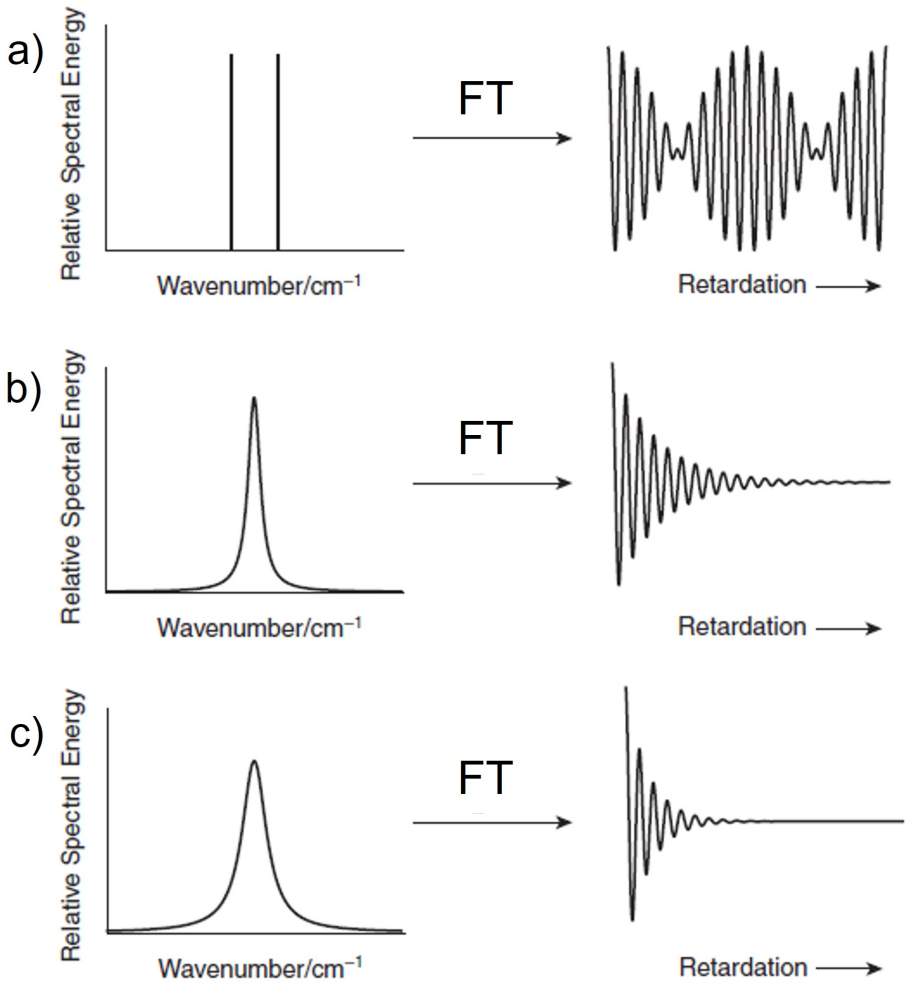

Fig. 3.7 Examples of spectra and their interferograms: a) two infinitesimally narrow lines of equal intensity; b) Lorentzian band centered at the mean of the lines in (a); the frequency of the interferogram is identical to (a) and the envelope decays exponentially; c) Lorentzian band at the same wavenumber as (b) but of twice the width; the exponent of the decay for the interferogram has a value double that of the exponent for (b). Image adapted from Ref.[63].

According to the previous equation, to have a complete spectrum measure at infinitely high resolution, the moving mirror scanning should be an infinitely long distance. The finite resolution of real spectra is the effect of measuring the signal over a limited retardation. This truncation introduces some non-physical contributions to the power spectrum, such as line broadening and spurious oscillations (sidelobes), generally known as spectral leakage. In order to reduce these spurious effects an appropriate truncation function can be introduced (apodization function) which depends on the experiment.

It is important to stress that the spectrometer sampling is discrete. Usually the wavenumber calibration and the interferogram sampling is reported to a single wavelength which in our case is the He-Ne laser frequency. Performing the sampling every time that the laser interference pattern has a minimum allows to sample intensity at equal spaced times. Since the wavelength of the He-Ne laser is $\lambda \approx 633$ nm, the number of points sampled per centimeters is $N = \frac{1cm}{\lambda/2} \approx 31600$. In this case the numerical operation to be performed to get the power spectrum is the Discrete Fourier Transform (DFT).

The discrete sampling of an interferogram is based on the Nyquist criterion, according to which if any waveform that is sinusoidal function of time or distance can be sampled with a sampling frequency or wavenumber greater than or equal to twice the bandpass of the system, there is not loss of information [63]. The power spectrum obtained from DFT shows periodicity in frequency domain and time domain. Due to the frequency periodicity, the spectrum between 0 and N/2 acquired points is the mirror image of the one between N/2 and N while, due to the time infinite periodicity, the spectrum has an infinite number of replicas. These effects, known as aliasing, can bring spurious contributions to the power spectrum. To sample the spectral range between $\tilde{\nu}_{max}$ and $\tilde{\nu}_{min}$ with a resolution of $\Delta\tilde{\nu}$, the required number of sampling points will be:

$$N_s = \frac{2(\tilde{\nu}_{max} - \tilde{\nu}_{min})}{\Delta\tilde{\nu}} \tag{3.7}$$

The last aspect considered in this brief introduction to FTIR spectroscopy is the spectrum phase corrections. In the case of DFT an imaginary component to the power spectrum could emerge due to inhomogeneities of the intensity of light, mechanical instabilities or difficulties in setting the zero path difference. To correct these effects a low-resolution test spectrum can be sampled before measuring to extract the phase, leading to the imaginary component of the spectrum $\phi(\tilde{\nu})$:

$$B(\tilde{\nu}) = R(\tilde{\nu}) + iI(\tilde{\nu}) = B(\tilde{\nu})e^{i\phi(\tilde{\nu})} \tag{3.8}$$

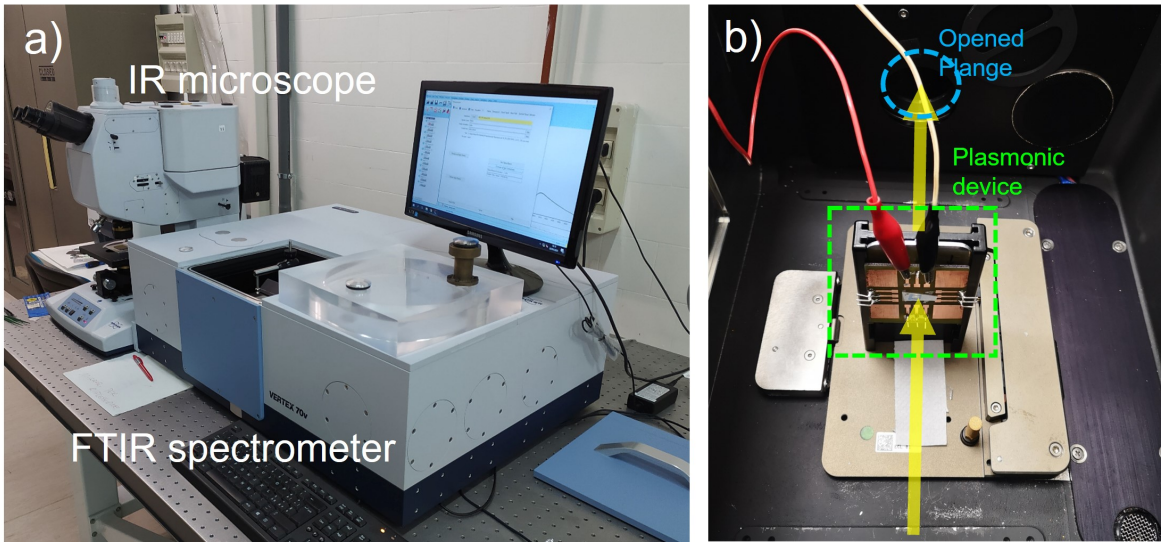

Fig. 3.8 a) Picture of the FT-IR spectroscopy experimental station at Terahertz labora- tories, showing the Bruker VERTEX70v spectrometer and the Hyperion 1000 microscope. b) Bruker VERTEX70v sample compartment. A plasmonic device is mounted inside, ready to be measured in the transmission mode.

where the phase can be calculated as:

$$\phi(\tilde{\nu}) = \arctan \frac{I(\tilde{\nu})}{R(\tilde{\nu})} \tag{3.9}$$

All the IR measurements reported in this work have been performed at Terahertz laboratories of the Physics Department of Sapienza University of Rome. The spectrometer used to characterize the samples in the FIR-MIR spectral region is a Bruker-VERTEX 70v and it is shown in Figure 3.8a, together with the IR microscope. This instrument usually works in vacuum and it allows to perform the measurements in both reflection and transmission mode. The internal light source is a Globar and the transmitted (or reflected) radiation is detected by a DTGS detector. The interferometer can also be coupled to a Bruker Hyperion 1000 infrared microscope which covers the spectral range between 0.05 to 1 eV. The microscope uses a liquid hydrogen-cooled MCT module for detection. Moreover, since the plasmonic properties of microribbon patterned devices depends critically on the light polarization, on these structures the measurements must be performed with linearly polarized light.

Overall, FT-IR spectroscopy and NIR-UV spectrometry are important techniques to investigate the response of materials to the electromagnetic radiation. Indeed, despite their different operating principles, both techniques enable the detection of the same macroscopic optical properties in different spectral ranges. Therefore, their combination makes it possible

to cover an extremely wide spectral interval, ranging from a few meV to ∼7 eV. Here the transmittance and reflectance of several Xene-based samples were measured in order to obtain their optical response. Reflectance and transmittance can be defined as:

$$R(\omega) = \frac{I_r(\omega)}{I_0(\omega)} \tag{3.10}$$

$$T(\omega) = \frac{I_t(\omega)}{I_0(\omega)} \tag{3.11}$$

where $I_r(\omega)$ and $I_t(\omega)$ are the intensities reflected and transmitted by the sample, while $I_0(\omega)$ is the incident intensity. In Figure3.8b is shown the VERTEX 70v sample compartment. Mounted in the sample holder is one of the device designed to measure the transmission of silicon and tin nanosheets as function of the gate voltage. Details of the configurations used for each optical characterisation are given in following chapters. Models and methods used to extract the microscopic properties such as the optical conductivity or the dielectric function of silicene and stanene from $T(\omega)$ and $R(\omega)$ are described in Appendix A.

3.3.3 Raman Spectroscopy

In radiation-matter interaction, the most intense optical processes are related to reflection and absorption. However, a small part of the incident light can be affected by scattering processes [9, 186]. Raman scattering is probably one of the best known and most used in the characterization of 2D materials. In particular, Raman spectroscopy has really proven over the years to be a fast, non-destructive and high-resolution technique and graphene is probably the most striking case in this respect [53]. Raman spectroscopy allows to obtain information about both atomic structure and electronic properties and can be used to determine the effects of perturbations such as electric and magnetic fields, strain, doping or disorder in 2D structures [51]. In this work, the potential of Raman spectroscopy has been fully exploited to shed light on different aspects: from the structural quality of silicene and graphene to the effects of local heating on heterostructures, but also to assess the effectiveness of the ionic-liquid gating as reported at the end of this chapter.

Keeping a classic approach the basic mechanism of Raman scattering is the modulation of the dielectric susceptibility by fluctuations due to a fundamental excitation. Various elementary excitations may be involved in the scattering process, but in solids Raman scattering can be mainly related to the lattice vibrations [186].
In an isotropic medium, the incident radiation induces a polarization:

$$\mathbf{P}(\mathbf{k}_i, \omega_i) = \chi(\mathbf{k}_i, \omega_i)\mathbf{E}(\mathbf{k}_i, \omega_i) \tag{3.12}$$

In the framework of the adiabatic approximation, fluctuations of susceptibility can be expressed as a Taylor series in the atomic displacement $\mathbf{Q}(\mathbf{r},t) = \mathbf{Q}(\mathbf{q},\omega_0)\cos(\mathbf{q}\cdot\mathbf{r}-\omega_0 t)$ associated with a phonon:

$$\chi(\mathbf{k},\omega,\mathbf{q}) = \chi_0(\mathbf{k},\omega) + (\partial\chi\partial\mathbf{Q})_0\mathbf{Q}(\mathbf{r},t) + ... \tag{3.13}$$

where χ_0 is the electric susceptibility of the medium with no fluctuation, the second term represents an oscillating susceptibility induced by the lattice wave, and $\mathbf{q}$ with ω_q are phonon wavevector and frequency, respectively.
So the polarization in presence of atomic vibration becomes (at the first order):

$$\mathbf{P}(\mathbf{r},t,\mathbf{Q}) = \chi_0(\mathbf{k}_i,\omega_i)\mathbf{E}(\mathbf{k}_i,\omega_i) + (\partial\chi/\partial\mathbf{Q})_0\mathbf{Q}(\mathbf{r},t)\mathbf{E}(\mathbf{k}_i,\omega_i) \tag{3.14}$$

The first term $\mathbf{P}_0(\mathbf{r},t)$ represents a polarization vibrating in phase with the incident radiation $\mathbf{E}(\mathbf{k}_i,\omega_i) = \mathbf{E}_i(\mathbf{k}_i,\omega_i)\cos(\mathbf{k}_i\cdot\mathbf{r}-\omega_i t)$ whereas the second term $\mathbf{P}_{ind}(\mathbf{r},t,\mathbf{Q})$ is a polarization wave induced by the phonon.
By making the expression of $\mathbf{P}_{ind}(\mathbf{r},t,\mathbf{Q})$ explicit, two components emerge:

$$\begin{aligned}\mathbf{P}_{ind}(\mathbf{r},t,\mathbf{Q}) = (\partial\chi/\partial\mathbf{Q})_0\mathbf{Q}(\mathbf{q},\omega_0)\cos(\mathbf{q}\cdot\mathbf{r}-\omega_0 t)\times\mathbf{E}_i(\mathbf{k}_i,\omega_i)\cos(\mathbf{k}_i\cdot\mathbf{r}-\omega_i t)\\ = \frac{1}{2}(\partial\chi/\partial\mathbf{Q})_0\mathbf{Q}(\mathbf{q},\omega_0)\mathbf{E}_i(\mathbf{k}_i,\omega_i t)\\ \times\{\cos[(\mathbf{k}_i+\mathbf{q})\cdot\mathbf{r}-(\omega_i+\omega_0)t]\\ +\cos[(\mathbf{k}_i-\mathbf{q})\cdot\mathbf{r}-(\omega_i-\omega_0)t]\}\end{aligned} \tag{3.15}$$

From the above equation, it is easy to recognise a first shifted wave with wavevector $\mathbf{k}_S = (\mathbf{k}_i-\mathbf{q})$ and frequency $\omega_S = (\omega_i-\omega_0)$ and a second one with wavevector $\mathbf{k}_{AS} = (\mathbf{k}_i+\mathbf{q})$ and frequency $\omega_{AS} = (\omega_i+\omega_0)$. They describe the Stokes and Anti-Stokes components of the Raman spectrum, respectively. The Stokes process is the most probable and is the one generally referred to.
Typical Raman experiments are performed in the IR-UV spectral range, between 1.2 and 5.4 eV. For lattice parameters of the order of $\sim 10^{-1}$ nm (~ 0.142 nm in graphene [174] or ~ 0.23 nm in silicene [168]), k_i, $k_S \ll \pi/a$, then $q \ll \pi/a$. It means that in first-order scattering only phonons near Γ ($\mathbf{q}\sim 0$) are measured.
The intensity of scattered radiation is proportional to:

$$I_s \propto |\mathbf{e}_i\cdot(\partial\chi/\partial\mathbf{Q})_0\mathbf{Q}(\omega_0)\cdot\mathbf{e}_s|^2 \tag{3.16}$$

where $\mathbf{e}_i$ and $\mathbf{e}_s$ denote the polarization of incident and scattered radiation. By introducing a unit vector parallel to the phonon displacement $\hat{\mathbf{Q}}$, the Raman tensor can be defined as:

$$\mathbf{R} = (\partial\chi/\partial\mathbf{Q})_0\hat{\mathbf{Q}}(\omega_0) \tag{3.17}$$

The Raman tensor relates the polarization of the scattered to the polarization of the incident radiation and its non-vanishing elements are determined by the symmetry of the crystal. It follows from this that not all the zone center phonons of a crystal are Raman active. Despite the approximation, even with the classical approach, the potential of Raman spectroscopy in determining the properties of crystalline solids such as frequency and symmetry of phonon modes, is evident. Indeed, the symmetry of the Raman tensor depends on the symmetry of the material.

More generally Raman scattering can be described by the time-dependent perturbation theory [9]. Applying quantum mechanics, an inelastic light scattering event involves the destruction of a photon of frequency ω_i incident from a light source, the creation of a scattered photon of frequency ω_s and a creation or destruction of an optical phonon of frequency ω_0. The first two processes arise from the electron-radiation interaction while the last process arises from the electron-phonon interaction. If the excitation is selected to match a specific energy level, then the process is resonant and the intensities are strongly enhanced due to the greater perturbation efficiency. The non-resonant condition is, however, the most common. Electron-hole (e-h) pairs and excitons may be involved in the scattering mechanism as intermediate states.

A basic experimental set-up for Raman spectroscopy consist of a collimated and monochromatic source, an efficient optical system to collect the weak scattered radiation, a spectrometer and a highly sensitive detector. Two different tools for Raman spectroscopy were used to characterize Xenes. The first is a T64000 spectrometer (Horiba Jobin-Yvon) which is triple grating system equipped with a 532 nm solid state laser. The second one is a single monochromator InVia spectrometer (Renishaw) equipped with a 514 nm solid state laser. In both machines, Raman signal detection is performed by a liquid hydrogen-cooled CCD device. Coupling with optical microscopes also allows Raman analysis with micrometric spatial resolution. All spectra are collectred in the backscattering configuration. Moreover, the xyz referenced motorized stages make possible Raman maps to be generated, acquiring spectra from different positions on the sample. By following a specific spectral feature, the distribution of individual chemical components or the variation of other effects such as phase, stress/strain and crystallinity can be reconstructed. An example of this specific use is reported in Chapter 4.

Temperature-dependent Raman Spectroscopy

In harmonic approximation the Raman line shape is a δ-function centered on the optical phonon frequency. Experimentally, however, the Raman line is broadened into a roughly Lorentzian shape with a width that increases with increasing temperature. This width can be attributed to anharmonic terms in the lattice potential energy [9]. In addition to line broadening, anharmonicity causes a shift of the frequency of peak to lower values as the temperature increases. The complex quantity that results from the anharmonic contributions is the phonon self-energy $\Delta(\omega_q, T) + i\Gamma(\omega_q, T)$. It accounts for the renormalization of the phonon energies due to the interaction induced by the anharmonicity [163, 10, 74]. The real part of the self-energy is associated with the frequency shift and is responsible for the temperature dependence of the phonon frequencies while the damping is described by the imaginary part. $\Gamma(\omega_q, T)$ is liable for the broadening of the Raman spectra. If the Raman line shape is fitted by a Lorentzian function, $2\Gamma(\omega_{q\sim 0}, T)$ corresponds to the full width at half maximum of the peak [163]. Other contributions that can be considered are the electron-phonon interaction and the effects of temperature and pressure on phonon modes. While the effects of temperature on mobility can be traced back to the former one, the latter are directly responsible for thermal expansion. The weight that each of these contributions has on the Raman response of a 2D material depends strongly on the intrinsic properties of the system and the possible interaction with the substrate.

Generally, the temperature dependence of the Raman peaks of a supported 2D material is described as the sum of three terms [185]:

$$\Delta\omega(T) = \Delta\omega_A(T) + \Delta\omega_V(T) + \Delta\omega_M(T) \tag{3.18}$$

The first, $\Delta\omega_A(T)$, is the frequency shift due to the anharmonic phonon-phonon processes while the second term $\Delta\omega_V(T)$ describes the lattice thermal expansion. Finally, $\Delta\omega_M(T)$ represents the effect of the mechanical strain caused by the thermal expansion coefficient mismatch between the supported material and the underlying substrate. Conversely, the temperature dependence of the bandwidth of Raman peaks is mainly linked to the anharmonic phonon-phonon interaction [10].

The actual behaviour of the system can be described through approximate expressions that are derived by making assumptions about the processes involved. The model developed by Balkanski [10] is among the most widely used to fit the anharmonic part of the frequency shift. This approach is based on the multi-phonon decay processes stemming from the cubic

or quartic anahrmonicity of the lattice potential. The first term in the Eq. 3.18 will be:

$$\Delta\omega_A(T) = A\big(1+\frac{2}{e^x-1}\big)+B\big(1+\frac{3}{e^y-1}+\frac{3}{(e^y-1)^2}\big) \tag{3.19}$$

where the two coefficient A and B represent the cubic and quartic anharmonic constant. This expression depends on the Bose-Einstein phonon population where $x = \hbar\omega/2k_BT$ and $y = \hbar\omega/3k_BT$, with k_B the Boltzmann constant. A similar expression is also given for the line width.
Studying Raman scattering as a function of temperature thus becomes extremely useful in better understanding all those physical effects that can be attributable to anharmonic phonons, such as thermal expansion, specific heat and thermal conductivity. In contrast to other 2D materials such as graphene [8, 21, 185, 98, 49], black phosphorous [171, 163, 47] and TMDs [137, 191], there is a lack of works reporting experimental studies on the thermal response of epitaxial Xenes, mainly due to configurational issues. The greatest limitation is probably is the strong interaction between the films and the native substrate. Being able to derive partial information or effective quantities determined by the interaction of Xenes with the materials they are supported by is certainly an important step towards the development of devices based on specific configurations.
It is worth noting at this point that the same laser used for the scattering spectroscopy can be used as a source of local heating and can affect the phonon response of the measured sample. This is the concept behind the optothermal Raman spectroscopy, used in Chapter 5 to gain information on the thermal behaviour of silicene on silver and the same silicene, placed within a heterostructure.

3.4 Plasmonic devices fabrication

Periodic surface patterning is a widely used method to experimentally observe the plasmonic response from different systems [79, 37, 6, 41]. The simplest periodicity can be achieved by making parallel stripes. Despite the elementary geometry, these structures are very efficient in spatially localising the collective electron modes. In order to investigate the plasmonic response in Xenes on Al_2O_3(0001) samples, micrometric stripes were realized by performing optical lithography on silicon nanosheets on Al_2O_3(0001) and tin nanosheets on graphene-Al_2O_3(0001). The patterning process is accurately described below.

3.4.1 Optical Lithography

Conventionally, optical lithography or photo-lithography consists of transferring patterns to a material from master images [126]. During the process, the photo-resist is applied and subsequently exposed to UV light through a mask. Chemical changes occur in the exposed regions making the photoresist more soluble (positive) or less soluble (negative resist) in a given solvent. According to the type of resist, a selected part of it is removed leaving on the surface a photo-resist pattern. The quality of the resulting profile depends on the combination of several parameters such as photoresist properties, exposure and development conditions. The next two steps consist in transferring the pattern from the resist to the sample by means of an etching process of the unprotected part of the sample and removing the resist. The wavelength of the photon source determines the maximum resolution of the process that can be estimate as follows:

$$R = (d \cdot \lambda)^{1/2}$$

where d is the resist thickness and λ is the wavelength of the optical radiation. In our case, considering the typical thickness of the photoresistive material and the wavelength equal to 435 nm, the minimum feature size that can be printed is $R = 0.7\mu m$, well below the dimensions of interest for stripes. Stripes fabrication, on epitaxial silicon and tin on graphene supported by $Al_2O_3(0001)$, was performed in a class 1000 clean room at CNR-IMM of Agrate Brianza. The clean room is equipped with several systems for film deposition, electronic and optical lithography, etching processes and diagnostics. To study the optical/plasmonic response of Xenes a specific mask, made by stripes with different widths and periodicity, was designed. The whole process is shown in Figure 3.9. It can be summarised in the following steps:

- Cleaning: the sample is initially heated at 120°C for a few minutes in order to drive off any moisture that may be present on the surface;
- Coating: the sample is covered with photoresist by spin coating. The resist is spread over the sample surface and it is spun at high speed to produce a uniformly thick layer. Setting a rotation speed of 6000 rpm for 30 s produces a layer of about 1 μm thick;
- Baking: the photoresist-coated sample is pre-backed at 90 °for 60 s on an hotplate, to drive off the excess of photoresist solvent.
- Exposure: in this step the desired pattern is written on the resist. A specially designed mask was used to obtain the stripes by placing it in contact with the resist before exposure. When exposed, positive photoresist becomes soluble in the developer.

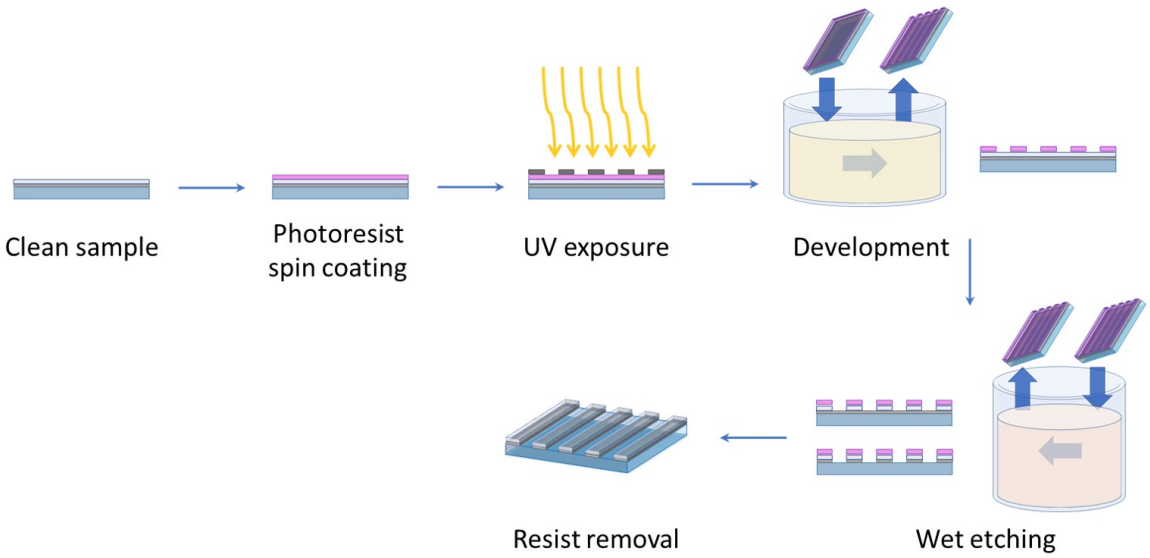

Fig. 3.9 Patterning process steps.

- Development: as a result of the exposure, the photosensitive material experiences a change in its physical and chemical properties, varying its solubility with respect to a specific solvent. For stripe widths between 3 and 5 μm, the optimum development time was estimated to be 40-45 seconds.
- Hard-baking: the sample is heated to 120 °for a few minutes in order to make the photoresist structure more stable for subsequent steps;
- Wet-etching: an etchant solution such as and acid is used in order to chemically attack the underlying film while leaving the photoresist intact. This form of etching is selective and isotropic. In particular the etching solutions were chosen according to the sequence of the layers that form the sample.
- Resist removal: the not exposed resist, which was not removed in the development step is removed by acetone, leaving the desired patterned material on the substrate.

As just mentioned, the selectivity of the etching process requires choosing specific chemicals depending on the material to be removed. The 5 nm of capping layer were removed exposing all the samples to a buffered oxide etch (BOE) (50:1) for about 5 s. For the silicon films, KOH (20%) was used with exposure times dependent on the films thickness. For tin films, tests were carried out with aqua regia, which proved to be very aggressive for such thin films and therefore difficult to handle. Further optimisation tests showed how the strong oxygen reactivity of tin can be exploited during etching. The opening of the alumina channels

facilitates tin oxidation, which can be easily removed by exposing the sample back to the BOE. Finally, to remove graphene, O_2 plasma etching (5 min at 80 W) was performed. This type of process is a mix of chemical etching due reaction of the film with the plasma and physical sputtering due to the directional bombardment of the ions hitting the substrate.

It is worth noting that the electron beam lithography (EBL), also present in the CNR-IMM unit laboratory, was not used because of the insulating nature of the supporting substrate ($Al_2O_3(0001)$). EBL is a fabrication technique based on the controlled irradiation of the sample covered with a sensitive resist via a focused beam of electrons. Typically a scanning electron microscope (SEM) is integrated with a lithographic system for the control of the electron beam and/or the SEM stage. This technique allows to obtain features with nanometric definition in very small areas with a low defect densities.

To make metal contacts on silicon and tin films, the lithographic process has been repeated using a mask-less system. In maskless photolithography a CAD-drawing pattern is exposed directly onto the substrate surface with the help of a spatial light modulator. This direct-write process facilitated alignments on previously made patterns, optimising the space available on the sample surface. A $1 \times 3\ mm^2$ electrode was created perpendicular to the stripes direction by opening the capping layer and evaporating Cr (10 nm) and Au (50 nm). Finally, the resist was removed with an acetone bath.

3.4.2 Ionic Liquid Gating

Modifying the physical properties of condensed matter systems by controlling the charge carrier density is a crucial aspect of device optimization both for electronic and photonic devices. In this sense, the invention of the field-effect transistor (FET) is a milestone in the technological revolution that began exactly 75 years ago [11]. The working principle of FET devices is based on the modulation of the transport properties of a material by means of an applied electric field [136]. The conventional approach involves the use of a solid-state dielectric layer between the active material and the gate electrode, which is both electronically and ionically insulating. The electrostatic doping scheme allows tuning the charge density excluding side effects such as disorder introduction or lattice structure modification that are typical of chemical substitutions and pressure application. On the other and, in order to inject a significant amount of charge, intense electric fields are required. This is probably the most limiting issue concerning the solid-state dielectric gate. The electrochemical gate (with liquid, gel or solid electrolytes) is an alternative approach, where the dielectric is replaced by a ionic compound.

In this work, an ionic liquid (IL) gate was developed with the aim of modifying the Xenes carrier density and evaluating effects on their optical and plasmonic response. Ionic liquids (IL) are ionic compounds, typically molten salts, formed by organic cations and inorganic anions. In contrast to conventional salts they are liquid at wide range of temperatures and differ from ionic solutions in the absence of a solvent [192].Among the main properties are chemical stability, non-volatility, non-flammability, low vapor pressure, relatively small electronic conductivity and comparatively large ionic conductivity. The application of an electric potential between the gate electrode and the active material, in contact with the IL, leads to a migration of cation and anion towards the oppositely charged electrodes. The IL-gate operation diagram is shown in Figure 3.10 together with a picture of an experimental prototype. In contrast to bulk dielectrics, IL are polarized only across a thin ($\sim 1nm$) interfa-

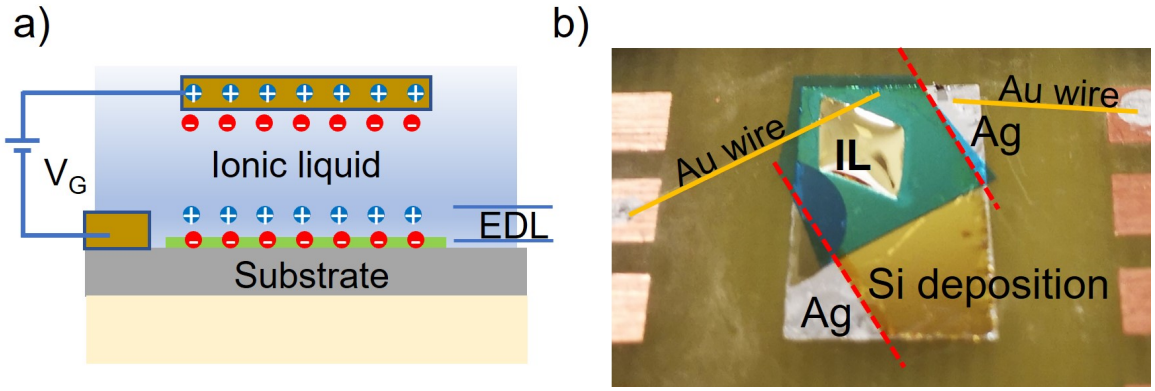

Fig. 3.10 a) Lateral view of an IL-gated device: when V_{Gate} is applied, ions are accumulated at the interface with the 2D film and a charge with opposite sign is induced on its surface, forming the electric double layer. b) Picture of a device for ionic liquid gating. A portion of the epitaxial film is covered by the [EMIM][TFSI]. It is polarized by a voltage source.

cial layer [164]. The formed electric double layer at the IL/material interface can be seen as a capacitor capable of accumulating an high density of charges in the channel. Large interfacial capacitance in the range of $\sim 1-10\mu F$ and extreme charge carrier densities ($\sim 10^{14} cm^{-2}$) make the electrochemical gate more efficient than the dielectric gate for 2D materials, since all of the applied voltage results a chemical potential shift. The typical operating voltages are in units of volts instead of tens of volts, characteristic for dielectric gates [33, 93]. The high levels of charge injection makes the electrochemical gate a widely used method in many areas of fundamental research on 2D materials. Electronic transport measurements and phase transitions experiments are just few examples. The first graphene top gating using a polymer electrolyte is reported by Das and co-workers in Ref. [33]. They showed a doping levels of up to $5 \times 10^{13} cm^{-2}$. Comparing this value with the value obtained through back-gate

configurations, they showed a value much higher than those reported until then. Through the electrochemical gate, a huge charge injection was obtained also for noble metal thin films. Despite the difficulty of carrying out field-effect measurements on metals, due to short electronic screening length of these materials, charge densities up to $4.5 \times 10^{15} cm^{-2}$ by using a polymer-electrolyte solution is reported [162]. In one of the examples shown in Section 2.3.3, where the plasmonic response of graphene is studied in the IR and THz frequencies, an ionic liquid was also used to control the carrier concentration in graphene micro-ribbon arrays [79]. It should be emphasised that in this particular case, the starting ionic liquid has been manipulated in order to obtain an ion-gel [30].

1-Ethyl-3-methylimidazolium bis(trifluoromethylsulfonyl)imide, also known as EMIM-TFSI, is the IL chosen as gate dielectric in the experiments reported in this work. The molecular structure of EMIM-TFSI has shown in Figure 3.11. It is polar binary salt composed of nitrogen-containing cations and imide anions. Given the chemical structure of the IL, an electrochemical stability window (ESW) can be defined. Within the ESW range, the electrode is perfectly polarizable and no appreciable current flows. For EMIM-TFSI at room temperature, the ESW is 4.19 V: from -2.07 to 2.12 V [192].

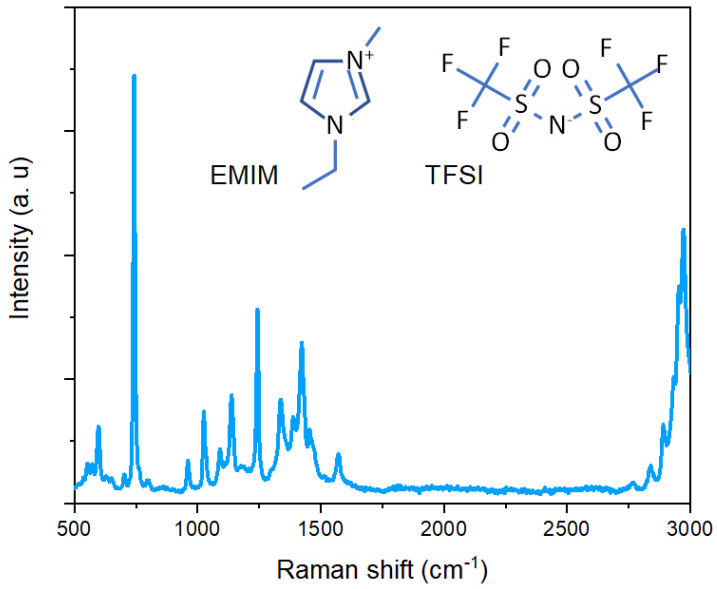

Fig. 3.11 Raman spectrum of [EMIM][TFSI] from 500 to 3000 cm^{-1}.

In order to use the EMIM-TFSI as gate dielectric it was previously characterized by Raman (and Infrared spectroscopy). The Raman spectrum acquired from 500 to 3000 cm^{-1} is reported in Figure 3.11 and is in good agreement with previous characterizations [84]. The

strongest bands in the Raman spectrum can be assigned to the CH stretching vibrations of the [EMIM] ethyl chain ($\sim 2960\ cm^{-1}$), the ring H-C-C-H symmetric bending combined with CF_3 symmetric bending (at $760\ cm^{-1}$), and the ring H-C-C-H in plane anti-symmetric stretching ($\sim 1431\ cm^{-1}$). Other recognisable vibrations from the [TFSI] anion are a SO_2 antisymmetric bending at $608\ cm^{-1}$, a SO_2 symmetric stretching around $1145\ cm^{-1}$, and a SO_2 antisymmetric stretching with contributions from the CF_3 symmetric stretching at $1252\ cm^{-1}$.

Chapter 4

Xenes on Al_2O_3 (0001)

Several sections in Chapters 1 and 2 highlight the crucial role of the substrate in the experimental realization of Xenes by epitaxy. The substrate must be chosen carefully, taking into account the requirement of commensurability. However, in many cases, this necessary condition is not sufficient to preserve the original electronic characters of the Xenes, as for silicene on Ag(111) [168, 31]. Theoretical calculations suggested the use of insulating substrates as a possible solution to this problem. It has been predicted that silicene and stanene can grow with limited interactions with on Al_2O_3(0001) [27, 169] and the results reported on the experimental realization of silicene-like nanosheets are particularly encouraging in this respect [61]. In this chapter, the possibility of extending the methodology proposed for silicene-like thin films grown on Al_2O_3(0001) to stanene is explored, with the aim of accessing its optical properties related to the non-trivial topology.

Al_2O_3(0001) is a dielectric material with an experimental band gap of ~ 9 eV [55]. It is optically transparent over a wide spectral range, from infrared to ultraviolet frequencies, and is therefore suitable for accessing the optical properties of thin films grown on its surface. A further substrate engineering strategy had to be developed despite the promising results reported in the first part of this chapter. This is due to oxidation effects of the Al_2O_3(0001) substrate on the tin nanosheets. The solution considered and reported in the second part of this chapter concerns the insertion of graphene as a buffer layer.

It is important to stress that the use of Al_2O_3(0001) substrates is particularly advantageous. Its insulating nature limits the interaction between integrated circuit components, reducing leakage current, parasitic capacitance and power consumption. In electronics and photonics, therefore, it can have a wide range of applications [78, 7, 28].

4.1 Tin nanosheets

Stanene attracted and continues to attract great interest because of its optical behaviour, which results from non-trivial topological properties of its band structure (see Sec. 2.1). The atomic weight of tin is greater than that of the preceding elements in the same group in the periodic table. This makes the effect of spin-orbit coupling (SOC) more relevant: it converts stanene from an ideal semi-metal to a quantum spin Hall insulator. Despite the keen appeal, the experimental realisation of stanene is limited by significant obstacles that strongly depend on the chemical reactivity of its constituent element. After the encouraging results obtained with the synthesis of silicon nano-sheets on Al_2O_3(0001) [61], the focus shifted to the study of the properties of thin tin films on the same optically transparent substrate. The choice of sapphire as a substrate was also supported by theoretical results in the literature that consider Al_2O_3(0001) as capable of preserving structural and electronic properties of stanene. DFT calculations and tight binding simulations performed by Wang and collaborators [169] suggest that stanene on Al_2O_3(0001) can be atomically bound but electronically decoupled from the substrate, providing high structural stability. This theoretical work also supports the presence of a significant topologically non-trivial band gap of 0.25 eV.

In this section, with the aim of synthesising the stanene, the optical properties of epitaxially grown tin nanosheets on Al_2O_3(0001) have been investigated in a broad photon energy range.

4.1.1 Experimental methods

Tin growth onto Al_2O_3(0001) was performed by molecular beam epitaxy (MBE) using a k-cell evaporator after the calibration of flux rate through a quartz microbalance. One-side polished Al_2O_3(0001) substrates were degassed in ultra-high vacuum at $\sim$ 250 °C , for several hours before tin deposition. Three different samples were grown at variable temperature ranging from $\sim$ 25 °C (Room Temperature) to 570 °C. The nominal thickness considered, based on the previous quartz microbalance calibration, is 0.5 nm. In order to assess the effect of thickness on the optical response of the films, a further sample with a thickness of 1.5 nm was grown at room temperature. For the sake of clarity, the full list of samples analysed is given in Table 4.1.Tin films were subsequently protected using an *in situ* grown capping layer made of amorphous aluminum oxide ($\sim$ 5 nm) as for other Xenes [116]. Before and after the tin and a-Al_2O_3 depositions, the chemical status was monitored by means of *in-situ* X-ray photoelectron spectroscopy (XPS). A more accurate description of the XPS system can be found in Section 3.2. The absolute transmittance and reflectance were measured at RT from 0.01 - 6.5 eV. Combining the two configurations (T and R) allowed us to cover a wide

spectral range, between far-infrared (FIR) and ultraviolet (UV), avoiding the exclusion of the Al_2O_3 active-phonon region ($0.034-0.12$ eV) from the analysis. The microscopic optical properties of the tin films were then extracted from a Kramers-Kronig consistent multi-layer model [86].

Table 4.1 List of samples analyzed. Thickness and growth temperature are shown.

n	Thickness (nm)	Growth temperature (°C)
1	0.5	~ 25
2	0.5	470
3	0.5	570
4	1.5	~ 25

4.1.2 Results and discussion

In situ analysis

A sketch of the samples structure is reported in Figure 4.1a. The chemical interaction between tin and $Al_2O_3(0001)$ was evaluated by an $in-situ$ XPS analysis. During the investigation, the C 1s core level was used as a reference for substrate-induced charging effects. Together with the C 1s, Al 2p, O 1s and Sn 3d core levels were also evaluated, but only Sn $3d_{5/2}$ has been considered below. Figure 4.1b reports the representative XPS spectra of the sample grown at room temperature just after the 0.5 nm of tin deposition and before the a-Al_2O_3 encapsulation. XPS Sn $3d_{5/2}$ core level shows two components: Sn^0 narrower at $BE = 484.93$ eV with a full-width at half-maximum $(FWHM) = 1.18$ eV and Sn^{x+} broader at $BE = 486.4$ eV, with $FWHM = 2$ eV. For the same tin nominal thickness, i. e. 0.5 nm and regardless of substrate temperature, all the samples scrutinized showed two components of the Sn $3d_{5/2}$ core level. The one at highest BE can be related to an oxidation state[157, 158]. The difference in BE between the metallic and the oxidized component is about 1.5 eV in all the 0.5 nm-thick samples, whereas the ratio between the metal and oxide component shows a temperature dependence as reported in Figure 4.1c. When increasing the growth temperature (T_G) from RT to 570 °C , the FWHM of the two tin components (Sn^0 and Sn^{x+}) are as those of 4.1b (1.2 and 2 eV, respectively) but the ratio between the metallic and oxide components Sn^0/Sn^{x+} decrease, from 4.99 (as measured when T_G=RT) down to 0.69. Further experiments are needed to determine the exact stoichiometry of the formed oxide, but from a comparison with published data, some observations can still be made as follows. Usually the BE of the elemental component Sn^0 is placed at ~ 484.98 eV while the oxidation states of SnO and

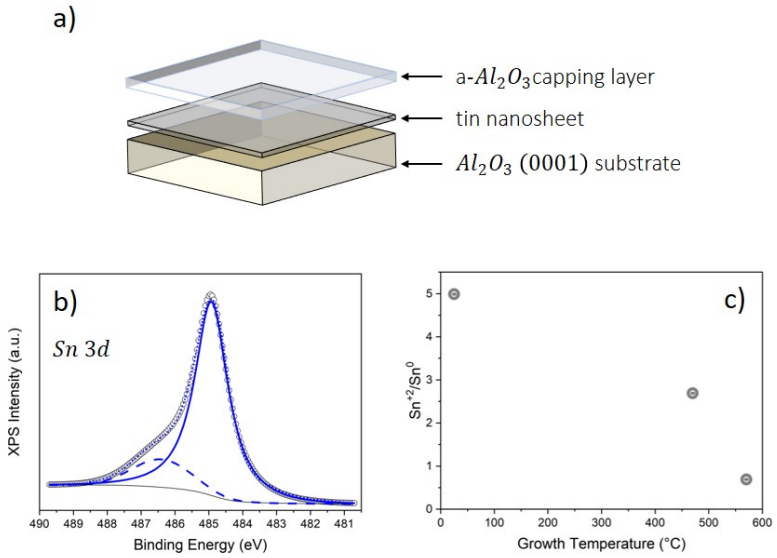

Fig. 4.1 a) Sketch of the samples from top to bottom: amorphous Al_2O_3 capping layer, tin nanosheets grown by MBE at RT, 470 and 570 °C, Al_2O_3(0001) substrate. b) XPS $Sn3d_{5/2}$ core level of 0.5 nm tin grown at RT showing Sn^0 (continuous line) and Sn^{x+} (dashed line) components related to the elemental and oxidized states of tin. Open circles represent experimental data. c) The Sn^0/Sn^{x+} ratio of the three samples grown at different substrate temperature (RT, 470 and 570 °C). The XPS spectra are recorded before the encapsulation.

SnO_2 are at 486.16 and 486.79 eV, respectively [157, 158]. Moreover, Sn $3d_{5/2}$ core level was observed at $BE = 486.2$ eV with a SnO stoichiometry on $Al_2O_3(\bar{1}012)$ [135]. The BE shift can thus be linked, for all samples considered, with an intermediate oxidation state between SnO and SnO_2. It is also worth noting that other metals oxidise at room temperature when grown on Al_2O_3(0001) substrates [125, 15]. The origin of the reported oxidation can be likely related to the interaction between tin and oxygen atoms of the Al_2O_3(0001), even if the surface is Al-terminated [43]. Specifically it can be explained by the interaction between tin and the adsorbed hydroxyl group (-OH) on the surface of the Al_2O_3(0001) substrate [2, 125].

Optical characterization

In order to investigate the optical response of tin films, at the two-dimensional limit, the absolute reflectance $R(\omega)$ and transmittance $T(\omega)$ were acquired from FIR to UV photon energy range (0.01-6.45 eV). The spectra, for different intervals, are reported in Figure 4.2. In particular, transmittance measurements have been performed in the substrate transparency region, i.e. below 0.035 eV and above 0.12 eV, while reflectance measurements have been collected in the range from 0.035 to 0.12 eV. In this region Al_2O_3(0001) shows a strong phonon absorption [2] that does not permit transmittance measurements. Figure 4.2a-b show

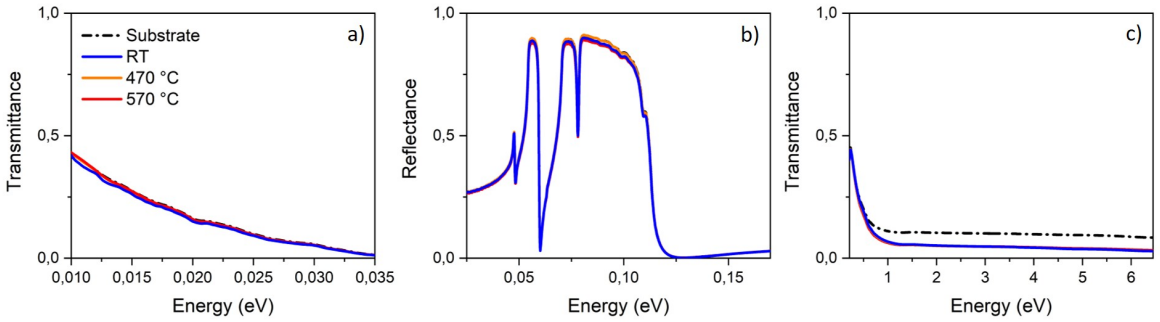

Fig. 4.2 Macroscopic optical properties of Bare $Al_2O_3(0001)$ substrate (black dashed line) and tin nanosheets grown at RT (blue line), 470 °C (orange line), and 570 °C (red line): a) Transmittance in the FIR spectral region. b) Reflectance in the MIR spectral region. c) Transmittance in the MIR-UV spectral region.

that in the interval between 0.01 and 0.035 eV, no optical signatures of the tin nanosheets can be observed. The absence of absorption in this region suggests the presence of an optical gap fairly compatible with the theoretical prediction for stanene [169]. Indeed, a gap as large as 0.25 eV opens after SOC is turned on in *ab initio* calculations, which as mentioned, is indicative of the non-trivial topological feature of stanene on $Al_2O_3(0001)$. Conversely, in the MIR-Vis-UV photon energy range (0.17-6.45 eV) tin nanosheets show an optical response different from that of the substrate, as shown in Figure 4.2c. The transmittance for all the samples is lower than that of the reference substrate. Absorption coefficients of the 0.5 nm-thick films deposited at increasing temperature (from RT to 570 °C) are reported in Figure 4.3. $\alpha(\omega)$ is obtained via the imaginary part of the refractive index as $\alpha(\omega) = 2\omega k(\omega)/c$, where $k(\omega)$, known also as extinction coefficient, is the imaginary part of the complex refractive index $\tilde{n}(\omega)$ and c is the speed of light. The extinction coefficient, in turn, has been extracted from a multilayer Drude-Lorentz model by considering both the measured $T(\omega)$ and $R(\omega)$. The absorption coefficient of tin films has been obtained by taking into account the actual complex refractive index of $Al_2O_3(0001)$, determined from the absolute transmittance and reflectance of a bare substrate coming from the same batch. It is important to stress that the amorphous capping layer, due to its small thickness and intrinsic transparency, does not affect the optical response of tin nanosheets on $Al_2O_3(0001)$. Further details of optical analysis methods are given in the Appendix A.

Despite differences in the ratio of metallic to oxidised component (Figure 4.1), the optical response in Figure 4.3 shows only a weak dependence on growth temperature of the samples. Indeed, their absorption coefficients show a quite similar shape characterized by two broad bands centered at nearly ~ 1.25 and ~ 3 eV. In the same plot (right scale),

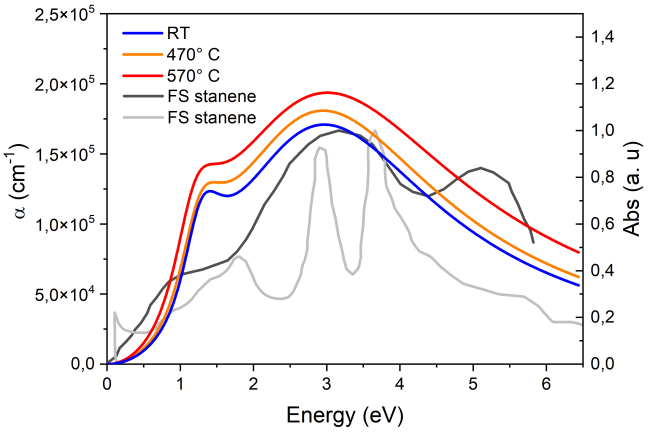

Fig. 4.3 Absorption coefficients $\alpha(\omega)$ of 0.5 nm-thick samples grown at RT (blue), 470 °C (orange), and 570 °C (red). The theoretical normalized absorbance $A(\omega)$ of freestanding stanene (black and gray lines) is reported for comparison (data from Refs. [111, 76])

.

theoretical absorption spectra for freestanding stanene are reported for comparison. As already mentioned in Chapter 2, the absorbance spectrum calculated by Matthes *et al* [111] shows a first peak around 1.8 eV as a consequence of 2D saddle points in the $\pi - \pi^*$ interband structure of stanene, located at the six M points at the Brillouin zone boundary. The higher-energy peaks near 3.1 and 4.0 eV are instead related to $\sigma - \sigma^*$ transitions mainly at the Γ point of the Brillouin zone [110, 111]. Here the experimental absorption feature of tin nanosheets at nearly 1.25 eV is redshifted with respect to the theoretical one (at about 1.8 eV) of freestanding stanene, while the theoretical two-peak structure (at 3.1 and 4 eV) merge in a single broad feature (located around 3 eV) in the experimental data. These effects are probably due to interaction with Al_2O_3(0001) substrate, as has already been observed for silicon nano-sheets grown on the same substrate [61]. The experimental absorption coefficients in the FIR spectral region show a vanishing intensity towards low energies ($\alpha(\omega) \to 0$), without a sharp absorption edge as expected from theoretical calculations [111]. However, it is important to observe that the reported calculation has been performed at zero temperature and the expected gap, at finite temperature, should be smoothed. Figure 4.3 reports a second theoretical freestanding stanene absorption spectrum, calculated by John et al. [76] for parallel (to the basal plane) polarized incident light. Their calculated absorbance $A(\omega)$ (black dashed line) shows an even better agreement with the experimental data obtained with an unpolarised light source. In particular, the broad theoretical peak centered at 3.27 eV, due to transitions among parallel bands formed along the K-Γ direction by p_z and σ^* orbitals, can be easily compared with the experimental broad feature centered at ~ 3 eV.

Conversely, the peak at 5.21 eV, related to the electronic transitions from p_x hybridized orbital and π^*, is not observed, being probably hidden by the high-energy experimental absorption tail. Finally, absorption starts at 1.27 eV with a small hump and not a sharp peak. For stanene bands do not become as flat as the other Xenes (graphene, silicene, and germanene) and hence the van Hove singularity related to $\pi - \pi^*$ interband transition is broadened. This is in good agreement with the experimental feature placed at 1.25 eV. Therefore, comparing experimental data and theoretical calculations, when scaled down to 2D regime, tin nanosheets on $Al_2O_3(0001)$ reveal stanene-like properties.

Further comparisons of the optical response of tin nanosheets with the absorption spectra of elemental allotropes of tin and various tin oxides corroborate the findings just presented. In Figure 4.4a the absorption coefficients of the 0.5 nm-thick tin nanosheets grown at different temperatures are contrasted with those of SnO and SnO_2 [132, 149]. Although the spectral

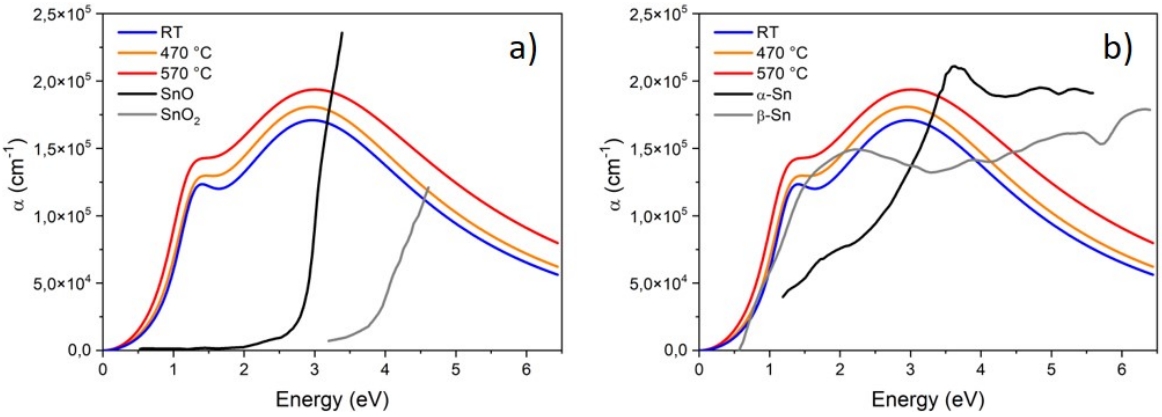

Fig. 4.4 a) Comparison between the absorption coefficients of Figure 4.3 and those of SnO (black) and SnO_2 (gray) (data from Refs [132, 149]). b) Comparison between the absorption coefficients of Figure 4.3 and those of α-Sn (black) and β-Sn (gray) (data from Refs [166, 160].

range examined does not coincide perfectly with the data available for the two oxide forms, different behaviour can be clearly observed. Both SnO and SnO_2 are electric insulators and have an optical gap at ~ 3 eV and ~ 4 eV, respectively. On the contrary, the optical absorption for all three tin nanosheets starts at lower energies. It might therefore make sense to consider the optical contribution of tin oxides to the observed spectra only for photon energies of more than 3 eV, ruling out an oxide-related response at frequencies below this threshold. On the other hand, a similar comparative analysis is reported in Figure 4.4b, by taking the absorption coefficient of the α- and β-Sn phases into account [166, 160]. This comparison highlights that the tin nanosheets does not resemble neither with the zero-gap semiconductor and the metal form nor with a linear combination of both. Thus the comparisons of all

spectra shown in Figure 4.4 further suggest that tin nanosheets on $Al_2O_3(0001)$, grown at the two-dimensional limit, show stanene-like properties.

Recent findings on superconductivity in a few-layer stanene system [45] and topological states in α-Sn thin films grown on InSb(111) [12, 180] also make the study of the optical response of tin nanosheets with increasing thickness particularly interesting. The comparison between the real part of the optical conductivity, $\sigma_1(\omega)$, of 0.5 and 1.5 nm-thick samples grown at RT is reported in Figure 4.5a.

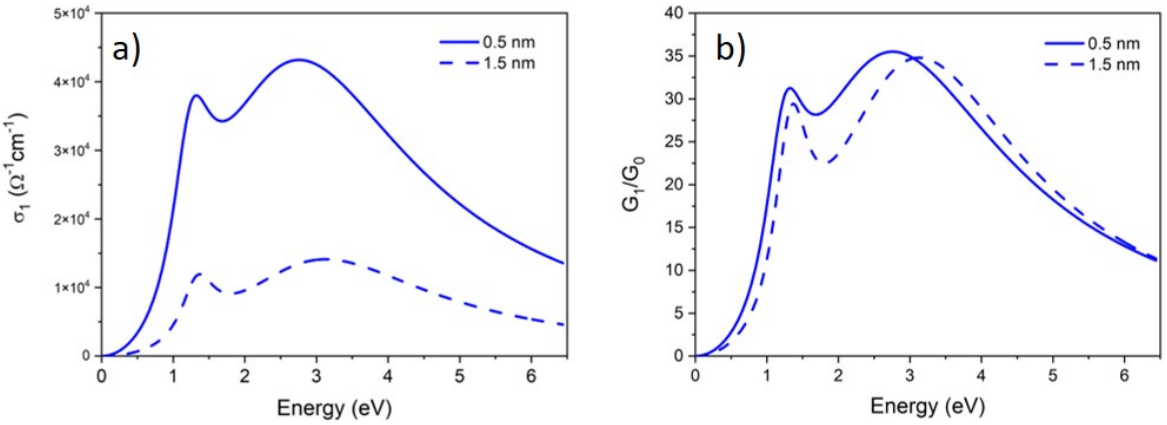

Fig. 4.5 a) Real part of the optical conductivity of 0.5 (blue) and 1.5 nm (blue dashed) tin nanosheets. b) Real part of the normalized optical conductance of 0.5 (blue) and 1.5 (blue dashed) nm-thick tin nanosheets grown at RT.

This quantity can be calculated as $\sigma_1 = \alpha$n c/4π, where α and n are the absorption coefficient and the refractive index of the tin films, both frequency-dependent. The introduction of a parameter, such as the film thickness, could suggest a dimensional crossover as already observed for silicon nanosheets [61]. However, in this case, no difference was observed as thickness increased. Specifically, moving from a nanosheet thickness of 0.5 to 1 nm, the σ_1 intensity shows an inverse dependence versus the film thickness. Despite this, the optical conductivity of the 1.5 nm thick nanosheet shows the same stanene-like features as the thinner sample, e. i. the broad peaks at 1.25 and 3 eV. A further comparison can be made in terms of normalized optical conductance G_1/G_0 which is related to the optical conductivity through $G_1 = \sigma_1 d$, where d is the film thickness. $G_0 = e^2/4\hbar$ [87] is instead the universal conductance, experimentally measured in graphene and confirmed by theoretical calculations [113, 107]. This quantity is conventionally used to describe the optical properties of 2D layered materials [107] and topological insulators[1]. Figure 4.5b shows that the low-energy spectral features of 0.5 and 1.5 nm G_1/G_0 spectra nearly superimpose but the broad band at higher energy is lightly blueshifted for the 1.5 nm nanosheet. The dimensional renormalisation allowed the optical response of tin nanosheets to be reveled,

independently of thickness d, showing that the stanene-like fingerprints are almost conserved. This suggests the existence of a single active stanene-like layer in both samples which, in the thickest sample, is likely superimposed to an optically inert layer.

The optical behavior of the tin films at the 2D limit is very similar to each other and strongly differs from those of common tin oxide (SnO and SnO_2) and from those of conventional elemental tin phases (α- and β-Sn). Most importantly, absorption spectra show characteristic signatures that closely resemble those of freestanding stanene endowed with SOC-induced bandgap as well as absorption peaks due electronic interband transitions along high symmetry directions of the Brillouin zone. The non-trivial nature of 2D tin nanosheets on $Al_2O_3(0001)$ is further corroborated by an interesting thickness-dependent optical response characterized by a decrease of the optical conductivity intensity for thicker films. However, when dimensional renormalization is taken into account through optical conductance comparison, the optical behavior turns out to be almost identical to the stanene-like spectrum of the thinnest nanosheet.

4.2 Graphene as buffer layer

As highlighted in the previous section, the optical response of tin nanosheets grown on $Al_2O_3(0001)$ show stanene-like features when compared to calculated absorbance spectra [111, 76]. Conversely, the XPS analysis show signs of tin oxidation well before the capping layer deposition. This oxidation process can therefore be explained by the interaction between tin and the adsorbed hydroxyl group (-OH) on the surface of the $Al_2O_3(0001)$ substrate [2, 125].

It is a matter of fact that the substrate plays a key role in determining structural and electronic properties of 2D materials. Gaining control over the interaction between the material of interest and the supporting substrate is all the more crucial, given the intrinsic metastable nature of Xenes. Nevertheless, from a general perspective, the stacking of different 2D materials offers a great potential for tailoring the properties of each constituent. The addition of graphene as a buffer layer, reported in the following paragraphs, fits into this context. On the one hand, there is a strong need to decouple stanene from the $Al_2O_3(0001)$ substrate in order to experimentally observe its promising properties. On the other hand, there is a growing interest in the discovery of new physics obtained by combining original heterostructures [129]. In this respect, at strongly interacting interfaces, new phenomena may emerge from common effects such as charge transfer or induced strain [155]. To all this must be added the advances made in the commercialization of graphene. Nowadays, the use of graphene in electronics, optoelectronics and photonics is severely limited by the

production methods and by the quality of the material obtained. Graphene on Al_2O_3(0001) is a technologically relevant system that attracted great interest in recent years [114, 29, 92]. It has been shown that metallic contamination levels, unintentional doping or mechanical stress can be reduced by employing sapphire as target substrate. Indeed, the tri-coordinated Al sites on the surface can act as catalytic sites during growth processes making Al_2O_3(0001) substrates a metal-free alternative. Moreover, it can itself serve as a substrate for a device fabricated directly on the synthesised 2D material, without the need for a transfer process [83]. There are examples in the literature where the atomically planar surface of graphene has been used as a template for the stabilisation of the growth of different 2D materials [68, 138]. Despite this, few works show the direct synthesis of Xenes on graphene to obtain vertical hetero-stacks. Probably the most prolific line of research at the moment concerns the silicene-graphene configuration [153, 91, 13]. However, in recent years, the possibility of growing stanene on graphene has been investigated in different theoretical works. The first-principle calculations proposed by Wu and co-workers [178] pointed out that stanene interacts with graphene via van der Waals interaction. Consequently, the preservation of their intrinsic electronic properties is to be expected. On the contrary, stronger interlayer interaction between stanene and graphene is reported in Ref. [27] together with an enhanced response of stanene in the visible spectral region. Both the theoretical works report on a band gap opening of the hybrid system. Experimental realization of stanene, using a monolayer graphene as buffer layer, has recently been reported on Cu(111) [177]. A uniform thickness and continuous morphology for stanene was demonstrated, as well as increased stability in air. Here the use of MOCVD-graphene as a template for the epitaxial growth of tin nanosheets in the 2D limit is reported. The main goal is to find a substrate passivation strategy to prevent the oxidation of newly deposited tin films thus obtain a quasi-freestanding stanene.

4.2.1 Experimental methods

High-quality monolayer graphene, grown on single side polished Al_2O_3(0001), has been used as substrate for tin nanosheets deposition. The 2-inch original wafer, provided by Aixtron, has been cleaved into $\sim 1 \times 1\ cm^2$ pieces using a commercial wafer saw. The cut was made on the clean side of the wafer and the effects of this operation on the graphene layer were evaluated via Raman and AFM analysis on the resulting slabs. Tin deposition on graphene was performed by molecular beam epitaxy (MBE) on degassed sample using a k-cell evaporator for which the flux rate was previously calibrated though a quartz micro-balance. Two samples, 0.5 and 1 nm-thick, were grown at room temperature (RT). Both were then covered by an amorphous aluminum oxide capping layer ($\sim$5 nm) in order to prevent their degradation in ambient conditions. The overall stacking is thus (from top to bottom)

a-$Al_2O_3/Sn/Gr/Al_2O_3(0001)$. Chemical properties of the samples were investigated in-situ by means XPS, monitoring the status of graphene and tin films at all stages of the growth. Raman spectroscopy was used to assess quality, doping and strain of graphene before and after the tin deposition. Raman maps over areas of $7 \times 7\mu^2$ were acquired in back-scattering configuration using a Renishaw InVia spectrometer equipped with 514 nm laser and 50× (N.A. 0.75) objective. The incident laser power was kept below 3 mW to avoid heating effects and sample damages. To gain a better understanding of both the nature of the tin nanosheets and their interaction with the underlying graphene, an optical characterization was also performed in the MIR-UV spectral range. The transmittance was measured at room temperature using a Cary 5000 spectrophotometer, covering the energy range between 0.3 and 6.5 eV. The optical conductivity of thin tin films was extracted though RefFIT by implementing a multilayer model [86].

4.2.2 Results and discussion

Substrate characterization

In order to address the lack of spectral features unequivocally attributable to tin nanosheets, we exploited the high sensitivity of Raman spectroscopy to changes induced on the graphene layer. By evaluating the effects of tin nanosheets deposition on the Raman response of graphene, indeed, it has been possible to gain information on the properties of the heterostructure. This is because, for a single layer of graphene, any shift or line widening of the G and 2D Raman peaks can be attributable to strain and/or doping in the material [90]. The quality of CVD-graphene on $Al_2O_3(0001)$ was monitored before and after the cutting of the pristine wafer and, subsequently, after the growth of the tin nanosheets. The reduction of the wafer into small slabs was necessary due to the smaller size of the MBE sample holder, accommodating samples up to 1 cm^2. A representative Raman spectrum of graphene on Al_2O_3 (0001), obtained from a single-point acquisition after cutting the sapphire wafer, is shown in Figure 4.6a. Here, fingerprints of the electron-phonon interaction in a single layer graphene are well recognizable. The statistical analysis, carried out on Raman maps acquired over several areas of 7×7 μm^2, returns the G band located at (1588 ± 1) cm^{-1} and the 2D band at (2690 ± 2) cm^{-1}, while the full width at half maximum (FWHM) of the 2D band is (40 ± 3) cm^{-1}. The latter value, although it is consistent with the expected value for the FWHM of the 2D peak in graphene on $Al_2O_3(0001)$, is higher than those recently reported for as-grown graphene on sapphire [114] and indicates a moderate crystalline quality. Moreover, the existence of the defect-active peak (D) located at ~ 1350 cm^{-1} confirms the presence of defects across the slabs. The Table 4.2 reports the values obtained from the statistical

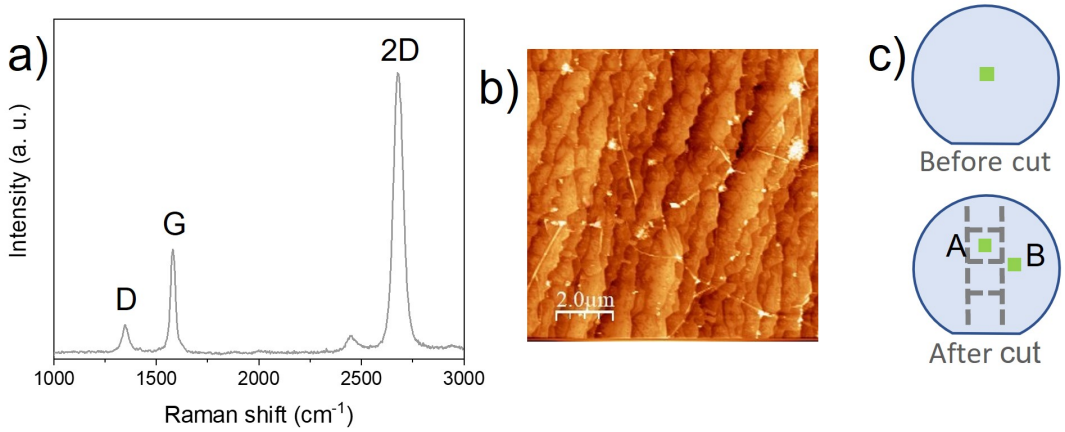

Fig. 4.6 a) Representative Raman spectrum of graphene on Al_2O_3(0001). b) Representative AFM image of terraces and wrinkles for graphene on Al_2O_3(0001) after the cutting process. c) Wafer sketches (non-scaled dimensions). The dashed grey lines (bottom) delimit the area of the slabs resulting from the cut. Green squares highlight the areas where Raman maps were acquired to determine initial and final conditions of graphene.

Table 4.2 Average value and standard deviation for FWHM, 2D/G and D/G obtained in the three different areas indicated in Figure 4.6 c.

Case	FWHM (cm^{-1})	Error (cm^{-1})	2D/G	Error	D/G	Error
Before cut	39	5	2.7	0.6	0.22	0.05
After cut - A	41	4	2.5	0.4	0.21	0.03
After cut - B	40	4	2.5	0.4	0.28	0.07

analysis performed on the three areas of the wafer highlighted (green squares) in Figure 4.6c. The FWHM of the 2D mode of graphene increases weakly, from 39 to 42 cm^{-1}, after the cut, indicating a slight deterioration in crystalline quality. At the same time the 2D/G and D/G intensity ratio, which are indicative of carrier and defect concentration respectively, do not vary significantly. Moreover, the values of the 2D/G intensity ratio (2.5 ± 0.2) indicate a low charge carrier concentration. According to the calibration curve reported by Das in Ref. [33] we estimate a carrier concentration of $\sim 1.5 \times 10^{12}$ cm^{-2}. In general the cutting procedure certainly lowered the overall quality of graphene on sapphire but did not compromise the properties detectable through Raman spectroscopy. The AFM images reported in Figure 4.6b confirm an high density of wrinkles on the slabs surface with a typical height of 1-5 nm. Such structures are consequence of the mismatch between the thermal expansion coefficient of graphene and sapphire and are often reported in literature [114, 29]. Scratches originating

from the substrate are also visible. These effects might justify the results of the Raman analysis described above.

Tin nanosheets growth

In situ XPS was carried out to check the chemical status of the tin nanosheets after the growth and after the a-Al_2O_3 capping deposition. The Sn $3d_{5/2}$ core level, for the 0.5 nm thick sample, is reported for both cases in Figure 4.7a-b. The spectra show a narrow peak related

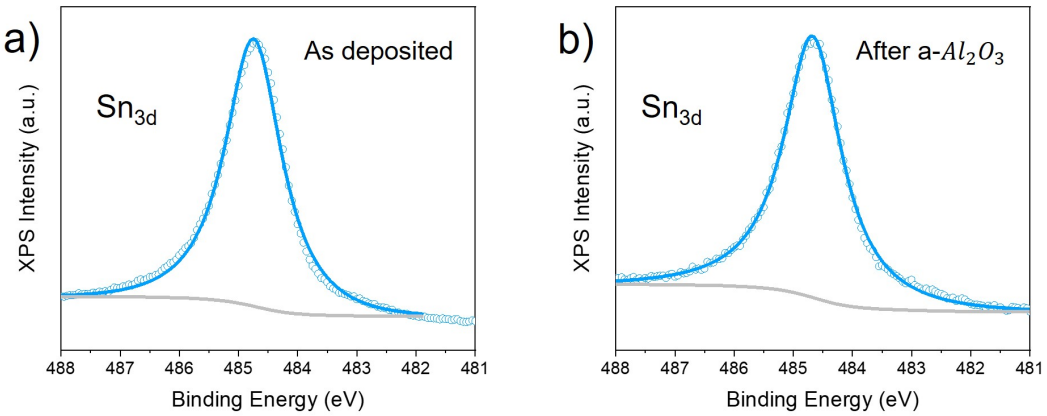

Fig. 4.7 XPS $Sn3d_{5/2}$ core level of 0.5 nm tin grown at RT on graphene a) before and b) after the capping layer deposition. Both spectra show only the Sn^0 (continuous line) component, which is related to the elemental state of tin. Open circles represent experimental data.

to the elemental tin, which is centered at $BE = 484.7$ eV with a $FWHM = 1.15$ eV. At room temperature, increasing the tin thickness to 1 nm, the XPS analysis still returns a spectrum with only one component, centered at the same location. The absence of any oxide-related component suggest that graphene is effective in limiting the chemical interaction between the tin nanosheets and the $Al_2O_3(0001)$ substrate. Moreover, the lack of additional components in the Sn $3d_{5/2}$ core level spectrum supports a framework in which the interaction between tin and graphene is low. After growth, the tin nanosheets were extracted from the vacuum condition and characterised by means of Raman spectroscopy. The Raman active phonon modes of stanene, α-Sn and β-Sn are generally expected in the spectral region between 100 and 500 cm^{-1} [147, 102, 154, 133] but neither Sn- nor stanene-related signatures have been detected in our samples. This fact, already reported in literature, could be traced back to the metallic nature of stanene [102, 36] or to substrate effects that do not promote the increase in signal generated by a few atomic layers. Optical interference is an example of the latter [96].

Raman correlation-map

The evolution of the Raman spectrum of graphene with increasing thickness of tin nanosheets is shown in Figure 4.8a. Clear variations in graphene Raman modes are the broadening of

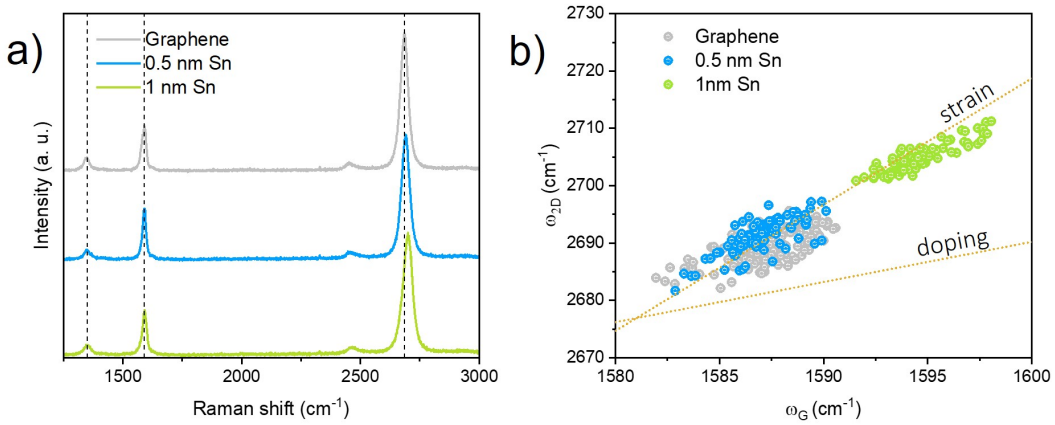

Fig. 4.8 a) Raman spectra of graphene before (gray) and after the growth of tin nanosheets 0.5 nm (blue) and 1 nm (green) thick. b) Correlation plot between the frequencies of the G and the 2D modes of graphene (ω_G, ω_{2D}) measured on pristine graphene and after the growth of tin nanosheets, 0.5 nm (blue) and 1 nm (green) thick. The "strain" orange line describes neutral-charge graphene under compressive or tensile strain. The "doping" orange line indicates p-type doped graphene.

the 2D mode and the blue-shift of the G and 2D modes. Specifically, the FWHM of the 2D peak in the spectra reported in Figure 4.8a increases with the thickness of deposited tin, from 35 for 0.5 nm to 42 cm^{-1} for a 1 nm thick nanosheet. Moreover, the D peak is still visible without any important variation suggesting that the quality of graphene has not been affected by the growth. As mentioned above, Raman spectroscopy is an highly useful method to extract information on doping and strain to which graphene is subjected. An inverse approach was thus used to shed light on the interaction between tin and graphene. We exploited the variation of the Raman response of graphene, induced by the deposition of tin films with different thicknesses, with the aim of gaining information on the resulting heterostructure. The correlation plot of the G peak Raman shift with the one of the 2D peak is reported in Figure 4.8b. The usefulness of this graphical representation lies in the fact that it makes possible to separate the contribution of doping and strain [90]. The two dashed orange lines specify the directions along which the strain-induced and the hole-doping induced shifts are expected. Moreover, the point where the two lines intersect, located at $(\omega_G^0, \omega_{2D}^0) = (1582, 2677)$, identifies graphene not affected by strain or excess charges[90]. The map points of the 0.5nm-thick sample are virtually superimposable on the bare graphene

map points. No substantial differences are observed between uncovered graphene and after the deposition of 0.5 nm-thick tin nanosheet. The dispersion, when tin nanosheets thickness increases, reveals that graphene is subject to increasing compressive strain while the effect on charge doping is practically negligible. Assuming an uniaxial strain-sensitivity of the G mode $\Delta\omega_G/\Delta\varepsilon = -23.5\ cm^{-1}/\%$ [185, 90] the corresponding compressive strain due to 1 nm-thick nanosheet deposition is about 0.5%. Interestingly, the type of stress undergone by graphene can provide information on the possible intercalation of tin atoms. It has recently been reported that under certain temperature and impurity conditions, silicene grown on graphene can exhibit intercalation [44]. In this case the Raman spectrum of graphene shows a splitting of the G peak and the 2D peak downshift which are indicative of the tensile strain experienced by graphene [115]. The different Raman response and the compressive strain to which graphene is subjected after the tin nanosheets deposition, leads to a first approximation to rule out intercalation effects. Finally, it is important to stress that effects such as desorption and intercalation occur mainly during high-temperature treatments, whereas all the samples scrutinized here were grown at room temperature.

Optical characterization

The optical response of the heterostructures formed by the tin nanosheets and graphene on Al_2O_3(0001) has been investigated by NIR-UV spectroscopy. Figure 4.9a shows the absolute transmittance for the two tin nanosheets samples, together with those for graphene on Al_2O_3(0001) and the bare substrate, in the photon energy range 0.3-6.5 eV. The lowering of reported transmittance spectra is consistent with an increase in absorption as the tin nanosheets gain in thickness. The insert also shows the fit results from which the optical constants for the different components of the heterostructures were extracted. The conductivity of graphene, 0.5 nm and 1 nm-thick tin nanosheet were obtained through fitting the NIR-UV measurements with the RefFIT software [86]. The transmittance of the samples, togheter with the substrate, was fitted by using a double (graphene-Al_2O_3) or a three (Sn-graphene-Al_2O_3) layers Kramers-Kronig consistent Drude-Lorentz model. The extracted real part $\sigma_1(\omega)$ of the optical conductivity was used to calculate the normalized optical conductance $G_1/G_0 = \sigma_1(\omega)d/G_0$ reported in Figure 4.9b, where d is the thickness of the considered layer and $G_0 = 2e^2/h$ is the universal conductance [87]. $G_1(\omega)$ for graphene shows the typical behaviour described by the superposition of a nearly flat background in the whole IR range (0.3-1.5 eV) due to the intraband transition [107], and an asymmetric absorption peak at ~ 4.6 eV. This feature is related, in the independent-particle description, to the interband transitions from the bonding π to the antibonding π^* states, near the saddle-point singularity at the M point of Brillouin zone [108]. At the lowest thickness of tin, $G_1(\omega)$ shows a small absorption

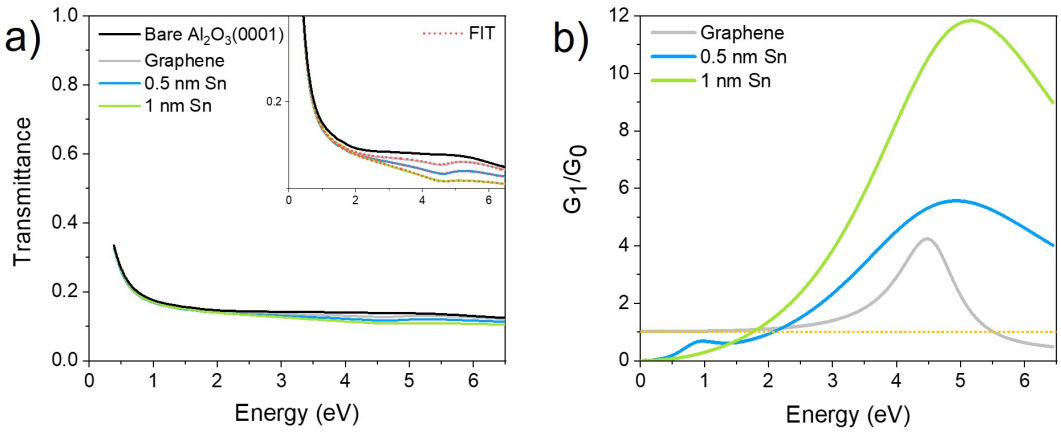

Fig. 4.9 a) Transmittance of supported graphene (gray), 0.5 nm (blue) and 1 nm (green) thick tin nanosheets. The bare Al_2O_3(0001) transmittance (black line) is reported as reference. b) Normalized optical conductance of graphene (gray), 0.5 nm (blue) and 1 nm (green) thick tin nanosheets, extracted from multi-layer models.

peak around 0.9 eV and rises around 1.5 eV up to the UV range. The maximum value occurs at $\sim$ 5 eV. When the tin nanosheet thickness increases to 1 nm, the absorption peak in the IR region disappear and the rise becomes steeper with a small maximum shift to higher energies. Surprisingly, both tin nanosheets exhibit an enhanced optical response compared to graphene, starting at $\sim$ 2 eV, as expected for the stanene-graphene heterostructure [27]. In order to clarify the origin of the spectral features described above for the tin nanosheets, Figure 4.10a compares the absorption coefficients $\alpha(\omega)$ of 0.5 and 1 nm-thick tin nanosheets, of the α- and β-tin [22, 160]. The optical behaviour of tin nanosheets deviates from that of the two allotropic form of tin. Towards low frequency, however, the way in which $\alpha(\omega)$ of tin nanosheets approach to zero is much more similar to that of α-Sn. As mentioned in previous sections, the general interest sparked by α-Sn is related to its non-trivial electronic and topological properties. α-Sn is a zero band-gap semiconductor [22] and, when strain is applied, α-Sn is expected to be a topological Dirac semi-metal [180]. Moreover, under moderate tensile strain it can turn into a topological insulator with a topological gap of $\sim$ 50 meV [154]. Epitaxy on lattice matched substrates has been reported as a possible approach to stabilize α-Sn [154, 39]. It is important to stress that the poor correspondence between the optical response of the tin nanosheets and the α-Sn might be attributed to the small thickness of the nanosheets compared to the reference (128 nm). Finally, Figure 4.10b reports the comparison between $\sigma_1(\omega)$ of the tin nanosheets and the calculated normalized absorbance of free-standing stanene as reported in Refs. [111] and [76]. The spectrum calculated by John *et al* [76] shows the best agreement with the experimental data for the broad peaks

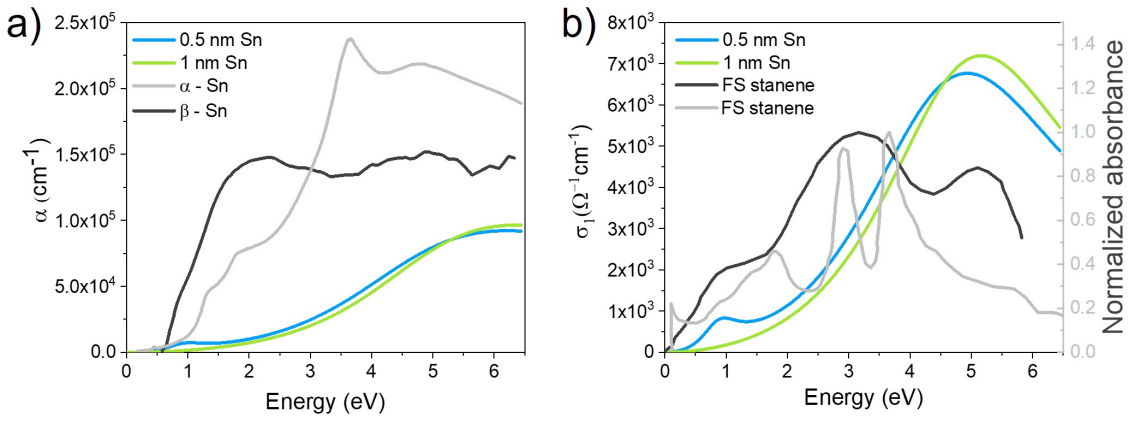

Fig. 4.10 a) Comparison between the absorption coefficients of 0.5 nm- (blue) and 1 nm-thick (green) tin nanosheets and those of α-Sn (gray) and β-Sn (black) (data from refs [22, 160]. b) Real part of the optical conductivity of 0.5 nm- (blue) and 1 nm-thick (green) tin nanosheets compared with the normalized absorbance of stanene reported in Ref. [111] (black) and Ref. [76] (gray).

at $\sim$1 and $\sim$5 eV. These absorption features are related to $\pi - \pi^*$ interband transitions and electronic transitions from p_x hybridized orbital and the π^*, respectively. The considerations that emerge from the comparisons in Figure 4.10a-b demonstrate once again the critical role of interlayer coupling in modifying the optical properties of a hybrid system.

The successful growth of non oxidized tin nanosheets at 2D limit has been reported. The structural characterization by Raman spectroscopy demonstrated that graphene after tin deposition turns out to be affected by compressive strain but not by charge transfer effects. The strain can be related to the interaction with tin overlayer which, however, shows no signs of intercalation. Optical measurements in the NIR-UV spectral range identify an increased absorption starting from 2 eV towards higher energies, as expected from theoretical calculations performed on stanene-graphene heterostructure. The poor correspondence with the calculated spectra of freestanding stanene can be attributed to strong interlayer interactions. In 2D heterostructured systems interlayer coupling can strongly modify the response of the individual components. More importantly, similarities were observed in the optical response of the tin nanosheets and the semi-metallic allotropic form of tin, suggesting the possibility of stabilising α-Sn on graphene-Al_2O_3(0001) at room temperature.

Chapter 5

Xenes heterostructures on Ag(111)

As mentioned in Chapter 4, the advent of 2D heterostructures is currently reshaping the frontiers of emerging materials research. The benefits of assembling layers of different materials include not only an increase in possible functionalities, but also a better stability of the single heterostruture components, and Xenes are certainly not excluded from this prospect. It has recently been shown that two well-established configurations such as silicene-on-Ag(111) [168] and stanene-on-Ag(111) [187] can operate as templates for the epitaxy of the reciprocal Xene single-layer, giving rise to two different types of Xene-based heterostructure [36]: (top-to-bottom) silicene-stanene on Ag(111) and stanene-silicene on Ag(111). Inserting one or more layers of Xenes between two different weakly interacting layers, with the aim of preserving their features, might be a successful strategy to move towards device integration. Moreover, the same approach could also prove useful for extracting all those properties that would otherwise be hidden by hybridization effects.

For epitaxial silicene, different experimental and theoretical studies pointed out that interface states, built up by mixed silicon and the native substrate wave functions, have a great impact on the its optical response. Moreover, to the best of our knowledge, for silicene on silver, no evidence is found of Si adlayers maintaining freestanding silicene optical properties [31, 69]. While the stability in air can be controlled by introducing a non-reactive capping layer such as amorphous Al_2O_3 [116], decoupling silicene and its substrate is still an unsolved issue. On this basis, the following chapter reports on the first optical characterization of silicene in the new silicene-stanene-Ag(111) configuration. The role of stanene as a 'buffer' layer is investigated by analyzing the optical response of epitaxial silicene through both power-dependent Raman spectroscopy and reflectance measurements in the near infrared (NIR) - ultraviolet (UV) spectral range.

5.1 Experimental methods

Silicene and stanene on commercial Ag(111)/mica substrates were deposited using the Scienta Omicron LAB10 MBE system described in Section 3.1. The samples realization took place in three steps: substrate preparation, growth, and encapsulation. Several cycles of sputtering and consecutive high temperature annealing (∼550 °C) were performed on Ag(111) substrates before Xenes growth. For heterostructures, first a Sn layer was deposited on the prepared substrate, then the Si layer is deposited on top of tin. The multilayered silicene samples were obtained by increasing the deposition time and monitoring thickness by means of a calibrated quartz microbalance. All samples were encapsulated with the non-reactive and amorphous Al_2O_3 capping layer to prevent degradation in ambient conditions. After the growth, Raman and NIR-UV spectroscopic characterizations were performed on the encapsulated samples. Raman measurements were carried out using a Jobin-Yvon T6400 spectrometer in back-scattering configuration with a continuous-wave 532 nm excitation and a 50× (0.75 numerical aperture) objective. To obtain the variation of Raman response versus the incident laser power a neutral density filter was added in the optical path and the samples surface was irradiated with a series of laser power from 1.8 to 60 mW. We measured the output laser power before the objective to take into account the laser energy loss in the optical path and the attenuation due to the filter. All spectra were acquired with an exposure time of 20 seconds, considering 3 accumulations. The samples were optically characterised through a JASCO 760v spectrometer, covering the NIR-UV spectral region, from 1.25 to 5 eV. The reflectance at near-normal incidence with respect to the sample surface (capping layer side) was measured by taking as reference an aluminum mirror. The possibility of neglecting the encapsulating layer from the optical analysis was confirmed by comparing the reflectance of bare and capped Ag. Several spectral acquisitions were performed to control experimental errors due to the extreme sensitivity of the reflectance to inhomogeneities and surface tilts. Both Raman and NIR-UV measurements were carried out at room temperature.

5.2 Results and discussion

The models of substrates and silicene-based configurations examined are shown in Figure 5.1 together with the respective Low Energy Electron Diffraction (LEED) patterns acquired *in-situ* during the different stages of growth. Keeping out the substrate column (panels a-b), from top to bottom, there are: (c) monolayer silicene directly grown on Ag(111), (d) monolayer silicene grown on stanene-Ag(111) template, (e) multilayer silicene on Ag(111)

and (f) multilayer silicene on stanene-Ag(111) template. The number of layers making up the multilayer structures was nominally set at three.

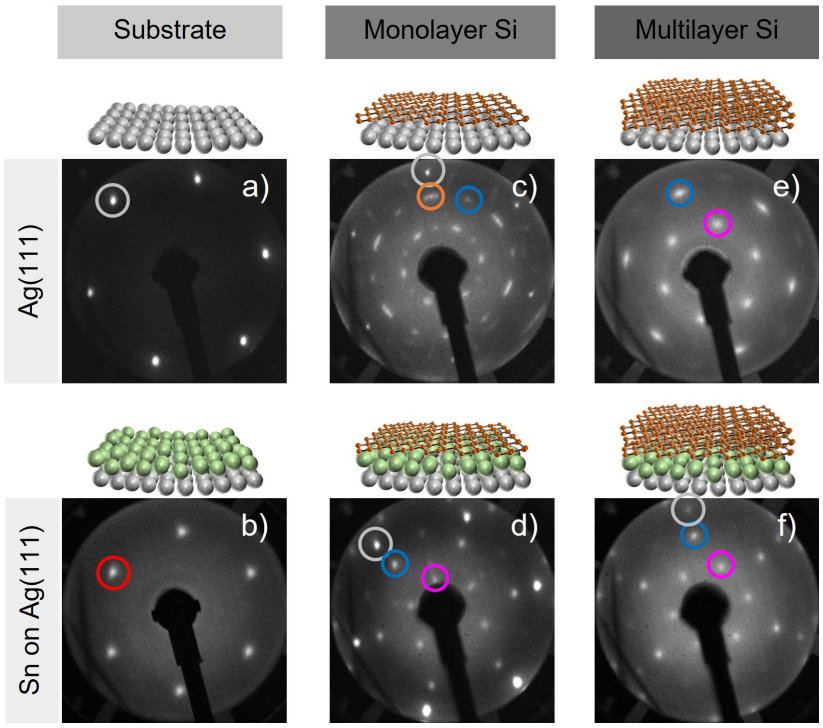

Fig. 5.1 Sketches and in-situ LEED characterization of substrate and Xenes stacking on Ag(111) substrate. LEED patterns obtained for: substrate templates (a) Ag(111) and (b) stanene on Ag(111), (c) monolayer silicene grown on Ag(111), (d) monolayer silicene grown on stanene-Ag(111), (e) multilayer silicene grown on Ag(111), (f) multilayer silicene grown on stanene-Ag(111). Color coding of solid circles: gray - Ag:1x1, red - $\sqrt{3} \times \sqrt{3}$ R30°order Sn spots, blue - integer order Si spots, orange - $\sqrt{13} \times \sqrt{13}$ *R*13.9°order Si spots, pink - $\sqrt{3} \times \sqrt{3}$ R30°order Si spots with respect to the integer order Si spots inside solid blue circles. The incident energy during LEED image acquisition is 50 eV except for (b), where the energy used is 33 eV.

In situ characterization

The LEED, presented in more detail in Section 3.2, is a surface-sensitive technique and is therefore indicative of the characteristic crystal structure of supported two-dimensional Xenes. The diffraction pattern of the just prepared Ag substrate, reported in Figure 5.1a, discloses the sharp hexagonal symmetry of its (111)-terminated surface. The subsequent deposition of (b) stanene on Ag(111) and (c) silicene on Ag(111) reproduce the relative structures previously observed for these configurations and confirm the epitaxial growth. In particular, Sn grows by assuming a $\sqrt{3} \times \sqrt{3}$ *R*30° reconstruction on the Ag(111)

surface [187], while silicene shows a mixed phase with the coexistence of spot from 4×4 and $\sqrt{13} \times \sqrt{13}$ $R13.9°$superstructures [120]. Silicene reconstructions for the single layer deposition and the multilayer on top of stanene-Ag(111) would be consistent with a $\sqrt{3} \times \sqrt{3}$ $R30°$structure, as well as multilayer silicene directly grown on Ag(111) [167]. However, it should be noted that further investigations are ongoing to clarify the mechanisms that determine the mutual distribution of tin and silicon atoms in heterostructures and thus shed light on the resulting surface reconstruction. After the *in situ* characterization, 5 nm-thick amorphous Al_2O_3 was deposited on the surface of the samples to prevent Xenes degradation throughout the ex-situ measurements [116].

Raman analysis

Representative optical images of silicene on Ag(111) and silicene on stanene-Ag(111) samples shown in Figure 5.2a-b highlight growth areas on the order of $\sim cm^2$. The large-scale homogeneity of Si depositions is supported by repeated Raman measurements performed at different positions over the whole surface of the samples.

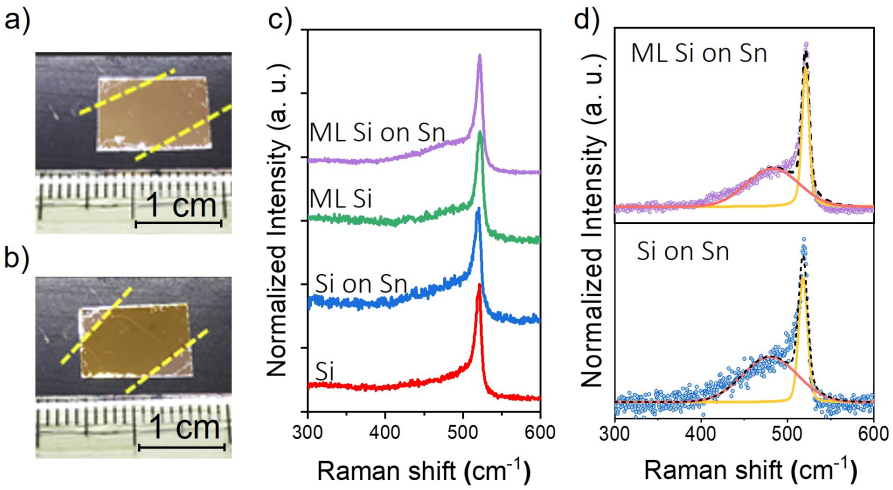

Fig. 5.2 Optical images of (a) silicene on Ag(111) and (b) silicene on stanene-Ag(111). Dashed yellow lines indicate the growth area. c) Room temperature normalized Raman spectra obtained at low incident laser power. d) Fitted Raman spectra of a multi- (top) and a single-layer (bottom) of silicene on stanene-Ag(111). In both cases the raw data are shown as circles (violet and blue respectively). Black dashed lines are the fit results, while yellow and orange curves are the two used Lorentzian-Gaussian components.

The preliminary Raman characterization of silicene in the configurations just described was performed at incident laser power below 3 mW to avoid damage and uncontrolled heating

effects. The spectra acquired with a laser power of 1.8 mW are reported in Figure 5.2c. The Raman analysis was carried out by fitting all the curves through a two-components Lorentzian-Gaussian model so that the typical asymmetric shape of silicene spectrum could be described. Indeed, as reported in Appendix B typical Raman spectrum of silicene is dominated by a sharp and intense peak in 515-522 cm^{-1} spectral range, due to the symmetric stretching of Si-Si atoms in planar hexagons (E_{2g} modes). Moreover, the vertical buckling is held accountable for the A_{1g} breathing mode that generates the asymmetric shoulder between 450 and 500 cm^{-1} [32]. In Figure 5.2d the fitting results for multilayer (top) and monolayer (bottom) silicene on stanene-Ag(111) are shown as an example. For a single layer of silicene, supported by Ag(111) or stanene-Ag(111), the spectra are dominated by an intense band located at 518 cm^{-1} with a full width half maximum (FWHM) of 8.0 cm^{-1} and 9.5 cm^{-1}, respectively. The fit results show a good agreement with the first order Raman peak expected for a low-dimensional crystalline silicon phase [32]. Conversely, for thicker samples the change of the spectral peak position to higher Raman shifts, up to 522 cm^{-1}, is consistent with the reported multilayer silicene growth [60]. It was also observed that the protection by a-Al_2O_3 encapsulation provide a durable preservation of the samples. This is confirmed by the Raman signal of silicene still detectable even after two months of air exposure (spectra not reported here).

At this point, it is worth noting that besides being used as a probe, laser excitation can also be applied to induce a localised temperature rise in the system under investigation. Briefly, due to the relatively small thicknesses involved in the case of 2D materials, even a low absorbed laser power can result in local heating and subsequent temperature rise in the surroundings of the illuminated area. Appreciable changes in the Raman spectrum due to the increase in temperature can be related to several physical properties at the very 2D level, which include anharmonic effects in the phonon-phonon interactions [163], thermal properties [21, 171, 47, 16], and thermal-mechanical response of the 2D layer [191, 49] to the optical absorbed power (see Section 3.3 for more details). To investigate the role of the stanene interlayer in modifying the interactions between silicene and silver, we analyzed the effect of laser-induced heating by taking the silicene-related Raman modes as a benchmark. The panels in Figure 5.3 show Raman spectra acquired by varying the incident laser power in the range 3.3-60 mW for silicene on Ag(111) (panel a), silicene on stanene-Ag(111) (panel b), multilayer silicene on Ag(111) (panel c) and multilayer silicene on stanene-Ag(111) (panel d). In contrast to silicene directly grown on Ag(111), the spectrum of silicene in contact with stanene shows a significant redshift ($\Delta\omega$) as the power of the incident radiation increases (see Figure 5.3b).

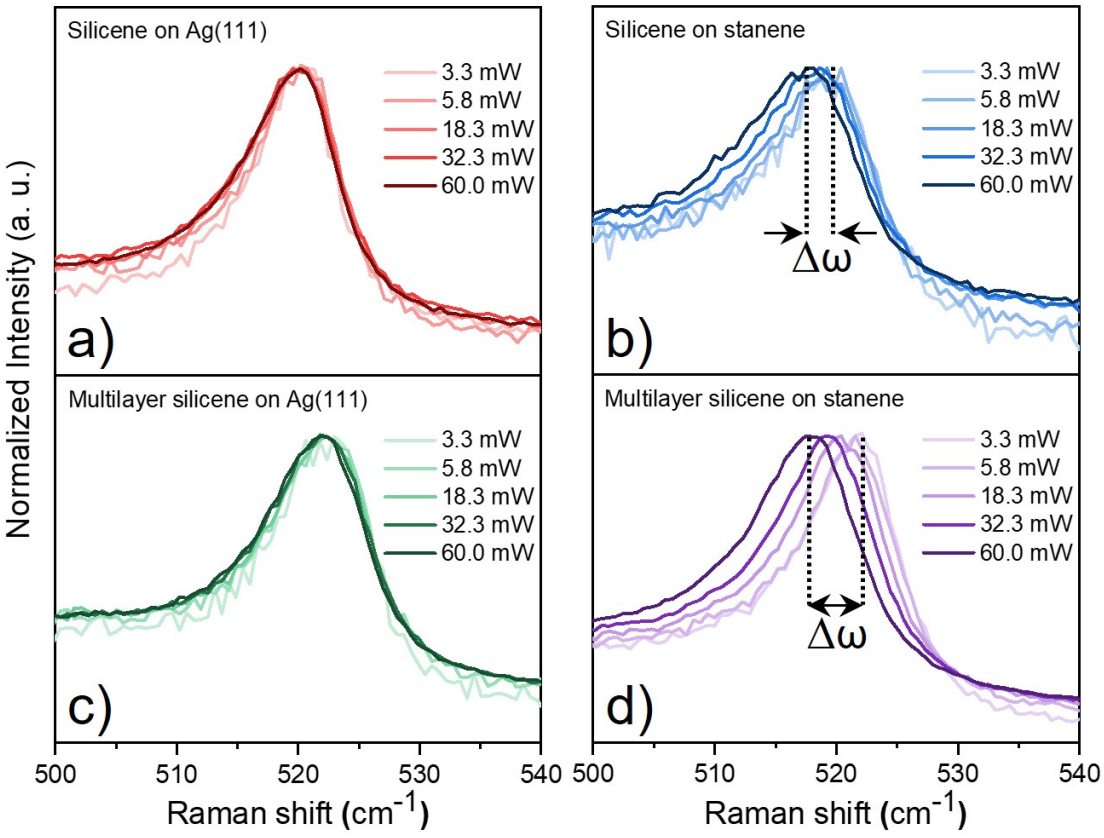

Fig. 5.3 Effect of the incident laser power increase on the Raman spectrum of (a) silicene, (b) silicene on stanene, (c) multilayer silicene and (d) multilayer silicene on stanene. All configurations are supported by an Ag(111) substrate.

Table 5.1 Results of linear fit applied to peak position data as a function of incident laser power.

Configuration	$\chi(cm^{-1}/mW)$	Error (cm^{-1}/mW)
Silicene	-0.009	0.002
Multilayer silicene	-0.012	0.001
Silicene on stanene	-0.035	0.003
Multilayer silicene on stanene	-0.069	0.003

As mentioned above and in agreement with the calibration curve reported by Solonenko et al. [151], the redshift is consistent with a local temperature increase. Moreover, it is clear that in the multilayer case, the power-dependent redshift is greater. Specifically, moving from an incident laser power of 3.3 to one of 60 mW, the silicene-related first-order Raman peak shifts by $\sim$0.8 cm^{-1} for multilayer silicene on Ag(111) and by $\sim$4.0 cm^{-1} for multilayer silicene with the same thickness, grown on stanene-Ag(111). Therefore, $\Delta\omega$ progressively increases when multiple silicene layers are grown on stanene, but in the same incident power range the effect is less evident if silicene layers are not separated from the Ag(111) substrate by the stanene interlayer. Interestingly, the heating process is reversible, suggesting that the power-dependent study does not induce structural modifications or damage to the silicene layers.

The trend of the Raman peak positions as a function of the incident laser power follows, to a good approximation, a linear behavior as it is shown in Figure 5.4a. Therefore, the heating-induced response can be quantifying by fitting data according to the equation $\omega(P) = \omega_0 + \chi P$, where ω_0 is the interpolated frequency when no laser power is applied, χ is the first order power coefficient and P is the incident laser power. The slope $\chi = \partial\omega/\partial P$ extracted for each of the scrutinized configurations and the standard error are given in Table 5.1. The modulus of the slope increases with the number of layers and is up to 6 times greater in samples where the stanene interlayer is present for the same number of silicene layers. Deviations among the power coefficient values confirm a distinct response of silicene on Ag(111) and silicene on stanene-Ag(111) to the incident laser power rise. Indeed, the trends observed in Figure 5.4a indicate that when silicene is in direct contact with the Ag(111) substrate the power dependence of $\Delta\omega$ is much weaker. The effect just described was examined in depth also assessing the dependence of the FWHM of the main peak to the incident laser power, as shown in Figure 5.4b. This study may indeed help to differentiate the mechanisms at the origin of the observed redshift. As a matter of fact, the Raman FWHM in unsupported 2D materials is more influenced by anharmonic phonon interactions than by thermal expansion effects [4, 85]. While the incident power dependence of the FWHM

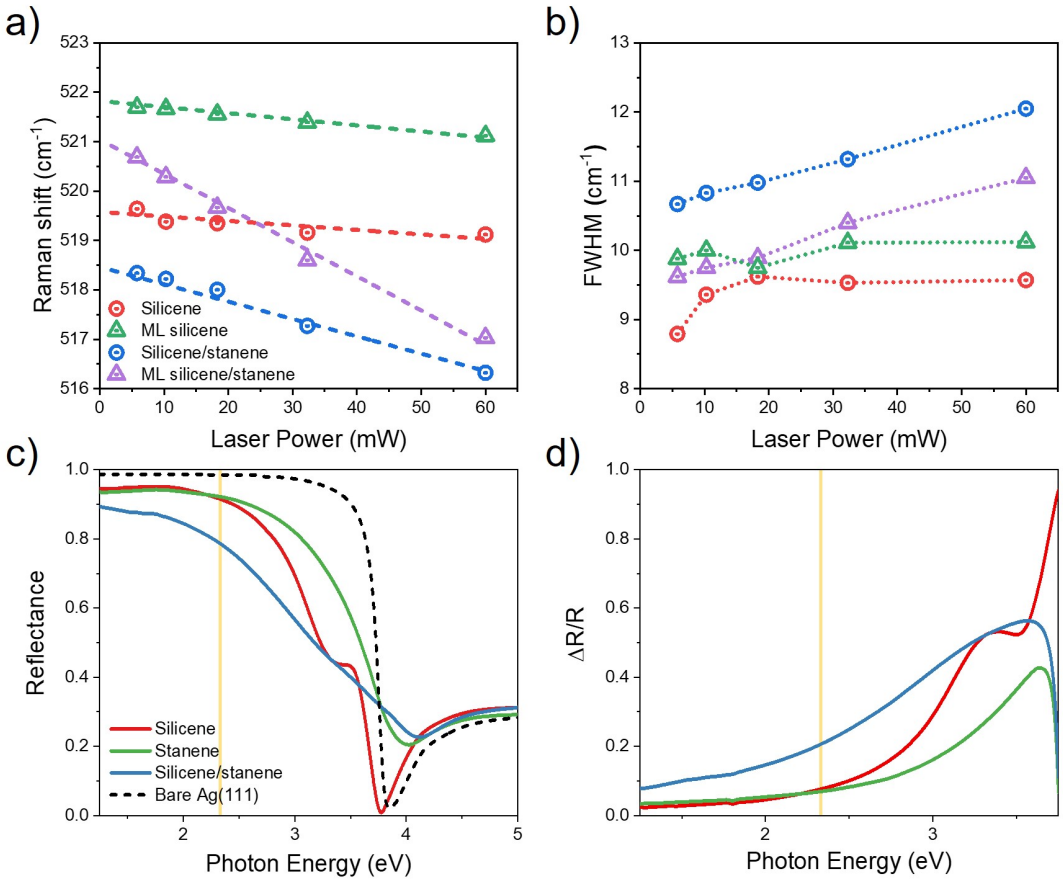

Fig. 5.4 First order silicene-related Raman peak (a)-position and (b)-full width at half maximum versus incident laser power, extracted from two-component fit analysis of the silicene Raman spectrum. In (a) the lines result from a linear fit made on the data distribution, while in the second one they are eye guides. c) Reflectance of bare silver (black dash), silicene/Ag(111) (red), stanene/Ag(111) (green) and silicene-stanene heterostructure/Ag(111) (blue) in the spectral range from 1.25 to 5 eV. d) Relative change of the reflectance caused by the Xene layers on the Ag(111) substrate. In (c) and (d) the yellow vertical line indicates the position of the laser frequency used during Raman characterization.

is weak for all configurations, it increases for silicene on stanene Ag(111) and shows a dependence on silicene thickness. Specifically, the increase in bandwidth as a function of laser power is maximum for the single layer of silicene on stanene Ag(111). On the other hand, the case of silicene on Ag(111) is similar to the multilayer heterostructure. Assuming that the increase of the thickness of silicene reduces the impact of the interface in the thermal dissipation is one possible explanation for this fact. In Section 3.3 is shown how the shift in the Raman spectrum can be caused by several effects such as the phonon-phonon anharmonic interaction, the deformation of the lattice due to the thermal energy contribution, and the effect of the mechanical strain induced by a thermal expansion coefficient mismatch between different layers. Therefore, considering the nearly power independent FWHM, the variation of $\Delta\omega$ reported in Figure 5.4a can be explained in terms of mechanical strain induced by a different thermal expansion coefficient mismatch in silicene-stanene interface compared with silicene-silver one [47].

In particular, the latter contribution calls for a deeper understanding of the interaction between silicene and the supporting substrate. Before turning to optical characterisation in the NIR-UV spectral range it is important to stress that the peak located at the lowest Raman shift in the decomposition of the spectrum of silicene was excluded from the discussion due to its broad spectral width. Indeed, regarding our method of analysis, with an initial FWHM of the order of tens of cm^{-1}, this component showed a completely negligible sensitivity to the laser-induced heating effect.

Optical characterization

To clarify the role of stanene layer in mediating silicene-silver interactions, a comparative study of the optical response of the heterostructure components was carried out in the NIR-UV spectral range. To achieve this, a control group was added to the previously studied set of samples. Several theoretical and experimental studies point the spectral range under investigation as being of exceptional interest in the study of the optical response of silicene and stanene. Indeed, it is between the IR and UV regions that some of the absorptions associated with the band structure of Xenes are expected (see Chapter 1). The analysed configurations with the NIR-UV spectroscopy are: bare Ag(111), Al_2O_3-silicene-Ag(111), Al_2O_3-stanene-Ag(111) and Al_2O_3-silicene-stanene-Ag(111). This new set of samples made it possible to experimentally observe the optical response of a monolayer of silicene, emphasizing the effect of the Si-Ag and Si-Sn interfaces, while simultaneously overshadowing the effects due to the increased number of silicene layers. The near-normal reflectance spectra, acquired in the photon energy range 1.25-5 eV, are shown in Figure 5.4c. All the reported curves are dominated by the substrate response although distinctive elements

can be attributed to silicene, stanene, or a combination of both. The main recognizable spectral feature is related to the silver plasma edge near 3.8 eV. For silver, this behaviour results from a combination between the free-carriers (intraband) response and the onset of interband electronic transitions [77]. In order to exclude effects due to the optical properties of the Ag(111) substrate and to highlight the response from Xenes, the change of the measured reflectance between 1.25 and 3.8 eV was considered. This quantity can be defined as:

$$\frac{\Delta R}{R} = \frac{R_{Substrate} - R_{Sample}}{R_{Substrate}} \tag{5.1}$$

where $R_{Substrate}$ and R_{Sample} are the reflectance of Ag(111) with and without the Xenes deposition, respectively. As already mentioned in Chapter 2.3, in the limit of two dimensions, the so-defined $\Delta R/R$ is proportional to the variation in the real part of the sheet conductivity and thus to the absorption of the considered thin film [111]. Based on this, the behaviour of the spectra shown in Figure 5.4d is strongly suggestive of the optical absorption of the Xenes layers. Interestingly, at the same photon energy used during Raman measurements, indicated by the vertical line in Figure 5.4c-d, the presence of the stanene layer in between silicene and Ag(111) results in an increase of $|\Delta R/R|$ which therefore also indicates an increase in optical absorption. It goes from 8% for the direct silicene/Ag coupling to 20% for the silicene-stanene heterostructure. This finding suggests that the higher slope, $\partial\omega/\partial P$, obtained for the heterostructure from the Raman measurements is due to an increase in the local temperature because of the optical absorption. We speculate that the distinct response may be due to a different thermal dissipation effect occurring at the silicene-silver and silicene-stanene interfaces.

The reflectance behaviour in various Xene configurations also discloses an unprecedented opportunity to gain a tunable optical response from silver by the Xene layer mediation. A thorough analysis of the reflectance spectra provided deeper insight in this respect. For a single layer of silicene on Ag(111) (red line in Figure 5.4c), the silver-related plasma edge shifts to lower photon energies and a small bump appears around 3.35 eV. The latter spectral feature can be traced back to the strong Si/Ag electronic interaction, as predicted within the density functional theory framework. Cinquanta and co-workers [31] have shown that electronic transitions involving mixed Si→Ag and Ag→Si states are responsible for almost all the absorption between 3 and 4 eV. Conversely, the presence of stanene on Ag (green line) strongly compensates for the silver plasma edge. The decrease of reflectance before its minimum value is less sharp and less deep than that observed for bare Ag(111) and it also results in a weak shift towards higher photon energies. Hence, single layer silicene and stanene yield different and opposite effects on the optical response of the system when

they are deposited separately on the Ag(111) surface. The former results in a shift of the reflectance minimum from 3.85 eV to 3.77 eV, whereas the latter to 4.02 eV. Moreover, as pointed out above, the reflectance of the silicene-stanene heterostructure (blue curve) shows a gradual decrease, and its minimum is still shifted to a higher photon energies as with the stanene layer. The plasma edge compensation is less steep than for a single layer of silicene or stanene. More importantly, the spectral marker at 3.35 eV is not present, thus confirming the role of the stanene layer in preventing the silicene/Ag electronic hybridization. As a final remark is is worth highlighting that, although the tuning of the plasmonic response by changing the local dielectric environment of the metal is well known, in the present case the shift of the silver plasma edge is obtained by combining different atomically thin layers. To explore the latter aspect, the dielectric functions (both real and imaginary part) of silicene on Ag(111) and stanene on Ag(111) were calculated starting from data reported in Figure 5.4c. The reflectance was fitted by employing a Drude-Lorentz model, which was subsequently refined by a Kramers-Kronig (K-K) constrained analysis [86]. At this stage of the analysis the fitting procedure neglects the thickness of the films, considering the spectrum variations due to Xene-silver interface effects. The obtained dielectric function components, ε_1 and ε_2, are shown in Figure 5.5a-b. The optical response of silicene-Ag(111) and stanene-Ag(111)

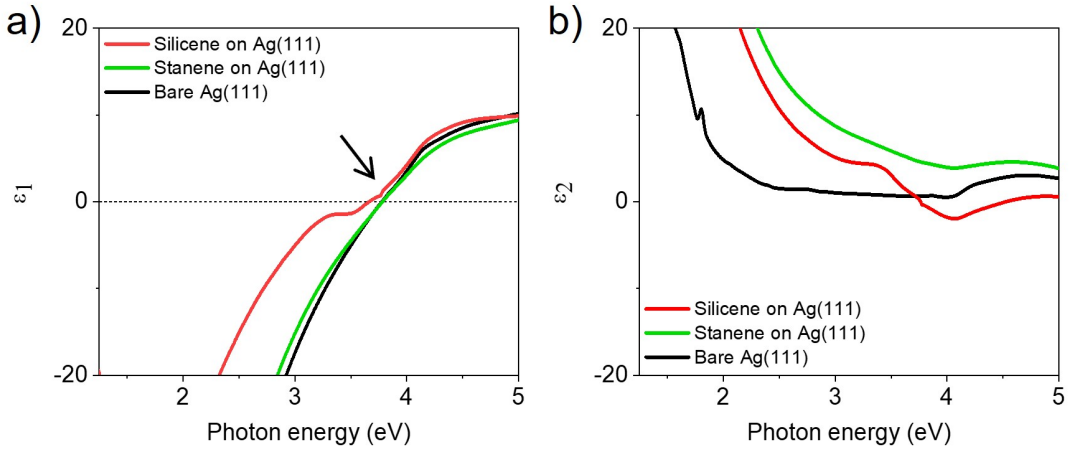

Fig. 5.5 (a) Real and (b) imaginary part of the dielectric function extracted from the reflectance spectra of bare Ag(111) (black), silicene on Ag(111) (green) and stanene on Ag(111) (blue).

shows remarkable differences in terms of spectral features around the silver plasma edge that reproduce those previously observed. In particular, the shift of the energy at which the real part of the dielectric function crosses the energy axis (indicated with a black arrow in Figure 5.5a) could be related to a change in the surface carrier density. Recalling the dispersion relation for SPs propagating at the interface between a metal and a dielectric

medium (Equation 2.25) introduced in Section 2.3, it is clear how the result obtained may have implications for the properties of surface plasmons (SPs) in the combined system. The optical response of the Xene systems described involves several different physical effects. For instance, the effective surface carrier density change does not necessary correspond to a change of bulk carrier density induced in the metal, and thus of the plasma frequency. A mechanism that can modulate the amplitude of the reflectivity can be also associated with an effective modification of optical damping (e.g. surface scattering) [40].

To summarise, the optical response of Xene-based heterostructures was investigated, paying particular attention to the properties of silicene in this new configuration. Although the indirect evaluation of the thermal response through the Raman spectroscopy, the results pave the way for the experimental investigation of the thermal properties of silicene. In particular, embedding silicene (or generally, other Xenes) in the heterostructure proves to be a viable layout to target thermoelectric applications as theoretically proposed [127, 194]. Moreover, a connection between the opto-thermal Raman response and the optical reflectance from differently configured silicene and silicene-stanene heterostructures on Ag(111) was established, pointing out the increased optical absorption in the visible spectral range. Surprisingly, in spite of experimental determination of effects due to each Xene is challenging, it was shown that the optical reflectance is conditioned by the detail of the Xene-silver interface, thus providing a quick tool for ex-situ identification of the heterostructure constituents. Finally, the Xene-induced shift of the silver plasma edge opens up the possibility of engineering the metal's plasmonic response by piling up Xene of different nature on top of the Ag(111) substrate.

Chapter 6

Plasmonic devices

The emergence of Dirac fermions in the absorption spectrum of epitaxial silicene-like nanosheets grown on Al_2O_3(0001) [61] strongly motivated the research activity presented in this chapter. On the basis of Xene-on-Al_2O_3(0001) configuration, the possibility of obtaining a plasmonic response from Xenes has been investigated, using as references some of the experiments carried out on graphene and reported in the literature (see Section 2.3). From these [79, 182] it is possible to identify two fundamental elements for studying Dirac plasmons: the periodic surface patterning and a strategy to modify (or control) the Fermi level of the system. On one hand, periodic structures can be used to locally concentrate fields with the aim to increase the absorption efficiency, on the other hand the ionic liquid gating allows doping to a high electron density.

Next sections report on tests performed on two Xene-on-Al_2O_3 configurations to assess their integrability in a plasmonic device. The structure of the devices that were analysed is shown in Figure 6.1a.

6.1 Micro-ribbon arrays fabrication

The trend in the optical conductivity of silicene-like nanosheets grown on sapphire at low frequencies suggests the existence of Dirac electrons, and hence plasmons [61]. However, these collective modes cannot be excited directly by the electromagnetic radiation because their dispersion law is such that momentum conservation in the photon absorption process is prevented (see Section 2.3). In other 2D systems the necessary extra momentum has been achieved by patterning the surface with a sub-wavelength grating [79, 37]. In this way, confined plasmons are obtained and detected. Plasmon excitation in such arrays correspond to collective oscillations of electrons across the width of the ribbons. Here this methodology has been applied to silicon nanosheets on Al_2O_3(0001) and tin nanosheets on graphene-

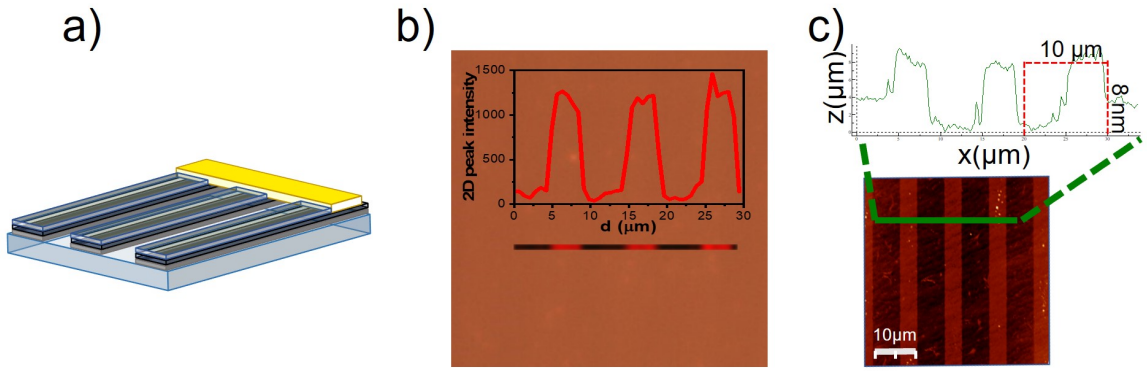

Fig. 6.1 Micro-ribbon arrays fabrication: a) Illustration of a typical micro-ribbon array in a-Al_2O_3-Sn-Gr-Al_2O_3(0001) sample. b) Superimposition of Raman mapping of the 2D graphene peak and an optical image of a patterned area. c) AFM image of a-Al_2O_3-Sn-Graphene micro-ribbon array with a nominal width of $5\mu m$ and a ribbon and gap width ratio of 1:1. The deviation from the expected result is a combination of several factors, first of all the isotropy of wet etching process.

Al_2O_3(0001). The stripes were fabricated by optical lithography and subsequent wet etching to remove the a-Al_2O_3 capping layer together with tin and silicon. Oxygen plasma etching (60 W, 5 min) was then used in order to remove the residual graphene. The optical lithography process is detailed in the Section 3.4. The micro-ribbon arrays had a width of $W = 5\mu m$ and period of 2W. The images in the Figure 6.1 and Figure 6.2 show representative results for the processes performed on the two type of samples.

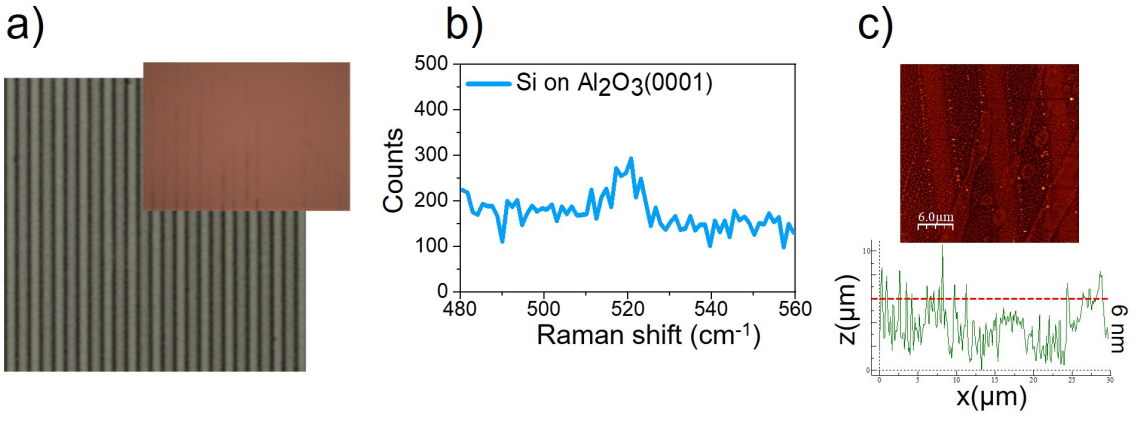

Fig. 6.2 Micro-ribbons array fabrication in 2D Si on Al_2O_3(0001) samples: a) Superimposition of optical images after the wet etching process with (big) and without (small) photo-resist. b) Raman signal collected from 3 nm-thick silicon nanosheet before photolithography. c) AFM image of the photo-lithography result on the 1.5 nm-thick silicon nanosheet sample.

With regard to tin nanosheets on graphene-Al_2O_3(0001), Figure 6.1b shows the hurdles of identifying the pattern once the photo-resist is removed. The existence of the pattern was verified by acquiring a linear Raman map following the graphene response and subsequently confirmed through an atomic force microscope (AFM). The AFM image in Figure 6.1c shows a fair agreement between the thickness of the removed material and the nominal one, which can be defined in a first approximation as the sum of the nominal thicknesses of the different layers (i. e. ~ 7 nm). Over-etching is also evident in the periodicity of the stripes, which is not completely maintained. This last effect can easily be traced back to the isotropy of the wet etching process. The difficulty of identifying the pattern after resist removal is also evident in the case of silicon nanosheets, as shown in Figure 6.2a. AFM mapping was required due to the low efficiency of Raman scattering on silicon films grown on sapphire, as shown by the spectrum in Figure 6.2b. The results of the AFM analysis, in Figure 6.2c, show the low quality of the grating obtained. The reason for this may be related to the initial quality of the films or the lack of control over the wet etching process of such thin films.

It is worth noting that tin films grown directly on Al_2O_3(0001) were not considered for the realisation of plasmonic gratings due to the lack of absorption in the optical response of tin nanosheets attributable to free electrons.

6.2 Ionic liquid gating implementation

For a given micro-ribbons array, the plasmon resonance can be tuned by changing the carrier concentration. According to the result reported in Section 2.3, the plasma frequency in a 2D Dirac system varies with carrier concentration as $n^{1/4}$. This is a signature of massless Dirac electrons. A method widely used to control the carrier concentration in 2D materials involves the ionic liquid (IL) gating introduced in Section 3.4. The use of ILs instead of dielectric materials provides an high charge injection for a relatively low operating voltage [33]. The IL chosen to control the carrier density in the Xene-based configurations is the [EMIM][TFSI], the main features of which are briefly described in Section 3.4. A dedicated setup (Figure 6.3b) was designed and realized on a printed circuit board in order to measure the optical response of the micro-ribbon arrays, as function of the applied gate voltage (V_G). In order to have good control of the IL thickness a pan of adhesive tape ($\sim 50\mu$m -thick) was applied and a co-planar arrangement during the optical characterization was preferred in most cases. A gold wire with a diameter of 0.25 μm was used as gate electrode.

Tests on graphene

Electrical characterisation of a device is undoubtedly the most accurate way to determine gating performance. In the absence of this possibility, the high sensitivity of Raman spectroscopy to changes induced on a graphene layer was exploited. In doped graphene, the doping-induced Fermi energy shift has two main effects: a change in the equilibrium lattice parameter with a consequent stiffening/softening of the phonons, and the onset of effects beyond the adiabatic Born-Oppenheimer approximation that modify the phonon dispersion close to the Kohn anomalies. In particular, the excess charge results in an expansion of the crystal lattice; conversely the defect results in its contraction. In both cases, this is reflected in the Raman response of graphene [140, 89, 33]. Specifically, the position of the G and 2D peaks together with the FWHM of the G peak vary as function of doping. 2D and G peaks show different dependencies on the gate voltage. For electron doping the position of the 2D peak does not change until high voltages, while for hole doping the shift in its position is more pronounced. The position of the G peak shifts visibly for both types of doping. The peak intensity also shows a characteristic trend with the level of doping [33, 25].

Therefore, the operation of the setup was first evaluated by monitoring the evolution of the position of the G peak of a sample of transferred graphene on SiO_2/Si, as a function of V_G. The trend followed by the G peak of graphene, shown in Figure 6.3a, is consistent with the sign of the voltage applied [33]. This test demonstrated the functionality of the system developed to modify the carrier density by IL gating. The experiment was then repeated on graphene supported by Al_2O_3(0001). In this case, a background signal due to the presence of the IL covers the Raman signal of graphene, as can be seen by comparing the intensities of the spectra in Figure 6.3c. The lower Raman efficiency observed here is due to a substrate effect [20, 21]. Overall, the lack of detectable spectral features for both Al_2O_3-supported graphene and Xene did not allow further evaluation with this method. Plasmonic devices were finally obtained by contacting the patterned samples. The Cr/Au contacts were fabricated by opening a channel in the a-Al_2O_3 capping layer.

6.3 Optical characterization of plasmonic gratings

Light-plasmon coupling in Xene-based devices has been investigated using polarized FT-IR spectroscopy. As reported in Section 2.3, for incident light polarized along the ribbons, the optical response due to the charge carriers is similar to that of free electrons in a homogeneous surface. In contrast, for incident light polarized perpendicular to the ribbons, the resulting spectrum should show an optical absorption originating from plasmons. Transmission and reflection configuration were combined in order to cover the IR spectral range between

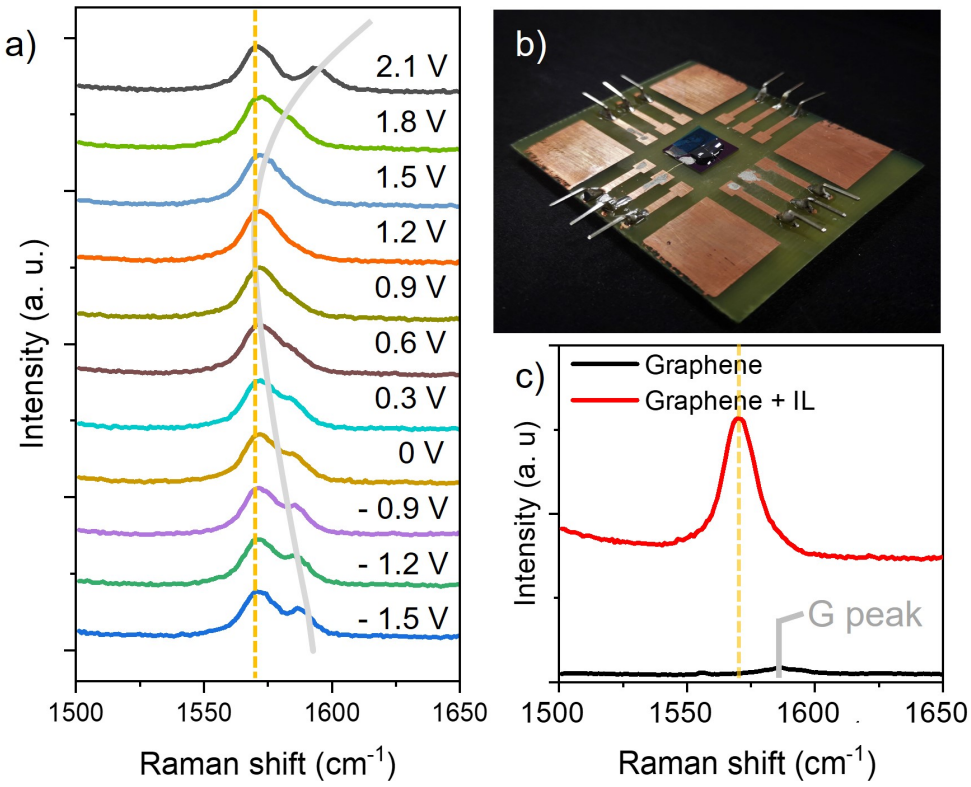

Fig. 6.3 Ionic liquid gating: a) Raman spectra of graphene on SiO_2/Si, at values of V_G between 2.1 V and -1.5 V. The grey line is a guide for the eyes whereas the dashed yellow line indicates an IL peak [84] that does not change as a function of V_G. b) Picture of the setup developed for the characterisation of Xene-based plasmonic devices. An opening for optical transmission measurements is located in the centre (below the sample). c) Comparison of the Raman spectrum of graphene on $Al_2O_3(0001)$ with that of the same system covered with the IL. The dashed yellow line indicates an IL peak.

150 and 7000 cm^{-1} (0.019-0.86 eV). The lower limit in this case was determined by the efficiency of the polariser. Transmittance measurements were performed in the transparency region of the substrate, while reflectance spectra were recorded in the Al_2O_3(0001) phonon absorption region, between 300 and 1200 cm^{-1}. An IR microscope coupled to the Bruker Vertex interferometer was used as described in Section 3.3. All the spectra were acquired in air and they were normalized to the optical response of the bare sapphire collected under the same experimental conditions. Before discussing the preliminary results reported in this section, it should be noted that the single side polished Al_2O_3(0001) substrate transmits up to the 50% of the incident radiation in its transparency regions, as shown in Figure 6.4.

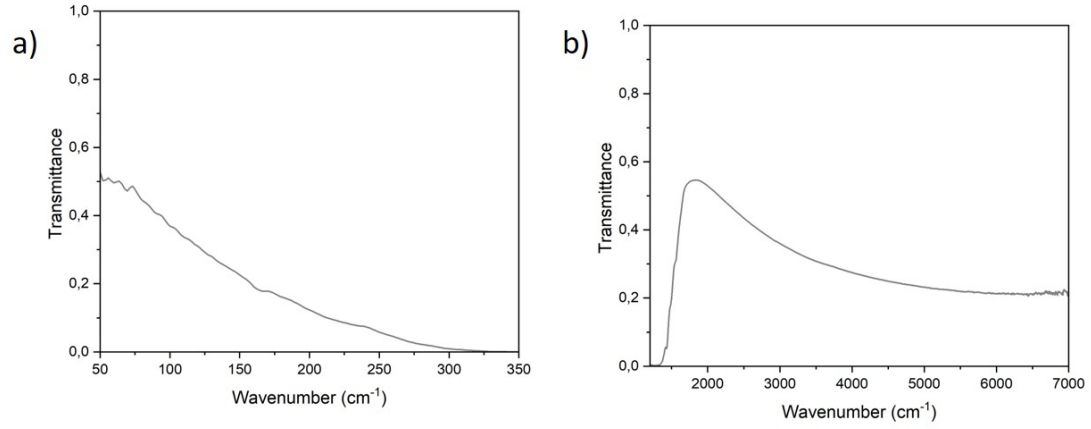

Fig. 6.4 Measured transmittance spectrum of 500 μm-thick single side polished Al_2O_3(0001) substrate. a) FIR spectral region, b) MIR spectral region.

The transmittance and reflectance were measured for two patterned configuration of Xene on Al_2O_3, namely Sn on graphene-Al_2O_3(0001) and Si on Al_2O_3(0001). Different spectra were also acquired under electrostatic doping. As can be seen from the representative spectra reported in Figure 6.5, no plasmon-related spectral features were detected in this experimental setup. Figure 6.5a shows the ratio 1-$R_{Sample}/R_{Substrate}$ calculated from the reflectance of patterned samples of graphene and 1nm Sn/graphene for the radiation electric field **E** parallel to the ribbons, between 300 and 800 cm^{-1}. The trend of the two curves is almost flat, with peaks around 500 cm^{-1} falling in the middle of the phonon absorption region of the substrate. Figure 6.5b presents the same quantity with **E** perpendicular to the ribbons. Although the direction is the same as that of the reciprocal lattice vectors required for energy-momentum conservation, no variation attributable to plasmonic excitation is observed. Transmission measurements in the 50-300 and 1200-7000 cm^{-1} ranges yielded similar results. In this case the extinction coefficient $E = 1 - T_{Sample}/T_{Substrate}$ was calculated from the correspondent

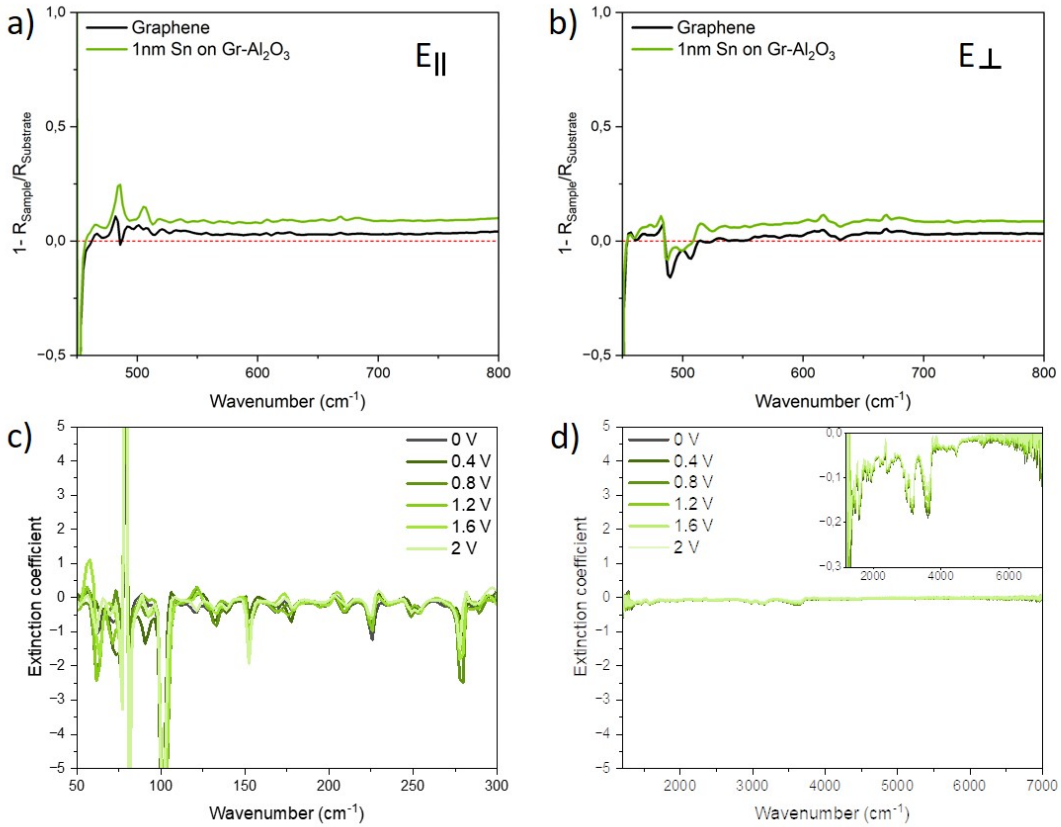

Fig. 6.5 a-b) Normalized reflectance of Gr-Al_2O_3 and 1nm-thick Sn on Gr-Al_2O_3 patterned samples with W=5μm and period 2W. The direction (a- parallel and b-perpendicular to the ribbons) of the radiation electric field is indicated. c-d) extinction coefficients of the same samples measured as function of the applied gate voltage V_g. The spectra are measured with the radiation electric field applied perpendicularly to the ribbons.

transmittance. The optical measurements on the patterned samples were then repeated by controlling the carrier concentration using the ion-liquid top gate. The gate-dependent optical response of 1nm-Sn on graphene-Al_2O_3 is reported in Figure 6.5 c-d, with **E** perpendicular to the ribbons. Although the trend of the extinction coefficients as a function of V_G is flat, the inset of Figure 6.5d shows a slight variation in the intensity of the spectra between 1000 and 4000 cm^{-1}. At this level, it seems reasonable to attribute the variation in the intensity of the signal to the water and not just to the water in the atmosphere [95]. In fact, water is recognized as one of the most important impurities in ILs [131]. The ionic nature results in a highly hygroscopic characteristic, the strength of which depends upon the exact cation-anion combination [38].

In summary, starting from prototypes with already known behaviour (e.g. graphene-based [79, 182]), the realisation of plasmonic devices has been systematically extended to the Xene-on-Al_2O_3(0001) platform. Experiments on graphene on SiO_2/Si demonstrate the operation of ionic liquid gating, but the reported preliminary results on the optical characterization of the devices do not show any plasmon-related absorption. The study of the plasmonic response of Xenes requires further investigation. Although the methods reported here are widely used in the scientific community, there is certainly room for improvement. Preliminary characterisations that provide information such as the carrier density in the 2D materials or a more precise choice in the doping control system are some of the aspects that will be addressed in the near future.

Conclusions

The advent of 2D materials has paved the way for the development of new technologies that would have been inaccessible until recently. Miniaturisation and low power consumption are the main drivers of this revolution, which is made possible by the existence of materials that are similar to graphene, but with extremely heterogeneous properties. The reduced dimensionality and the associated reduced dielectric screening of the Coulomb interactions between charge carriers determine a strong light-matter interaction that can be exploited in photonics and optoelectronics applications. Understanding the optical response of 2D materials and developing strategies to control it is a key issue in this regard.

The main objective of this work was the optical characterisation of different configurations based on silicon and tin nanosheets, within the 2D limit. To this end, I evaluated the effectiveness of different strategies to limit the interactions between stanene-like and silicon-like films and their native substrates. Specifically, two approaches were considered: the use of a commensurate insulating substrate, such as Al_2O_3(0001), and the engineering of the Ag(111) substrate through the introduction of a low-interacting buffer layer. The main achievements, together with some considerations on the feasibility of developing a Xene-based plasmonic device, are reported in the following.

Xenes on Al_2O_3(0001)

The absorption spectrum of tin nanosheets was determined by combining optical measurements in transmission and reflection mode over a spectral range from THz to UV. The main results in this respect are:

a) The epitaxial growth of tin nanosheets on an optically transparent substrate;

b) An optical behaviour that is different from that of tin oxides and conventional elemental tin phases;

c) Free-standing stanene signatures in the absorption spectra of the tin films.

The data show how the systematic use of an optically transparent substrate such as $Al_2O_3(0001)$ effectively allows the optical response of non-trivial materials to be measured at the 2D limit. Epitaxial tin films differ from the more common oxide forms and the elemental α and β phases in their optical behaviour. At the same time, regardless of the film growth temperature, the absorption spectrum showed spectral features traceable to those expected for stanene. Despite these promising results, the XPS spectra obtained during the growth process revealed the presence of oxidized tin components.

A different strategy has therefore been considered in order to control the interaction between tin and the $Al_2O_3(0001)$ substrate. This strategy consists of introducing a buffer layer of a different nature between the Xene and the desired substrate. Tin nanosheets were then grown on graphene-$Al_2O_3(0001)$ substrates by MBE. I have shown that this configuration can prevent tin oxidation as demonstrated by the XPS analysis. The observed optical response is consistent with the gray tin phase. Specifically, similarities with the α-Sn spectrum, suggest the possibility of stabilizing this phase at room temperature using graphene on $Al_2O_3(0001)$ as template.

Xene-based heterostructures

The introduction of an interlayer to limit the interaction with the substrate also proved to be a successful strategy in the case of silicene grown on Ag(111). In this regard, the main findings can be summarised as follows:

a) Decoupling of the silicene from the Ag substrate when introducing a layer of stanene;

b) Indirect access to the thermal response of silicene.

The reflectance measurements showed the absence of the spectral feature previously attributed to electronic transitions between hybridized Si-Ag states when a layer of stanene is placed between silicene and the Ag substrate. It was then possible to obtain information about the thermal behaviour of the silicene-stanene on Ag(111) heterostructure by means of the opto-thermal Raman spectroscopy. For the heterostructure, the position of the first-order Si-related Raman peak was extracted as a function of the incident radiation power. The trend was then compared with that obtained for silicene grown directly on Ag. Although it is an indirect assessment of fundamental response functions such as thermal conductivity, these observations can help to understand the properties and the potential of heterostructures and their components. In addition, this study leads the way for the evaluation of photothermal effects in silicene, which are critical for its integration into optoelectronic and photonic devices.

Plasmonic devices

A significant part of the research activity presented here has been devoted to the realization of devices to measure the plasmonic response potentially due to Dirac electrons hosted by Xenes. I focused on the a-Al_2O_3-Xene- Al_2O_3(0001) configuration to test the feasibility of transferring methods used in other two-dimensional system to a Xene-based platform. In particular, methods reported in the literature for determining the plasmonic response of graphene were applied to capped samples of silicon and tin/graphene nanosheets on Al_2O_3(0001). The surface of the samples was patterned with periodic micro-ribbon arrays using a lithographic mask I had designed. Various attempts have been made to optimise the etching process by varying the concentration, geometry and exposure time of the etchant solutions. To implement the ionic liquid gating, I realized a portable and reusable sample holder on a printed circuit board (PCB) that would also allow optical transmission measurements to be made. The temporary impossibility to electrically characterise the samples was circumvented by exploiting the sensitivity of the Raman spectroscopy to graphene properties such as the doping level. Periodic patterns were thus realised and the operation of ionic liquid gating on graphene was demonstrated.

Finally, a preliminary optical characterisation of the plasmonic gratings were reported. Although these results do not validate the Xenes-based platform, it may be helpful to analyse the critical issues that arose during the implementation of the plasmonic device in order to design new experiments. This is done by outlining the problems and proposing some solutions:

- Poor control of etching processes. It is extremely puzzling to optimise wet etching processes at such low thicknesses by adapting existing recipes, which were mainly developed on 3D systems
  $\rightarrow$ Moving to dry etching processes could lead to greater control and reproducibility of the patterns;

- The efficiency of ionic liquids is affected by their interaction with atmospheric water
  $\rightarrow$ using controlled environments (e. g., glove box), switching to ionic gels, selecting the most suitable ionic liquids;

- The lack of electrical characterisation of the Xenes and other systems under investigation makes it difficult to properly identify gating effects on Xenes
  $\rightarrow$ Preliminary characterisation and subsequent identification of the Fermi level.

With this in mind, it can be concluded that there is still room to evaluate the integration of the Xene-on-Al_2O_3(0001) platform into a working plasmonic device.

References

[1] Aguilar, R. V., Stier, A. V., Liu, W., Bilbro, L. S., George, D. K., Bansal, N., Wu, L., Cerne, J., Markelz, A. G., Oh, S., and Armitage, N. P. (2012). Terahertz response and colossal kerr rotation from the surface states of the topological insulator bi2se3. *Physical Review Letters*, 108:087403.

[2] Ahn, J. and Rabalais, J. (1997). Composition and structure of the al2o3{0001}-(1 × 1) surface. *Surface Science*, 388:121–131.

[3] Anker, J. N., Hall, W. P., Lyandres, O., Shah, N. C., Zhao, J., and Duyne, R. P. V. (2008). Biosensing with plasmonic nanosensors. *Nature Materials*, 7:442–453.

[4] Apostolov, A. T., Apostolova, I. N., and Wesselinowa, J. M. (2012). Temperature and layer number dependence of the g and 2d phonon energy and damping in graphene. *Journal of Physics: Condensed Matter*, 24:235401.

[5] Arafune, R., Lin, C.-L., Kawahara, K., Tsukahara, N., Minamitani, E., Kim, Y., Takagi, N., and Kawai, M. (2013). Structural transition of silicene on ag(111). *Surface Science*, 608:297–300.

[6] Autore, M., D'Apuzzo, F., Gaspare, A. D., Giliberti, V., Limaj, O., Roy, P., Brahlek, M., Koirala, N., Oh, S., de Abajo, F. J. G., and Lupi, S. (2015). Plasmon-phonon interactions in topological insulator microrings. *Advanced Optical Materials*, 3:1257–1263.

[7] Baehr-Jones, T., Spott, A., Ilic, R., Spott, A., Penkov, B., Asher, W., and Hochberg, M. (2010). Silicon-on-sapphire integrated waveguides for the mid-infrared. *Optics Express*, 18:12127.

[8] Balandin, A. A., Ghosh, S., Bao, W., Calizo, I., Teweldebrhan, D., Miao, F., and Lau, C. N. (2008). Superior thermal conductivity of single-layer graphene. *Nano Letters*, 8:902–907.

[9] Balkanski, M. and Wallis, R. F. (2000). *Semiconductor Physics and Applications*. Oxford University Press.

[10] Balkanski, M., Wallis, R. F., and Haro, E. (1983). Anharmonic effects in light scattering due to optical phonons in silicon. *Physical Review B*, 28:1928–1934.

[11] Bardeen, J. and Brattain, W. H. (1948). The transistor, a semi-conductor triode. *Physical Review*, 74:230–231.

[12] Barfuss, A., Dudy, L., Scholz, M. R., Roth, H., Höpfner, P., Blumenstein, C., Landolt, G., Dil, J. H., Plumb, N. C., Radovic, M., Bostwick, A., Rotenberg, E., Fleszar, A., Bihlmayer, G., Wortmann, D., Li, G., Hanke, W., Claessen, R., and Schafer, J. (2013). Elemental Topological Insulator with Tunable Fermi Level: Strained α-Sn on InSb(001). *Physical Review Letters*, 111(15):157205.

[13] Ben Jabra, Z., Abel, M., Fabbri, F., Aqua, J.-N., Koudia, M., Michon, A., Castrucci, P., Ronda, A., Vach, H., De Crescenzi, M., and Berbezier, I. (2022). Van der Waals Heteroepitaxy of Air-Stable Quasi-Free-Standing Silicene Layers on CVD Epitaxial Graphene-6H-SiC. *ACS Nano*, 16(4):5920–5931.

[14] Berciaud, S., Ryu, S., Brus, L. E., and Heinz, T. F. (2009). Probing the intrinsic properties of exfoliated graphene: Raman spectroscopy of free-standing monolayers. *Nano Letters*, 9:346–352.

[15] Biener, J., Bäumer, M., Madix, R., Liu, P., Nelson, E., Kendelewisz, T., and Brown, G. (2000). Growth and electronic structure of vanadium on α-Al2O3(0001). *Surface Science*, 449(1-3):50–60.

[16] Bonera, E. and Molle, A. (2022). Optothermal raman spectroscopy of black phosphorus on a gold substrate. *Nanomaterials*, 12:1410.

[17] Borensztein, Y., Curcella, A., Royer, S., and Prévot, G. (2015). Silicene multilayers on ag(111) display a cubic diamond-like structure and a $\sqrt{3} \times \sqrt{3}$ reconstruction induced by surfactant ag atoms. *Physical Review B*, 92:155407.

[18] Cahangirov, S., Topsakal, M., Aktürk, E., Şahin, H., and Ciraci, S. (2009). Two- and one-dimensional honeycomb structures of silicon and germanium. *Physical Review Letters*, 102:236804.

[19] Cai, B., Zhang, S., Hu, Z., Hu, Y., Zou, Y., and Zeng, H. (2015). Tinene: a two-dimensional dirac material with a 72 mev band gap. *Physical Chemistry Chemical Physics*, 17:12634–12638.

[20] Calizo, I., Bao, W., Miao, F., Lau, C. N., and Balandin, A. A. (2007). The effect of substrates on the raman spectrum of graphene: Graphene- on-sapphire and graphene-on-glass. *Applied Physics Letters*, 91:201904.

[21] Calizo, I., Ghosh, S., Bao, W., Miao, F., Lau, C. N., and Balandin, A. A. (2009). Raman nanometrology of graphene: Temperature and substrate effects. *Solid State Communications*, 149:1132–1135.

[22] Carrasco, R. A., Zamarripa, C. M., Zollner, S., Menendez, J., Chastang, S. A., Duan, J., Grzybowski, G. J., Claflin, B. B., and Kiefer, A. M. (2018). The direct bandgap of gray α -tin investigated by infrared ellipsometry. *Applied Physics Letters*, 113:232104.

[23] Casiraghi, C. (2009). Probing disorder and charged impurities in graphene by raman spectroscopy. *physica status solidi (RRL) - Rapid Research Letters*, 3:175–177.

[24] Castellanos-Gomez, A. (2016). Why all the fuss about 2d semiconductors? *Nature Photonics*, 10:202–204.

[25] Chen, C.-F., Park, C.-H., Boudouris, B. W., Horng, J., Geng, B., Girit, C., Zettl, A., Crommie, M. F., Segalman, R. A., Louie, S. G., and Wang, F. (2011). Controlling inelastic light scattering quantum pathways in graphene. *Nature*, 471:617–620.

[26] Chen, M. X., Zhong, Z., and Weinert, M. (2016a). Designing substrates for silicene and germanene: First-principles calculations. *Physical Review B*, 94:075409.

[27] Chen, X., Meng, R., Jiang, J., Liang, Q., Yang, Q., Tan, C., Sun, X., Zhang, S., and Ren, T. (2016b). Electronic structure and optical properties of graphene/stanene heterobilayer. *Physical Chemistry Chemical Physics*, 18(24):16302–16309.

[28] Chen, Z., Liu, Z., Wei, T., Yang, S., Dou, Z., Wang, Y., Ci, H., Chang, H., Qi, Y., Yan, J., Wang, J., Zhang, Y., Gao, P., Li, J., and Liu, Z. (2019). Improved epitaxy of aln film for deep-ultraviolet light-emitting diodes enabled by graphene. *Advanced Materials*, 31:1807345.

[29] Chen, Z., Xie, C., Wang, W., Zhao, J., Liu, B., Shan, J., Wang, X., Hong, M., Lin, L., Huang, L., Lin, X., Yang, S., Gao, X., Zhang, Y., Gao, P., Novoselov, K. S., Sun, J., and Liu, Z. (2021). Direct growth of wafer-scale highly oriented graphene on sapphire. *Science Advances*, 7(47):115.

[30] Cho, J. H., Lee, J., Xia, Y., Kim, B., He, Y., Renn, M. J., Lodge, T. P., and Frisbie, C. D. (2008). Printable ion-gel gate dielectrics for low-voltage polymer thin-film transistors on plastic. *Nature Materials*, 7:900–906.

[31] Cinquanta, E., Fratesi, G., dal Conte, S., Grazianetti, C., Scotognella, F., Stagira, S., Vozzi, C., Onida, G., and Molle, A. (2015). Optical response and ultrafast carrier dynamics of the silicene-silver interface. *Physical Review B*, 92:165427.

[32] Cinquanta, E., Scalise, E., Chiappe, D., Grazianetti, C., van den Broek, B., Houssa, M., Fanciulli, M., and Molle, A. (2013). Getting through the nature of silicene: An sp_2 -sp_3 two-dimensional silicon nanosheet. *The Journal of Physical Chemistry C*, 117:16719–16724.

[33] Das, A., Pisana, S., Chakraborty, B., Piscanec, S., Saha, S. K., Waghmare, U. V., Novoselov, K. S., Krishnamurthy, H. R., Geim, A. K., Ferrari, A. C., and Sood, A. K. (2008). Monitoring dopants by Raman scattering in an electrochemically top-gated graphene transistor. *Nature Nanotechnology*, 3(4):210–215.

[34] de Abajo, F. J. G. (2014). Graphene plasmonics: Challenges and opportunities. *ACS Photonics*, 1:135–152.

[35] Deng, J., Xia, B., Ma, X., Chen, H., Shan, H., Zhai, X., Li, B., Zhao, A., Xu, Y., Duan, W., Zhang, S.-C., Wang, B., and Hou, J. G. (2018). Epitaxial growth of ultraflat stanene with topological band inversion. *Nature Materials*, 17:1081–1086.

[36] Dhungana, D. S., Grazianetti, C., Martella, C., Achilli, S., Fratesi, G., and Molle, A. (2021). Two-dimensional silicene-stanene heterostructures by epitaxy. *Advanced Functional Materials*, 31:2102797.

[37] Di Pietro, P., Ortolani, M., Limaj, O., Di Gaspare, A., Giliberti, V., Giorgianni, F., Brahlek, M., Bansal, N., Koirala, N., Oh, S., Calvani, P., and Lupi, S. (2013). Observation of Dirac plasmons in a topological insulator. *Nature Nanotechnology*, 8(8):556–560.

[38] Doblinger, S., Donati, T. J., and Silvester, D. S. (2020). Effect of Humidity and Impurities on the Electrochemical Window of Ionic Liquids and Its Implications for Electroanalysis. *The Journal of Physical Chemistry C*, 124(37):20309–20319.

[39] Dong, X., Zhang, L., Yoon, M., and Zhang, P. (2021). The role of substrate on stabilizing new phases of two-dimensional tin. *2D Materials*, 8(4):045003.

[40] Dressel, M. and Gruner, G. (2002). *Electrodynamics of Solids*. Cambridge University Press.

[41] El-Fattah, Z. M. A., Mkhitaryan, V., Brede, J., Fernández, L., Li, C., Guo, Q., Ghosh, A., Echarri, A. R., Naveh, D., Xia, F., Ortega, J. E., and de Abajo, F. J. G. (2019). Plasmonics in atomically thin crystalline silver films. *ACS Nano*, 13:7771–7779.

[42] Elias, D. C., Nair, R. R., Mohiuddin, T. M. G., Morozov, S. V., Blake, P., Halsall, M. P., Ferrari, A. C., Boukhvalov, D. W., Katsnelson, M. I., Geim, A. K., and Novoselov, K. S. (2009). Control of graphene's properties by reversible hydrogenation: Evidence for graphane. *Science*, 323:610–613.

[43] Eng, P. J., Trainor, T. P., Brown Jr., G. E., Waychunas, G. A., Newville, M., Sutton, S. R., and Rivers, M. L. (2000). Structure of the Hydrated α-$Al_2O_3(0001)$ Surface. *Science*, 288(5468):1029–1033.

[44] Fabbri, F., Scarselli, M., Shetty, N., Kubatkin, S., Lara-Avila, S., Abel, M., Berbezier, I., Vach, H., Salvato, M., Crescenzi, M. D., and Castrucci, P. (2022). Silicene nanosheets intercalated in slightly defective epitaxial graphene on a 4h-sic(0001) substrate. *Surfaces and Interfaces*, 33:102262.

[45] Falson, J., Xu, Y., Liao, M., Zang, Y., Zhu, K., Wang, C., Zhang, Z., Liu, H., Duan, W., He, K., Liu, H., Smet, J. H., Zhang, D., and Xue, Q. K. (2020). Type-II Ising pairing in few-layer stanene. *Science*, 367(6485):1454–1457.

[46] Faraone, G. (2020). *Two-Dimensional Phosphorus: From the Synthesis Towards the Device Integration*. PhD thesis.

[47] Faraone, G., Sipala, R., Mariani, M., Martella, C., Grazianetti, C., Molle, A., and Bonera, E. (2021). Probing the laser ablation of black phosphorus by raman spectroscopy. *The Journal of Physical Chemistry C*, 125:8704–8711.

[48] Feng, B., Ding, Z., Meng, S., Yao, Y., He, X., Cheng, P., Chen, L., and Wu, K. (2012). Evidence of silicene in honeycomb structures of silicon on ag(111). *Nano Letters*, 12:3507–3511.

[49] Feng, Q., Wei, D., Su, Y., Zhou, Z., Wang, F., and Tian, C. (2021). Study of thermal expansion coefficient of graphene via raman micro-spectroscopy: Revisited. *Small*, 17:2006146.

[50] feng Zhu, F., jiong Chen, W., Xu, Y., lei Gao, C., dan Guan, D., hua Liu, C., Qian, D., Zhang, S.-C., and feng Jia, J. (2015). Epitaxial growth of two-dimensional stanene. *Nature Materials*, 14:1020–1025.

[51] Ferrari, A. C. and Basko, D. M. (2013). Raman spectroscopy as a versatile tool for studying the properties of graphene. *Nature Nanotechnology*, 8(4):235–246.

[52] Ferrari, A. C., Bonaccorso, F., Fal'ko, V., Novoselov, K. S., Roche, S., Bøggild, P., Borini, S., Koppens, F. H. L., Palermo, V., Pugno, N., Garrido, J. A., Sordan, R., Bianco, A., Ballerini, L., Prato, M., Lidorikis, E., Kivioja, J., Marinelli, C., Ryhänen, T., Morpurgo, A., Coleman, J. N., Nicolosi, V., Colombo, L., Fert, A., Garcia-Hernandez, M., Bachtold, A., Schneider, G. F., Guinea, F., Dekker, C., Barbone, M., Sun, Z., Galiotis, C., Grigorenko, A. N., Konstantatos, G., Kis, A., Katsnelson, M., Vandersypen, L., Loiseau, A., Morandi, V., Neumaier, D., Treossi, E., Pellegrini, V., Polini, M., Tredicucci, A., Williams, G. M., Hong, B. H., Ahn, J.-H., Kim, J. M., Zirath, H., van Wees, B. J., van der Zant, H., Occhipinti, L., Matteo, A. D., Kinloch, I. A., Seyller, T., Quesnel, E., Feng, X., Teo, K., Rupesinghe, N., Hakonen, P., Neil, S. R. T., Tannock, Q., Löfwander, T., and Kinaret, J. (2015). Science and technology roadmap for graphene, related two-dimensional crystals, and hybrid systems. *Nanoscale*, 7:4598–4810.

[53] Ferrari, A. C., Meyer, J. C., Scardaci, V., Casiraghi, C., Lazzeri, M., Mauri, F., Piscanec, S., Jiang, D., Novoselov, K. S., Roth, S., and Geim, A. K. (2006). Raman spectrum of graphene and graphene layers. *Physical Review Letters*, 97:187401.

[54] Fleurence, A., Friedlein, R., Ozaki, T., Kawai, H., Wang, Y., and Yamada-Takamura, Y. (2012). Experimental evidence for epitaxial silicene on diboride thin films. *Physical Review Letters*, 108:245501.

[55] French, R. H. (1990). Electronic band structure of al2o3, with comparison to alon and ain. *Journal of the American Ceramic Society*, 73:477–489.

[56] Genser, J., Nazzari, D., Ritter, V., Bethge, O., Watanabe, K., Taniguchi, T., Bertagnolli, E., Bechstedt, F., and Lugstein, A. (2021). Optical signatures of dirac electrodynamics for hbn-passivated silicene on au(111). *Nano Letters*, 21:5301–5307.

[57] Glover, R. E. and Tinkham, M. (1957). Conductivity of superconducting films for photon energies between 0.3 and 40ktc. *Physical Review*, 108:243–256.

[58] Gou, J., Kong, L., Li, H., Zhong, Q., Li, W., Cheng, P., Chen, L., and Wu, K. (2017). Strain-induced band engineering in monolayer stanene on sb(111). *Physical Review Materials*, 1:054004.

[59] Grazianetti, C., Cinquanta, E., and Molle, A. (2016). Two-dimensional silicon: the advent of silicene. *2D Materials*, 3:012001.

[60] Grazianetti, C., Cinquanta, E., Tao, L., Padova, P. D., Quaresima, C., Ottaviani, C., Akinwande, D., and Molle, A. (2017). Silicon nanosheets: Crossover between multilayer silicene and diamond-like growth regime. *ACS Nano*, 11:3376–3382.

[61] Grazianetti, C., De Rosa, S., Martella, C., Targa, P., Codegoni, D., Gori, P., Pulci, O., Molle, A., and Lupi, S. (2018). Optical Conductivity of Two-Dimensional Silicon: Evidence of Dirac Electrodynamics. *Nano Letters*, 18(11):7124–7132.

[62] Grazianetti, C., Martella, C., and Molle, A. (2020). The xenes generations: A taxonomy of epitaxial single-element 2d materials. *physica status solidi (RRL) – Rapid Research Letters*, 14:1900439.

[63] Griffiths, P. R. and de Haseth, J. A. (2007). *Fourier Transform Infrared Spectrometry*. John Wiley & Sons, Inc.

[64] Grigorenko, A. N., Polini, M., and Novoselov, K. S. (2012). Graphene plasmonics. *Nature Photonics*, 6:749–758.

[65] Haffner, C., Chelladurai, D., Fedoryshyn, Y., Josten, A., Baeuerle, B., Heni, W., Watanabe, T., Cui, T., Cheng, B., Saha, S., Elder, D. L., Dalton, L. R., Boltasseva, A., Shalaev, V. M., Kinsey, N., and Leuthold, J. (2018). Low-loss plasmon-assisted electro-optic modulator. *Nature*, 556:483–486.

[66] Hantanasirisakul, K. and Gogotsi, Y. (2018). Electronic and optical properties of 2d transition metal carbides and nitrides (mxenes). *Advanced Materials*, 30:1804779.

[67] Harbecke, B. (1986). Coherent and incoherent reflection and transmission of multilayer structures. *Applied Physics B Photophysics and Laser Chemistry*, 39:165–170.

[68] Hoang, A. T., Katiyar, A. K., Shin, H., Mishra, N., Forti, S., Coletti, C., and Ahn, J.-H. (2020). Epitaxial Growth of Wafer-Scale Molybdenum Disulfide-Graphene Heterostructures by Metal-Organic Vapor-Phase Epitaxy and Their Application in Photodetectors. *ACS Applied Materials & Interfaces*, 12(39):44335–44344.

[69] Hogan, C., Pulci, O., Gori, P., Bechstedt, F., Martin, D. S., Barritt, E. E., Curcella, A., Prevot, G., and Borensztein, Y. (2018). Optical properties of silicene, Si on Ag(111), and Si on Ag(110). *Physical Review B*, 97:195407.

[70] Houssa, M., Pourtois, G., Afanas'ev, V. V., and Stesmans, A. (2010). Can silicon behave like graphene? a first-principles study. *Applied Physics Letters*, 97:112106.

[71] Huang, H., Zhou, S., and Duan, W. (2016). Type-ii dirac fermions in the ptse2 class of transition metal dichalcogenides. *Physical Review B*, 94:121117.

[72] Huertas-Hernando, D., Guinea, F., and Brataas, A. (2006). Spin-orbit coupling in curved graphene, fullerenes, nanotubes, and nanotube caps. *Physical Review B*, 74:155426.

[73] Hufner, S. (2008). *Photoelectron Spectroscopy: Principles and Applications*. Springer Science & Business Media.

[74] Ipatova, I. P., Maradudin, A. A., and Wallis, R. F. (1967). Temperature dependence of the width of the fundamental lattice-vibration absorption peak in ionic crystals. ii. approximate numerical results. *Physical Review*, 155:882–895.

[75] Jeanmaire, D. L. and Duyne, R. P. V. (1977). Surface raman spectroelectrochemistry. *Journal of Electroanalytical Chemistry and Interfacial Electrochemistry*, 84:1–20.

[76] John, R. and Merlin, B. (2017). Optical properties of graphene, silicene, germanene, and stanene from ir to far uv - a first principles study. *Journal of Physics and Chemistry of Solids*, 110:307–315.

[77] Johnson, P. B. and Christy, R. W. (1972). Optical constants of the noble metals. *Physical Review B*, 6:4370–4379.

[78] Johnson, R., de la Houssaye, P., Chang, C., Chen, P.-F., Wood, M., Garcia, G., Lagnado, I., and Asbeck, P. (1998). Advanced thin-film silicon-on-sapphire technology: microwave circuit applications. *IEEE Transactions on Electron Devices*, 45:1047–1054.

[79] Ju, L., Geng, B., Horng, J., Girit, C., Martin, M., Hao, Z., Bechtel, H. A., Liang, X., Zettl, A., Shen, Y. R., and Wang, F. (2011). Graphene plasmonics for tunable terahertz metamaterials. *Nature Nanotechnology*, 6(10):630–634.

[80] Kane, C. L. and Mele, E. J. (2005a). Quantum spin hall effect in graphene. *Physical Review Letters*, 95:226801.

[81] Kane, C. L. and Mele, E. J. (2005b). Z2 topological order and the quantum spin hall effect. *Physical Review Letters*, 95:146802.

[82] Kauranen, M. and Zayats, A. V. (2012). Nonlinear plasmonics. *Nature Photonics*, 6:737–748.

[83] Khan, A., Islam, S. M., Ahmed, S., Kumar, R. R., Habib, M. R., Huang, K., Hu, M., Yu, X., and Yang, D. (2018). Direct cvd growth of graphene on technologically important dielectric and semiconducting substrates. *Advanced Science*, 5:1800050.

[84] Kiefer, J., Fries, J., and Leipertz, A. (2007). Experimental Vibrational Study of Imidazolium-Based Ionic Liquids: Raman and Infrared Spectra of 1-Ethyl-3-methylimidazolium Bis(Trifluoromethylsulfonyl)imide and 1-Ethyl-3-methylimidazolium Ethylsulfate. *Applied Spectroscopy*, 61(12):1306–1311.

[85] Kolesov, E. A., Tivanov, M. S., Korolik, O. V., Kapitanova, O. O., Cho, H. D., Kang, T. W., and Panin, G. N. (2019). Phonon anharmonicities in supported graphene. *Carbon*, 141:190–197.

[86] Kuzmenko, A. B. (2005). Kramers–Kronig constrained variational analysis of optical spectra. *Review of Scientific Instruments*, 76(8):083108.

[87] Kuzmenko, A. B., van Heumen, E., Carbone, F., and van der Marel, D. (2008). Universal optical conductance of graphite. *Physical Review Letters*, 100:117401.

[88] Kuzmenko, A., B. (2018). Guide to RefFIT - software to fit optical spectra.

[89] Lazzeri, M. and Mauri, F. (2006). Nonadiabatic kohn anomaly in a doped graphene monolayer. *Physical Review Letters*, 97:266407.

[90] Lee, J. E., Ahn, G., Shim, J., Lee, Y. S., and Ryu, S. (2012). Optical separation of mechanical strain from charge doping in graphene. *Nature Communications*, 3(1):1024.

[91] Li, G., Zhang, L., Xu, W., Pan, J., Song, S., Zhang, Y., Zhou, H., Wang, Y., Bao, L., Zhang, Y., Du, S., Ouyang, M., Pantelides, S. T., and Gao, H. (2018). Stable silicene in graphene/silicene van der waals heterostructures. *Advanced Materials*, 30:1804650.

[92] Li, J., Chen, M., Samad, A., Dong, H., Ray, A., Zhang, J., Jiang, X., Schwingenschlögl, U., Domke, J., Chen, C., Han, Y., Fritz, T., Ruoff, R. S., Tian, B., and Zhang, X. (2022). Wafer-scale single-crystal monolayer graphene grown on sapphire substrate. *Nature Materials*, 21(7):740–747.

[93] Li, Z. Q., Henriksen, E. A., Jiang, Z., Hao, Z., Martin, M. C., Kim, P., Stormer, H. L., and Basov, D. N. (2008). Dirac charge dynamics in graphene by infrared spectroscopy. *Nature Physics*, 4(7):532–535.

[94] Liao, M., Zang, Y., Guan, Z., Li, H., Gong, Y., Zhu, K., Hu, X.-P., Zhang, D., Xu, Y., Wang, Y.-Y., He, K., Ma, X.-C., Zhang, S.-C., and Xue, Q.-K. (2018). Superconductivity in few-layer stanene. *Nature Physics*, 14:344–348.

[95] Libnau, F. O., Kvalheim, O. M., Christy, A. A., and Toft, J. (1994). Spectra of water in the near- and mid-infrared region. *Vibrational Spectroscopy*, 7(3):243–254.

[96] Lien, D.-H., Kang, J. S., Amani, M., Chen, K., Tosun, M., Wang, H.-P., Roy, T., Eggleston, M. S., Wu, M. C., Dubey, M., Lee, S.-C., He, J.-H., and Javey, A. (2015). Engineering light outcoupling in 2d materials. *Nano Letters*, 15:1356–1361.

[97] Limaj, O., Lupi, S., Mattioli, F., Leoni, R., and Ortolani, M. (2011). Midinfrared surface plasmon sensor based on a substrateless metal mesh. *Applied Physics Letters*, 98:091902.

[98] Lin, J., Guo, L., Huang, Q., Jia, Y., Li, K., Lai, X., and Chen, X. (2011). Anharmonic phonon effects in raman spectra of unsupported vertical graphene sheets. *Physical Review B*, 83:125430.

[99] Liu, C.-C., Feng, W., and Yao, Y. (2011a). Quantum spin hall effect in silicene and two-dimensional germanium. *Physical Review Letters*, 107:076802.

[100] Liu, C.-C., Jiang, H., and Yao, Y. (2011b). Low-energy effective hamiltonian involving spin-orbit coupling in silicene and two-dimensional germanium and tin. *Physical Review B*, 84:195430.

[101] Liu, H., Gao, J., and Zhao, J. (2013). Silicene on substrates: A way to preserve or tune its electronic properties. *The Journal of Physical Chemistry C*, 117:10353–10359.

[102] Liu, Y., Gao, N., Zhuang, J., Liu, C., Wang, J., Hao, W., Dou, S. X., Zhao, J., and Du, Y. (2019). Realization of strained stanene by interface engineering. *The Journal of Physical Chemistry Letters*, 10:1558–1565.

[103] Liu, Z., Lee, H., Xiong, Y., Sun, C., and Zhang, X. (2007). Far-field optical hyperlens magnifying sub-diffraction-limited objects. *Science*, 315:1686–1686.

[104] Lupi, S. and Molle, A. (2020). Emerging dirac materials for thz plasmonics. *Applied Materials Today*, 20:100732.

[105] Mahatha, S. K., Moras, P., Sheverdyaeva, P. M., Flammini, R., Horn, K., and Carbone, C. (2015). Evidence for a diamondlike electronic band structure of si multilayers on ag(111). *Physical Review B*, 92:245127.

[106] Maier, S. A. (2007). *Plasmonics: Fundamentals and Applications*. Springer US, New York, NY.

[107] Mak, K. F., Sfeir, M. Y., Wu, Y., Lui, C. H., Misewich, J. A., and Heinz, T. F. (2008). Measurement of the Optical Conductivity of Graphene. *Physical Review Letters*, 101(19):196405.

[108] Mak, K. F., Shan, J., and Heinz, T. F. (2011). Seeing many-body effects in single- and few-layer graphene: Observation of two-dimensional saddle-point excitons. *Physical Review Letters*, 106:046401.

[109] Matthes, L., Gori, P., Pulci, O., and Bechstedt, F. (2013a). Universal infrared absorbance of two-dimensional honeycomb group-iv crystals. *Physical Review B*, 87:035438.

[110] Matthes, L., Pulci, O., and Bechstedt, F. (2013b). Massive dirac quasiparticles in the optical absorbance of graphene, silicene, germanene, and tinene. *Journal of Physics: Condensed Matter*, 25:395305.

[111] Matthes, L., Pulci, O., and Bechstedt, F. (2014). Optical properties of two-dimensional honeycomb crystals graphene, silicene, germanene, and tinene from first principles. *New Journal of Physics*, 16:105007.

[112] Meng, L., Wang, Y., Zhang, L., Du, S., Wu, R., Li, L., Zhang, Y., Li, G., Zhou, H., Hofer, W. A., and Gao, H.-J. (2013). Buckled silicene formation on ir(111). *Nano Letters*, 13:685–690.

[113] Min, H. and MacDonald, A. H. (2009). Origin of universal optical conductivity and optical stacking sequence identification in multilayer graphene. *Physical Review Letters*, 103:067402.

[114] Mishra, N., Forti, S., Fabbri, F., Martini, L., McAleese, C., Conran, B. R., Whelan, P. R., Shivayogimath, A., Jessen, B. S., Buss, L., Falta, J., Aliaj, I., Roddaro, S., Flege, J. I., Boggild, P., Teo, K. B. K., and Coletti, C. (2019). Wafer-Scale Synthesis of Graphene on Sapphire: Toward Fab-Compatible Graphene. *Small*, 15(50):1904906.

[115] Mohiuddin, T. M. G., Lombardo, A., Nair, R. R., Bonetti, A., Savini, G., Jalil, R., Bonini, N., Basko, D. M., Galiotis, C., Marzari, N., Novoselov, K. S., Geim, A. K., and Ferrari, A. C. (2009). Uniaxial strain in graphene by raman spectroscopy: G peak splitting, gruneisen parameters, and sample orientation. *Physical Review B*, 79:205433.

[116] Molle, A., Faraone, G., Lamperti, A., Chiappe, D., Cinquanta, E., Martella, C., Bonera, E., Scalise, E., and Grazianetti, C. (2021). Stability and universal encapsulation of epitaxial Xenes. *Faraday Discussions*, 227:171–183.

[117] Molle, A., Goldberger, J., Houssa, M., Xu, Y., Zhang, S.-C., and Akinwande, D. (2017). Buckled two-dimensional xene sheets. *Nature Materials*, 16:163–169.

[118] Molle, A. and Grazianetti, C. (2022). *Xenes: 2D Synthetic Materials Beyond Graphene*. Elsevier.

[119] Molle, A., Grazianetti, C., Chiappe, D., Cinquanta, E., Cianci, E., Tallarida, G., and Fanciulli, M. (2013). Hindering the oxidation of silicene with non-reactive encapsulation. *Advanced Functional Materials*, 23:4340–4344.

[120] Moras, P., Mentes, T. O., Sheverdyaeva, P. M., Locatelli, A., and Carbone, C. (2014). Coexistence of multiple silicene phases in silicon grown on ag(111). *Journal of Physics: Condensed Matter*, 26:185001.

[121] Nair, R. R., Blake, P., Grigorenko, A. N., Novoselov, K. S., Booth, T. J., Stauber, T., Peres, N. M. R., and Geim, A. K. (2008). Fine structure constant defines visual transparency of graphene. *Science*, 320:1308–1308.

[122] Nemanich, R., Lucovsky, G., and Solin, S. (1977). Infrared active optical vibrations of graphite. *Solid State Communications*, 23:117–120.

[123] Neto, A. H. C., Guinea, F., Peres, N. M. R., Novoselov, K. S., and Geim, A. K. (2009). The electronic properties of graphene. *Reviews of Modern Physics*, 81:109–162.

[124] Nie, S. and Emory, S. R. (1997). Probing single molecules and single nanoparticles by surface-enhanced raman scattering. *Science*, 275:1102–1106.

[125] Niu, C., Shepherd, K., Martini, D., Tong, J., Kelber, J., Jennison, D., and Bogicevic, A. (2000). Cu interactions with α-Al2O3(0001): effects of surface hydroxyl groups versus dehydroxylation by Ar-ion sputtering. *Surface Science*, 465(1-2):163–176.

[126] Nogueras, J. M. D. T. (2020). *Nanofabrication*. IOP Publishing Ltd.

[127] Noshin, M., Khan, A. I., and Subrina, S. (2018). Thermal transport characterization of stanene/silicene heterobilayer and stanene bilayer nanostructures. *Nanotechnology*, 29:185706.

[128] Novoselov, K. S., Geim, A. K., Morozov, S. V., Jiang, D., Zhang, Y., Dubonos, S. V., Grigorieva, I. V., and Firsov, A. A. (2004). Electric field effect in atomically thin carbon films. *Science*, 306:666–669.

[129] Novoselov, K. S., Mishchenko, A., Carvalho, A., and Neto, A. H. C. (2016). 2d materials and van der waals heterostructures. *Science*, 353.

[130] Novotny, L. and Hecht, B. (2012). *Principles of Nano-Optics*, volume 9781107005. Cambridge University Press.

[131] O Mahony, A. M., Silvester, D. S., Aldous, L., Hardacre, C., and Compton, R. G. (2008). Effect of Water on the Electrochemical Window and Potential Limits of Room-Temperature Ionic Liquids. *Journal of Chemical and Engineering Data*, 53(12):2884–2891.

[132] Ogo, Y., Hiramatsu, H., Nomura, K., Yanagi, H., Kamiya, T., Hirano, M., and Hosono, H. (2008). p-channel thin-film transistor using p-type oxide semiconductor, SnO. *Applied Physics Letters*, 93:032113.

[133] Olijnyk, H. (1992). Pressure dependence of raman phonons of metallic β-Sn. *Physical Review B*, 46:6589–6591.

[134] Padova, P. D., Ottaviani, C., Quaresima, C., Olivieri, B., Imperatori, P., Salomon, E., Angot, T., Quagliano, L., Romano, C., Vona, A., Muniz-Miranda, M., Generosi, A., Paci, B., and Lay, G. L. (2014). 24 h stability of thick multilayer silicene in air. *2D Materials*, 1:021003.

[135] Pan, X. Q. and Fu, L. (2001). Oxidation and phase transitions of epitaxial tin oxide thin films on ($\bar{1}$012) sapphire. *Journal of Applied Physics*, 89:6048–6055.

[136] Papadopoulos, C. (2014). *Solid-State Electronic Devices*. Springer New York.

[137] Peimyoo, N., Shang, J., Yang, W., Wang, Y., Cong, C., and Yu, T. (2015). Thermal conductivity determination of suspended mono- and bilayer ws2 by raman spectroscopy. *Nano Research*, 8:1210–1221.

[138] Piccinini, G., Forti, S., Martini, L., Pezzini, S., Miseikis, V., Starke, U., Fabbri, F., and Coletti, C. (2020). Deterministic direct growth of WS_2 on cvd graphene arrays. *2D Materials*, 7:014002.

[139] Pietro, P. D., Adhlakha, N., Piccirilli, F., Gaspare, A. D., Moon, J., Oh, S., Mitri, S. D., Spampinati, S., Perucchi, A., and Lupi, S. (2020). Terahertz tuning of dirac plasmons in bi2se3 topological insulator. *Physical Review Letters*, 124:226403.

[140] Pisana, S., Lazzeri, M., Casiraghi, C., Novoselov, K. S., Geim, A. K., Ferrari, A. C., and Mauri, F. (2007). Breakdown of the adiabatic born–oppenheimer approximation in graphene. *Nature Materials*, 6:198–201.

[141] Piscanec, S., Lazzeri, M., Mauri, F., Ferrari, A. C., and Robertson, J. (2004). Kohn anomalies and electron-phonon interactions in graphite. *Physical Review Letters*, 93:185503.

[142] Ritchie, R., Arakawa, E., Cowan, J., and Hamm, R. (1968). Surface-plasmon resonance effect in grating diffraction. *Physical Review Letters*, 21:1530–1533.

[143] Rivero, P., Yan, J.-A., García-Suárez, V. M., Ferrer, J., and Barraza-Lopez, S. (2014). Stability and properties of high-buckled two-dimensional tin and lead. *Physical Review B*, 90:241408.

[144] Robinson, J. T., Burgess, J. S., Junkermeier, C. E., Badescu, S. C., Reinecke, T. L., Perkins, F. K., Zalalutdniov, M. K., Baldwin, J. W., Culbertson, J. C., Sheehan, P. E., and Snow, E. S. (2010). Properties of fluorinated graphene films. *Nano Letters*, 10:3001–3005.

[145] Sahoo, S. K. and Wei, K. (2019). A perspective on recent advances in 2d stanene nanosheets. *Advanced Materials Interfaces*, 6:1900752.

[146] Sarma, S. D. and Hwang, E. H. (2009). Collective modes of the massless dirac plasma. *Physical Review Letters*, 102:206412.

[147] Saxena, S., Chaudhary, R. P., and Shukla, S. (2016). Stanene: Atomically thick free-standing layer of 2d hexagonal tin. *Scientific Reports*, 6:31073.

[148] Scalise, E., Houssa, M., Pourtois, G., van den Broek, B., Afanas'ev, V., and Stesmans, A. (2013). Vibrational properties of silicene and germanene. *Nano Research*, 6:19–28.

[149] Shanthi, E., Dutta, V., Banerjee, A., and Chopra, K. L. (1980). Electrical and optical properties of undoped and antimony-doped tin oxide films. *Journal of Applied Physics*, 51:6243–6251.

[150] Shirai, T., Shirasawa, T., Hirahara, T., Fukui, N., Takahashi, T., and Hasegawa, S. (2014). Structure determination of multilayer silicene grown on ag(111) films by electron diffraction: Evidence for ag segregation at the surface. *Physical Review B*, 89:241403.

[151] Solonenko, D., Gordan, O. D., Lay, G. L., Zahn, D. R. T., and Vogt, P. (2017). Comprehensive raman study of epitaxial silicene-related phases on $Ag(111)$. *Beilstein Journal of Nanotechnology*, 8:1357–1365.

[152] Solonenko, D., Gordan, O. D., Lay, G. L., Şahin, H., Cahangirov, S., Zahn, D. R. T., and Vogt, P. (2016). 2d vibrational properties of epitaxial silicene on ag(111). *2D Materials*, 4:015008.

[153] Sone, J., Yamagami, T., Nakatsuji, K., and Hirayama, H. (2016). Si growth at graphene surfaces on 6H-SiC(0001) substrates. *Japanese Journal of Applied Physics*, 55:035502.

[154] Song, H., Yao, J., Ding, Y., Gu, Y., Deng, Y., Lu, M.-H., Lu, H., and Chen, Y.-F. (2019). Thermal stability enhancement in epitaxial alpha tin films by strain engineering. *Advanced Engineering Materials*, 21:1900410.

[155] Song, J. C. W. and Gabor, N. M. (2018). Electron quantum metamaterials in van der waals heterostructures. *Nature Nanotechnology*, 13:986–993.

[156] Sorger, V. J., Lanzillotti-Kimura, N. D., Ma, R.-M., and Zhang, X. (2012). Ultra-compact silicon nanophotonic modulator with broadband response. *Nanophotonics*, 1:17–22.

[157] Stranick, M. A. and Moskwa, A. (1993a). SnO by XPS. *Surface Science Spectra*, 2(1):45–49.

[158] Stranick, M. A. and Moskwa, A. (1993b). SnO2 by XPS. *Surface Science Spectra*, 2(1):50–54.

[159] Takeda, K. and Shiraishi, K. (1994). Theoretical possibility of stage corrugation in si and ge analogs of graphite. *Physical Review B*, 50:14916–14922.

[160] Takeuchi, K. and Adachi, S. (2009). Optical properties of β-sn films. *Journal of Applied Physics*, 105:073520.

[161] Tang, P., Chen, P., Cao, W., Huang, H., Cahangirov, S., Xian, L., Xu, Y., Zhang, S.-C., Duan, W., and Rubio, A. (2014). Stable two-dimensional dumbbell stanene: A quantum spin hall insulator. *Physical Review B*, 90:121408.

[162] Tortello, M., Sola, A., Sharda, K., Paolucci, F., Nair, J. R., Gerbaldi, C., Daghero, D., and Gonnelli, R. S. (2013). Huge field-effect surface charge injection and conductance modulation in metallic thin films by electrochemical gating. *Applied Surface Science*, 269:17–22.

[163] Tristant, D., Cupo, A., Ling, X., and Meunier, V. (2019). Phonon anharmonicity in few layer black phosphorus. *ACS Nano*, 13:10456–10468.

[164] Velicky, M. (2021). Electrolyte versus Dielectric Gating of Two-Dimensional Materials. *J. Phys. Chem. C*, 125:21803–21809.

[165] Verri, G. G. G. and Voon, L. C. L. Y. (2007). Electronic structure of silicon-based nanostructures. *Physical Review B*, 76:075131.

[166] Via, L., Höchst, H., and Cardona, M. (1985). Dielectric function of α-sn and its temperature dependence. *Physical Review B*, 31:958–967.

[167] Vogt, P., Capiod, P., Berthe, M., Resta, A., Padova, P. D., Bruhn, T., Lay, G. L., and Grandidier, B. (2014). Synthesis and electrical conductivity of multilayer silicene. *Applied Physics Letters*, 104:021602.

[168] Vogt, P., Padova, P. D., Quaresima, C., Avila, J., Frantzeskakis, E., Asensio, M. C., Resta, A., Ealet, B., and Lay, G. L. (2012). Silicene: Compelling experimental evidence for graphene like two-dimensional silicon. *Physical Review Letters*, 108:155501.

[169] Wang, H., Pi, S. T., Kim, J., Wang, Z., Fu, H. H., and Wu, R. Q. (2016). Possibility of realizing quantum spin hall effect at room temperature in stanene/al2o3(0001). *Physical Review B*, 94:035112.

[170] Wang, Q. H., Kalantar-Zadeh, K., Kis, A., Coleman, J. N., and Strano, M. S. (2012). Electronics and optoelectronics of two-dimensional transition metal dichalcogenides. *Nature Nanotechnology*, 7:699–712.

[171] Wang, T., Wang, R., Yuan, P., Xu, S., Liu, J., and Wang, X. (2017). Interfacial thermal conductance between mechanically exfoliated black phosphorus and sio: Effect of thickness and temperature. *Advanced Materials Interfaces*, 4:1700233.

[172] Wei, W., Dai, Y., Huang, B., Whangbo, M.-H., and Jacob, T. (2015). Loss of linear band dispersion and trigonal structure in silicene on ir(111). *The Journal of Physical Chemistry Letters*, 6:1065–1070.

[173] West, P., Ishii, S., Naik, G., Emani, N., Shalaev, V., and Boltasseva, A. (2010). Searching for better plasmonic materials. *Laser & Photonics Reviews*, 4:795–808.

[174] Wintterlin, J. and Bocquet, M.-L. (2009). Graphene on metal surfaces. *Surface Science*, 603:1841–1852.

[175] Woodruff, D. (2016). *Low Energy Electron Diffraction*. Elsevier.

[176] Wooten, F. (1972). *Optical Properties of Solids*. Academic Press.

[177] Wu, H., Tang, J., Liang, Q., Shi, B., Niu, Y., Si, J., Liao, Q., and Dou, W. (2019). A van der Waals epitaxial growth of ultrathin two-dimensional Sn film on graphene covered Cu(111) substrate. *Applied Physics Letters*, 115(14):141601.

[178] Wu, L., Lu, P., Bi, J., Yang, C., Song, Y., Guan, P., and Wang, S. (2016). Structural and electronic properties of two-dimensional stanene and graphene heterostructure. *Nanoscale Research Letters*, 11(1).

[179] Xu, C.-Z., Chan, Y.-H., Chen, P., Wang, X., Flötotto, D., Hlevyack, J. A., Bian, G., Mo, S.-K., Chou, M.-Y., and Chiang, T.-C. (2018). Gapped electronic structure of epitaxial stanene on insb(111). *Physical Review B*, 97:035122.

[180] Xu, C.-Z., Chan, Y.-H., Chen, Y., Chen, P., Wang, X., Dejoie, C., Wong, M.-H., Hlevyack, J. A., Ryu, H., Kee, H.-Y., Tamura, N., Chou, M.-Y., Hussain, Z., Mo, S.-K., and Chiang, T.-C. (2017). Elemental Topological Dirac Semimetal: α-Sn on InSb(111). *Physical Review Letters*, 118(14):146402.

[181] Xu, Y., Yan, B., Zhang, H.-J., Wang, J., Xu, G., Tang, P., Duan, W., and Zhang, S.-C. (2013). Large-gap quantum spin hall insulators in tin films. *Physical Review Letters*, 111:136804.

[182] Yan, H., Low, T., Zhu, W., Wu, Y., Freitag, M., Li, X., Guinea, F., Avouris, P., and Xia, F. (2013). Damping pathways of mid-infrared plasmons in graphene nanostructures. *Nature Photonics*, 7:394–399.

[183] Yan, M., Huang, H., Zhang, K., Wang, E., Yao, W., Deng, K., Wan, G., Zhang, H., Arita, M., Yang, H., Sun, Z., Yao, H., Wu, Y., Fan, S., Duan, W., and Zhou, S. (2017). Lorentz-violating type-ii dirac fermions in transition metal dichalcogenide ptte2. *Nature Communications*, 8:257.

[184] Yao, Y., Ye, F., Qi, X.-L., Zhang, S.-C., and Fang, Z. (2007). Spin-orbit gap of graphene: First-principles calculations. *Physical Review B*, 75:041401.

[185] Yoon, D., Son, Y.-W., and Cheong, H. (2011). Strain-dependent splitting of the double-resonance raman scattering band in graphene. *Physical Review Letters*, 106:155502.

[186] Yu, P. Y. and Cardona, M. (2010). *Fundamentals of Semiconductors*. Springer Berlin Heidelberg.

[187] Yuhara, J., Fujii, Y., Nishino, K., Isobe, N., Nakatake, M., Xian, L., Rubio, A., and Lay, G. L. (2018). Large area planar stanene epitaxially grown on Ag(111). *2D Materials*, 5.

[188] Zhang, H., Liu, C.-X., Qi, X.-L., Dai, X., Fang, Z., and Zhang, S.-C. (2009). Topological insulators in Bi_2Se_3, Bi_2Te_3 and Sb_2Te_3 with a single dirac cone on the surface. *Nature Physics*, 5:438–442.

[189] Zhang, K., Feng, Y., Wang, F., Yang, Z., and Wang, J. (2017). Two dimensional hexagonal boron nitride (2d-hbn): synthesis, properties and applications. *Journal of Materials Chemistry C*, 5:11992–12022.

[190] Zhang, K., Wang, M., Zhou, X., Wang, Y., Shen, S., Deng, K., Peng, H., Li, J., Lai, X., Zhang, L., Wu, Y., Duan, W., Yu, P., and Zhou, S. (2021). Growth of large scale ptte, ptte2 and ptse2 films on a wide range of substrates. *Nano Research*, 14:1663–1667.

[191] Zhang, L., Lu, Z., Song, Y., Zhao, L., Bhatia, B., Bagnall, K. R., and Wang, E. N. (2019). Thermal expansion coefficient of monolayer molybdenum disulfide using micro-raman spectroscopy. *Nano Letters*, 19:4745–4751.

[192] Zhang, S., Sun, N., He, X., Lu, X., and Zhang, X. (2006). Physical properties of ionic liquids: Database and evaluation. *Journal of Physical and Chemical Reference Data*, 35:1475–1517.

[193] Zhao, M., Hao, Y., Zhang, C., Zhai, R., Liu, B., Liu, W., Wang, C., Jafri, S. H. M., Razaq, A., Papadakis, R., Liu, J., Ye, X., Zheng, X., and Li, H. (2022). Advances in two-dimensional materials for optoelectronics applications. *Crystals*, 12:1087.

[194] Zhu, B., Chen, Q., Jiang, S., Holt, M., Zhu, W., Akinwande, D., and Tao, L. (2021). Thermoelectric effect and devices on iva and va xenes. *InfoMat*, 3:271–292.

Appendix A

Methods for optical analysis

A.1 Applied models

FTIR spectroscopy, combined with NIR-UV spectroscopy, makes it possible to cover a wide energy range. The measurable optical parameters are transmittance and reflectance as function of photon energy which are defined as:

$$T(\omega) = \frac{I_T(\omega)}{I_0(\omega)} \qquad R(\omega) = \frac{I_R(\omega)}{I_0(\omega)}$$

$I_0(\omega)$ is the intensity of incident radiation, whereas $I_T(\omega)$ and $I_R(\omega)$ are the intensities of transmitted and reflected radiation by the sample under investigation. $T(\omega)$ and $R(\omega)$ can be related to the microscopic optical properties of materials via the Fresnel's equations. Before defining and making explicit the Fresnel' equations, it is worth to recall a general result obtained by solving Maxwell's equations and given in Chapter 3.2. The response of a media under an electric field is fully described by $\varepsilon(\tilde{q},\omega)$ and $\sigma(\tilde{q},\omega)$:

$$\varepsilon(\tilde{q},\omega) = 1 + \frac{i\sigma(\tilde{q},\omega)}{\varepsilon_0\omega} \tag{A.1}$$

$\varepsilon(\tilde{q},\omega)$ and $\sigma(\tilde{q},\omega)$ represent the microscopic properties of matter and they can be defined as complex quantities to take into account the propagation and dissipation of electromagnetic waves. In the spectral range between FIR and UV, the radiation enabling to investigate the response of excitations at $\tilde{q} \sim 0$ and thus to obtain information on the low-energy electrodynamics.

Solving Maxwell's equations also yields other important relations such as the dispersion relation between the complex wavevector $\tilde{q}$ and the frequency ω:

$$\tilde{q} = \frac{\omega}{c}[\tilde{\varepsilon} + i\frac{4\pi\tilde{\sigma}}{\omega}]^{\frac{1}{2}}\hat{n} \tag{A.2}$$

where $\hat{n}$ is the versor along the $\tilde{q}$ direction. The complex refractive index appears in the following relation:

$$\tilde{q} = \frac{\omega}{c}\tilde{n} = \frac{\omega}{c}(n + i\kappa) = \frac{\omega}{c}[\tilde{\varepsilon} + i\frac{4\pi\tilde{\sigma}}{\omega}]^{\frac{1}{2}} \tag{A.3}$$

where n is the refractive index and κ is the extinction coefficient. The last two quantities are completely determined by the complex conductivity and dielectric function:

$$n^2 - \kappa^2 = \varepsilon_1 = 1 - \frac{4\pi\sigma_2}{\omega} \tag{A.4}$$

$$2n\kappa = \frac{4\pi\sigma_1}{\omega} = \varepsilon_2 \tag{A.5}$$

On the other hand Fresnel's equations describe the experimental optical function $R(\omega)$ and $T(\omega)$ in terms of coefficients of reflection and transmission. These relations specify the amplitude of the coefficients at the interface between two transparent homogeneous media and they may be considered the starting point for making clear the close connection that exists between $R(\omega)$, $T(\omega)$ and the microscopic optical properties.
In the special configuration of normal incidence, Fresnel's equations assume the form:

$$\hat{r}_{12} = \frac{\tilde{n}_2 - \tilde{n}_1}{\tilde{n}_2 + \tilde{n}_1} \tag{A.6a}$$

$$\hat{t}_{12} = \frac{\tilde{n}_2}{\tilde{n}_1 + \tilde{n}_2} \tag{A.6b}$$

where $\tilde{n}_1$ and $\tilde{n}_2$ represent the complex refractive index of the two media. Reflectance and transmittance can then be expressed as:

$$R = \frac{I_R}{I_0} = |\hat{r}|^2 \tag{A.7a}$$

$$T = \frac{I_T}{I_0} = \sqrt{\varepsilon_1}|\hat{t}|^2 \tag{A.7b}$$

A material of thickness d, refractive index n and extinction coefficient κ can be conceived as a one-layer system. If this layer comes between two media (labeled by "1" and "3"), the total

reflection and transmission coefficients of the whole system are respectively:

$$\hat{r}_{123} = \frac{\hat{r}_{12} + \hat{r}_{23} e^{2i\delta}}{1 + \hat{r}_{12}\hat{r}_{23} e^{2i\delta}} \tag{A.8a}$$

$$\hat{t}_{123} = \frac{\hat{t}_{12}\hat{t}_{23} e^{i\delta}}{1 + \hat{r}_{12}\hat{r}_{23} e^{2i\delta}} \tag{A.8b}$$

where the reflection and transmission coefficients of each interface are calculated according to the Eq. A.6.
The complex angle δ is defined as

$$\delta = \beta + \frac{i\alpha d}{2}$$

Here β indicates a phase change and describes the ratio of material thickness and the wavelength in the medium while α is the absorption coefficient that describes the attenuation of wave. The general expression for reflectance and transmittance, considering the multiple reflections and transmissions in a film of thickness d, will be:

$$R_F = R\frac{(1 - e^{-\alpha d})^2 + 4e^{-\alpha d}\sin^2\beta}{(1 - Re^{-\alpha d})^2 + 4Re^{-\alpha d}\sin^2(\beta + \phi_r)} \tag{A.9a}$$

$$T_F = \frac{[(1 - R)^2 + 4R\sin^2\phi_T]e^{-\alpha d}}{(1 - Re^{-\alpha d})^2 + 4Re^{-\alpha d}\sin^2(\beta + \phi_t)} \tag{A.9b}$$

where R is the bulk reflectivity, ϕ_r and ϕ_t are the phase changes of the reflected and transmitted wave and α and β have been defined before.

By now, the close relation between the macroscopic response and the optical constants should be clear: the transmittance and reflectance, once known, can be used to retrieve the refractive index or dielectric function. In general, this procedure can be repeated for multilayer systems, but it results in complex expressions. Thus, excluding special cases in which the equations can be simplified in accordance with the properties of the experiment (e. g. thin film approximation [57]), the iterative calculation presented above is not the most convenient method to use. The matrix method, where matrices describe the transformation of two plane waves traveling in opposite directions between the layer and their development within them, appears more general and it is suitable for use in algorithm implementation. In this case reflection and transmission coefficients are represented as a product of matrices. The RefFIT software, which is used here for the data analysis, apply the Harbecke's approach [88, 67].

A.1.1 Kramers-Kronig relations

In order to solve the systems of equations introduced in the previous section and thus determine both components of complex optical functions, it is necessary to have both $R(\omega)$ and $T(\omega)$ available at the same time. This is not always possible, e.g. due to absorption phenomena. Kramers and Kronig (K-K) relations are involved in resolving this issue.
The K-K relations connect real and imaginary parts of any complex function that is analytic in the upper half-plane[40]. In a linear physical system the analytical nature of a response function is guaranteed by the principle of causality. Considering a complex function (i.e. $\hat{G} = G_1(\omega) + iG_2(\omega)$), the dispersion relations between its real and imaginary parts are given by:

$$G_1(\omega) = \frac{2}{\pi} \wp \int_0^\infty \frac{\omega' G_2(\omega')}{\omega'^2 - \omega^2} \, d\omega' \tag{A.10a}$$

$$G_2(\omega) = -\frac{2}{\pi\omega} \wp \int_0^\infty \frac{G_1(\omega')}{\omega'^2 - \omega^2} \, d\omega' \tag{A.10b}$$

where the symbol $\wp$ denotes the principal value integral. Through these general relations it is possible to derive the expressions connecting the real and imaginary parts of different optical parameters and response functions. For the complex refractive index which has been previously defined as $\tilde{n} = n + i\kappa$, the dispersion relations are as follows:

$$n(\omega) - 1 = \frac{2}{\pi} \wp \int_0^\infty \frac{\omega' \kappa(\omega')}{\omega'^2 - \omega^2} \, d\omega' \tag{A.11a}$$

$$\kappa(\omega) = -\frac{2}{\pi\omega} \wp \int_0^\infty \frac{\omega'^2 [n(\omega') - 1]}{\omega'^2 - \omega^2} \, d\omega' \tag{A.11b}$$

The complex dielectric constant links the polarization in response to an applied electric field to the displacement through the following equation:

$$4\pi \vec{P}(\omega) = [\tilde{\varepsilon}(\omega) - 1] \vec{E}(\omega) \tag{A.12}$$

consequently $\tilde{\varepsilon}(\omega) - 1$ is the appropriate response function [40]:

$$\varepsilon_1(\omega) - 1 = \frac{2}{\pi} \wp \int_0^\infty \frac{\omega'^2 \varepsilon_2(\omega')}{\omega'^2 - \omega^2}, d\omega' \tag{A.13a}$$

$$\varepsilon_2(\omega) = -\frac{2}{\pi\omega} \wp \int_0^\infty \frac{\omega'^2 [\varepsilon_1(\omega') - 1]}{\omega'^2 - \omega^2}, d\omega' \tag{A.13b}$$

Analog considerations can by made for the complex conductivity, the response function which describes the relation between the current and the electric field in the Ohm's law. Therefore, for $\tilde{\sigma}(\omega) = \sigma_1(\omega) + i\sigma(\omega)$, the dispersion relations which connect the real and imaginary parts of the complex conductivity are the given by:

$$\sigma_1(\omega) = \frac{2}{\pi} \wp \int_0^\infty \frac{\omega' \sigma_2(\omega')}{\omega'^2 - \omega^2}, d\omega' \tag{A.14a}$$

$$\sigma_2(\omega) = -\frac{2\omega}{\pi} \wp \int_0^\infty \frac{\sigma_1(\omega')}{\omega'^2 - \omega^2}, d\omega' \tag{A.14b}$$

The equations (A.11)-(A.13)-(A.14) were implicitly used during data analysis with the software RefFIT.

A.1.2 Drude-Lorentz model

The Drude-Lorentz approach consists in considering the linear response function of a material as a superposition of several contributions related to different charge excitations: the Drude contribution which represents the response of an electron gas to radiation and the contribution of several Lorentz oscillators (such as in insulators).

In spite of these are classical models, they produce a good description of absorption and dispersion of radiation in a solid [176].

As already seen in the chapter introducing plasmonics, the Drude model describes the diffusive properties of a metal, following a plasma model, where a gas of free electron of density n moves against a fixed background of positive ion cores, assuming an average time relaxation $\tau = 1/\Gamma_D$. The Lorentz model, indeed, is used to describe the insulators response where the valence electrons can be considered bonded to the nucleus. In this case the motion equation corresponds to:

$$m\frac{d^2\vec{r}}{dt^2} + m\gamma\frac{d\vec{r}}{dt} + m{\omega_0}^2\vec{r} = -e\vec{E} \tag{A.15}$$

where m is the electron mass. The Eq. A.15 defines the dynamics of a damped oscillating system in which the local electric field acting on the electron as a driving force. The second term on the left in the Eq. A.15 represents viscous damping and provides for an energy loss mechanism, while the term $[m{\omega_0}^2\vec{r}]$ is a Hooke's law restoring force. If the electric field has a time dependence expressed by $e^{-i\omega t}$, the solution to Eq. A.15 has the form:

$$\vec{r}(\omega) = \frac{-e\vec{E}/m}{({\omega_0}^2 - \omega^2) - i\gamma\omega} \tag{A.16}$$

The induced dipole moment for a sufficiently small displacement is defined as $\vec{p}(\omega) = -e\vec{r}(\omega)$ thus it can be written as:

$$\vec{p} = \frac{e^2\vec{E}}{m}\frac{1}{({\omega_0}^2 - \omega^2) - i\gamma\omega} = \tilde{\alpha}(\omega)\vec{E} \tag{A.17}$$

where $\tilde{\alpha}(\omega)$ is the atomic polarizability. The macroscopic polarizability is then the sum over all charge carriers per unit volume: $\vec{P} = N\tilde{\alpha}(\omega)\vec{E}$. At this point the displacement vector can be generalized as follows:

$$\vec{D}(\omega) = \tilde{\varepsilon}(\omega)\vec{E} = \vec{E} + 4\pi\vec{P}(\omega) \tag{A.18}$$

Now, using the last equation and the macroscopic polarizability expression, the dielectric complex function is $\tilde{\varepsilon}(\omega) = 1 + 4\pi N\tilde{\alpha}(\omega)$. Finally, making clear $\tilde{\alpha}(\omega)$, the complex dielectric function in terms of oscillator parameters becomes:

$$\tilde{\varepsilon}(\omega) = 1 + \frac{4\pi Ne^2}{m}\frac{1}{({\omega_0}^2 - \omega^2) - i\gamma\omega} = 1 + \frac{{S_{el}}^2}{({\omega_0}^2 - \omega^2) - i\omega\gamma} \tag{A.19}$$

S_{el} describes the oscillator strength and it is defined as:

$$S_{el} = \left(\frac{4\pi Ne^2}{m}\right)^{\frac{1}{2}} \tag{A.20}$$

Once $\tilde{\varepsilon}(\omega)$ is known, the relations defined above in the Eqs. A.4 and A.5 can be used to obtain the optical quantities of interest. The real part of optical conductivity for the Lorentz model thus will be:

$$\sigma_1(\omega) = \frac{S_{el}^2}{4\pi}\frac{\omega^2\gamma}{({\omega_0}^2 - \omega^2)^2 + (\omega\gamma)^2} \tag{A.21}$$

Here it is assumed that each atom contributes one electron to the absorption process. However the same atoms could contribute more than one electron and the dielectric functions becomes the sum of several terms each of which participates with its own ω_{0i}. As it was stated above, the Lorentz model is used to described the behavior of a bounded charge system subject to dissipation phenomena. In the view of a quantum-mechanical interpretation this model describes radiation absorption due to interband transition. Furthermore, the same model can be used to describe the contribution to the dielectric function due to the IR active optical phonons. In fact the transverse optical modes can produce a polarization and interact with electromagnetic radiation [186]. In terms of oscillator parameters, the ionic oscillator

strength is given by:

$$S_{ph} = \left[\frac{4\pi N(Ze)^2}{m^*}\right]^{\frac{1}{2}}$$

where m^* is the ion reduced mass, N is the density per unit volume and (Ze) is the ionic charge.

Setting by 0 the oscillator frequency ω_0 in the Eq. A.15, the Drude model for the treatment of the free charges effect to the optical properties of a solid is obtained. Now the equation of motion for a charge under the effect of an electric field is given by:

$$m\frac{d^2\vec{r}}{dt^2} + m\gamma_D\frac{d\vec{r}}{dt} = -e\vec{E} \tag{A.22}$$

In this model the wave function for a free electron is uniformly distributed thus the field acting on the electron is just the average field. The viscous damping term describes the ordinary scattering of electrons associated with electrical resistivity and the mean free time between collisions is defined as $\tau = {\gamma_D}^{-1}$ and it governs the relaxation of the system to equilibrium. The complex dielectric function for the Drude model is given by:

$$\tilde{\varepsilon}(\omega) = 1 - \frac{{\omega_p}^2}{(\omega^2 - i\omega\gamma_D)} \tag{A.23}$$

The quantity ω_P in Eq.A.23 is again the plasma frequency.

The contributions just introduced, which are due to free and bound carriers and due to the ions, can be summed resulting in an expression for the complex dielectric function:

$$\tilde{\varepsilon}(\omega) = \varepsilon_\infty - \frac{\omega_p^2}{\omega^2 - i\gamma_D\omega} + \sum_i \frac{S_{el,i}^2}{({\omega_{0i}}^2 - \omega^2) - i\gamma_i\omega} + \sum_j \frac{S_{ph,j}^2}{({\omega_{0j}}^2 - \omega^2) - i\gamma_j\omega} \tag{A.24}$$

The Eq. (A.24) contains the Drude term and an arbitrary number of Lorentz contributions. The effect of other contributions at higher frequencies is included in ε_∞, which is assumed to be real and frequency-independent in the range considered. This term comes from to the limit $\varepsilon_1(\omega \to \infty) \to 1$.

A.2 The RefFIT Software

In order to obtain the microscopic optical functions of Xenes, the reflectance and transmittance spectra were analyzed through RefFIT. The primary goal of this software is to get information about the complex dielectric function, considering that the linear macroscopic optical characteristics of materials are completely determined by $\tilde{\varepsilon}$. The spectral analysis is done using the method of the K-K constrained variational fitting, where the ability of the Kramers and Kronig analysis to extract the full spectral information is combined with the robustness of the dispersion analysis based on a least-square fitting [86].

The optical properties reported in this work were achieved through a special model for dielectric function capable to analyze the transmission and reflectance spectra coming from a multilayer system. As stated at the beginning, analytical expressions can be used to link the optical properties with transmittance and reflectance at normal incidence for a bilayer system. Each layer can be described by a Drude-Lorentz model where the parameters ω_0, ω_p and γ represent the quantities discussed above. The adjustable parameters that characterize the models of the dielectric function are varied in order to obtain the best match between the experimental and calculated data points. The curve fitting process, in this respect, is to all intent and purpose an optimization problem. A χ^2 functional can be defined as:

$$\chi^2(p_1, p_2, ...p_k) = \sum_i^N \left(\frac{y_i - f(x_i, p_1, ...p_M)}{\sigma_i} \right) \tag{A.25}$$

Here it is supposed to have a set of N experimental data point $\{x_i, y_i, \sigma_i\}$, where x_i is the frequency, y_i is the data value of reflectance or transmittance and σ_i is the data error bar. Finally $f(x_i, p_1, p_M)$ is the y_i^{model} value as function of frequency and a set of internal parameters. If it is assumed that all measured values y_i are normally distributed, than the best match would correspond to the minimal value of χ^2. The function $f(x_i, p_1, p_N)$ is in general a non-linear function of parameters so to perform the minimization of χ^2 functional the so-called Lavenberg-Marquardt algorithm is used. The Lavenberg-Marquardt algorithm is based on the self-adjustable balance between the two minimizing strategies: the gradient descendent and the inverse Hessian methods. The first method relies on a moving in the steepest descendent direction which is determined by the gradient defined as:

$$\beta_k = -\frac{1}{2}\frac{\partial \chi^2}{\partial p_k} = \sum_{i=1}^N \frac{y_i - f(x_i, p_1, ...p_M)}{\sigma_i^2} \frac{\partial f}{\partial p_k}(x_i, p_1, ...p_M) \tag{A.26}$$

To improve the fit, the parameters p_k are shifted by a quantity δp_k where δp_k corresponds to the product between a constant and β_k. The 'steepest descent' strategy becomes extremely

inefficient close to the minimum, especially in the multi-parameter space. For this reason, near the minimum, it is much better to assume that the function to be minimized has almost parabolic shape determined by the Hessian defined as follows:

$$\alpha_{kl} = \frac{1}{2}\frac{\partial^2\chi^2}{\partial p_k \partial p_l} = \sum_{i=1}^{N}\frac{1}{\sigma_i{}^2}\left\{\frac{\partial f(x_i, p_1, ...p_M)}{\partial p_k}\frac{\partial f(x_i, p_1, ...p_M)}{\partial p_l}\right\} \tag{A.27}$$

Here the second order derivative term is neglected because it is not important near the minimum and may even destabilize the fitting process. The displacement vector δp_k is determined from the linear system:

$$\sum_{i}^{M}\alpha_{kl}\delta p_l = \beta_k \tag{A.28}$$

It is important to focus on the parameters which are generally measured in different units. In order to obtain dimensionless quantities a normalization of the constant can be introduced:

$$\delta p_k = \frac{constant}{\alpha_{kk}}\beta_k \tag{A.29}$$

At this point, defining an α-matrix as $\alpha'_{kl} = \alpha_{kl}(1+\delta_{kl}\lambda)$ where λ is a dimensionless constant, it is possible to move from one method to another. The matrix α can be replaced with α' in the Equation [A.28]. In this way, for $\lambda << 1$ the inverse Hessian technique is taken into account while for $\lambda >> 1$ the off-diagonal elements can be almost neglected and the solution of the equation

$$\sum_{i}^{M}\alpha'_{kl}\delta p_l = \beta_k \tag{A.30}$$

becomes

$$\delta p_k = \frac{\beta_k}{\alpha'_{kk}} = \frac{\beta_k}{\alpha_{kk}(1+\lambda)} \tag{A.31}$$

The equation (A.31) has the same form as equation (A.29). It means that by increasing the parameter λ the "steepest descendent" limit is approached. The minimization process is iterative and stops when the stop criteria are satisfied.
The Lavenberg-Marquardt algorithm may easily handle models that contain a huge number of parameters because the number of iterations, needed to reach the minimum, it is not significantly influenced by them. It rather depends on the adequacy of the model to the experimental data and the success of the initial approximation [88].

It is important to emphasize that any realistic dielectric function complies the Kramers-Kronig relations. It implies that only one of the two function $\varepsilon_1(\omega)$ and $\varepsilon_2(\omega)$ is independent.

If the physical system is characterized by an optical response which is defined as sum of different terms due to the presence of independent subsystem, then the Kramers-Kronig relations must holds for each contribution separately. In addition $\tilde{\varepsilon}(\omega)$ ought to satisfy certain physical conditions. In particular $\varepsilon_1(\omega) = \varepsilon_1(-\omega)$ and $\varepsilon_2(\omega) = -\varepsilon_2(-\omega)$, hence it is sufficient to model $\tilde{\varepsilon}(\omega)$ for $\omega \geq 0$ only. Then, $\varepsilon_2(\omega > 0) \geq 0$, which means that the intensity of light cannot increase in the direction of propagation. The last requirement is that at very high frequencies the optical properties of matter are the same as those vacuum thus $\varepsilon_1(\omega \to \infty) = 1$ and $\varepsilon_2(\omega \to 0) = 0$.

In order to obtain a consistent model from which to get the optical conductivity, it was useful to apply a two-step scheme. This allowed to address the problem of extrapolation, typical also of the Kramers and Kronig analysis. First the experimental spectra is fitted by a series of Drude-Lorentz oscillators, with a limited number of parameters. The associate dielectric function model described, therefore, the major features of the experimental spectra and it was possible to assume that the frequency dependence outside the considered spectral range was right. In the second step the variational function is introduced. It consists in a large number of oscillators (of the order of experimental points) with the task of extracting the information model-independently. In this way the variational function can be seen as a small correction which is able to fit the fine spectra details. Applying this method the result is an analytical form for the optical functions of the analyzed samples.

Appendix B

Raman spectrum of graphene and silicene

B.1 Graphene

The structural and electronic properties of graphene are strongly reflected in its Raman response, in some ways more so than for other materials. Graphene's point group symmetry (D_{6h}) is the same of graphite [122] but it has two atoms per unit cell. The irreducible representation for the Brillouin zone centre Γ in given by: $A_{2u} + B_{2g} + E_{1u} + E_{2g}$ with one degenerate in-plane optical mode E_{2g} and one out-of-plane optical mode B_{2g} [51]. The E_{2g} phonons are Raman active whereas the B_{2g} phonon is neither Raman nor infrared active. In all carbon based structure such as graphene, graphite and nanotubes, Raman processes involving up to six phonons can be observed. Usually, however, the discussion is limited to one- and two-phonon processes. Raman bands are easily recognised in the single-layer-graphene spectrum (both supported and suspended). The G peak corresponds to the high-frequency E_{2g} phonon at Γ point. In monolayer defect-free graphene only the G peak fulfils the symmetry and wave vector conditions that a single-phonon mode must satisfy to be active. The D peak is due to the transversal optical phonons around the K point of the Brillouin zone and it is active by double resonance. Moreover, it is expected to be strongly dispersive with the excitation energy due to the screening of atomic vibrations carried out by the electronic states at the K point(Kohn anomaly) [141]. The same effect can also happen connecting two points belonging to the same cone around the K point. This gives the so-called D' peak. The 2D (2D') peak is the D (D')-peak overtone. 2D and 2D' peaks originate from a process where momentum conservation is satisfied by two phonons with opposite wavevectors. Thus they are always present, regardless of the presence of defects.

From the analysis of the intensity, frequency and line width of the characteristic G, D and 2D Raman modes, information about the quality, doping level and strain to which graphene is subject can be extracted. The line shape of the 2D peak is used to distinguish single-layer

graphene from multilayered structures [53], while the strength of the D mode is indicative of the degree of short range disorder in the sample. Both the frequency and the line width of the G mode together with the 2D peak position, can be used to monitor the doping level [33, 25]. Finally, it should be stressed that often the doping observed for supported graphene arises from the interaction of graphene with the substrate [14].

B.2 Silicene

This section briefly outlines the notable steps that led to the identification of the Raman spectrum of silicene and highlights its main features. The vibrational properties of free-standing silicene and silicene nano-roads were calculated by Scalise *et al* [148]. The Raman active modes of silicene were derived from the phonon dispersion curve and identified by analogy with those of graphene. Following their results, the Raman spectra of silicene are characterized by a main peak at about 575 cm^{-1} that corresponds to the degenerate in-plane E_{2g} zone-centre phonon, whereas the D mode, was found to be located at around 515 cm^{-1}. This optical mode, which is forbidden in the case of perfect sheets, is evident in the case of defects and disorder as for graphene [23]. Although the experimental realisation of silicene involves the introduction of a commensurate substrate, the agreement between the spectrum calculated for free-standing silicene and that measured for silicene on Ag(111) is remarkable. The Raman response reported by Cinquanta and co-workers [32] is dominated by a peak located at 516 cm^{-1} along with an asymmetric shoulder at lower frequencies (440-500 cm^{-1}). The first feature was related to the E_{2g} modes from different oriented domains. Conversely, the shoulder is motivated by the interaction of disorder-activated modes (A_{1g} and B_{2u}) and traces of unreconstructed sp^3 silicon. In particular, the Raman spectrum of silicene is found to reflect its hybridized nature, resulting from a buckling-induced distortion of the sp^2 hybridized structure. The Raman spectrum obtained in situ for silicene on Ag(111) and reported in Ref. [152] shows narrow Raman modes at 175 cm^{-1}, 216 cm^{-1} and 514 cm^{-1}, together with broad bands at 350 cm^{-1} and 480 cm^{1}, due to the co-existence of amorphous Si. In this case, the lowest frequency peaks were associated with active Raman A modes, which describe the out-of-plane displacement of Si atoms.

The Raman spectrum features of multilayer silicene have also been widely debated. The topic of discussion concerns the idea that multilayer silicene may be described as a trivial diamond-like phase [105, 17, 150] rather than a graphite-like phase. Work describing multilayer silicene as films, growing in successive flat terraces (in analogy to multilayer graphene), reports the main Raman peak to higher frequencies than that of bulk silicon [134, 60]. The blue-shift can be rationalized in terms of shorter Si-Si bond length with respect to

the one of bulk Si(111), being consistent with mixed sp^2-sp^3 bonds in multilayer silicene. Overall, Raman spectroscopy is a powerful technique that can be used to confirm both the 2D nature and the distorted honeycomb symmetry of epitaxial silicene.